Solar modulation studies and proton-electron separation with the AMS/RICH detector

Miguel Reis Orcinha

Thesis to obtain the Master of Science Degree in

Engineering Physics

Supervisors:	Prof. Dr. Fernando José de Carvalho Barão Dr. Maria Luísa Ferreira da Gama Velho Arruda

Examination Committee

President:	Prof. Dr. Mário João Martins Pimenta
Supervisor:	Prof. Dr. Fernando José de Carvalho Barão
Members of the Committee:	Prof. Dr. Bernardo António Neto Gomes Baptista Tomé Dr. Sylvie Rosier-Lees

November 2014

To Ana, Beatriz, Catarina and Francisco

Abstract

This work seeks to interpret Solar modulation under the terms of Plasma Physics, study its impact on the cosmic ray flux and characterize the AMS-02 Ring-Imaging Cherenkov Detector (RICH) detector. This is achieved by estimating the Solar magnetic field (from a Solar wind hypothesis) and deducing the corresponding particle transport equation. The transport equation in question includes diffusion, particle drifts and the three-dimensional Heliospheric Current Sheet (HCS). Several solutions to the transport equation are presented (Force-Field, 1D and 2D), the corresponding numerical models are then explained and their results shown. These showed a strong agreement with AMS-02 proton flux. After Solar modulation is interpreted and duly simulated, the AMS-02 RICH detector is studied in order to estimate its velocity resolution. Finally, from the results of RICH resolution study, a particle estimator, is created in order to help particle identification and data selection. The simulations revealed to be in good agreement with the estimated proton flux from AMS-02 data and exhibited the expected high energy behaviour. The model for the RICH velocity resolution described the expected shape. By making use of Monte Carlo data, the estimator proved to be a good tool to identify protons at low rigidities ($P < 15\mathrm{GV}$) but falls short at high rigidities in the discrimination aspect since the pdf functions between the different particles merge together for high velocity values. A cut was developed in order to keep the proton contamination lower than 1/100 for an electron selection. Using a new statistical variable, the model proved to have great discrimination power in the working regime.

Keywords

AMS-02, Solar Modulation, Force-Field solution, 1D solution, 2D solution, RICH resolution

Resumo

Este trabalho procura interpretar a modulação Solar dentro dos termos da Física de Plasmas, estudar o seu impacto no fluxo Galáctico de raios cósmicos e caracterizar o detector RICH de AMS-02. Este fá-lo através do cálculo do campo magnético Solar e da dedução da equação de transporte da densidade de raios cósmicos. A equação de transporte inclui difusão, deriva e a folha de corrente neutra heliosférica (HCS). Vários métodos foram usados para a resolução da equação de transporte (Force-Field, 1D e 2D), os correspondentes modelos numéricos foram deduzidos e os seus resultados discutidos. Os resultados das simulações revelaram um forte acordo com o fluxo de protões estimado a partir de dados de AMS-02 e exibe o esperado comportamento de altas energias. Em seguida, o detector RICH é estudado recorrendo ao fluxo de protões e estimar a sua resolução de medição. Finalmente, baseando-se nos resultados do estudo da resolução do RICH, um estimador de particulas, é criado para ajudar a separar partículas para ser usado em selecção de dados. O modelo do RICH estimou a resolução da velocidade com a forma esperada. Usando dados de Monte Carlo, o estimador provou ser uma ferramenta capaz de separar electrões de protões a baixa rigidez mas degenera para valores mais altos ($P > 15$ GV) dado que as diferentes funções de densidade de probabilidade fundem-se. Foi estimado também um corte em probabilidade que mantenha a contaminação de protões menor que 1/100 numa selecção de electrões. Usando ainda uma nova variável estatística, o modelo revelou ter grande poder de discriminação, dentro do regime de funcionamento.

Palavras Chave

AMS-02, Modulação Solar, modelo Force-Field, modelo 1D, modelo 2D, resolução do RICH

Contents

1 **Introduction** 1

- 1.1 Introduction . . . 2

2 **Cosmic Rays** 3

- 2.1 Introduction . . . 4
  - 2.1.1 Brief History of Cosmic Rays . . . 4
- 2.2 Cosmic Ray Spectrum . . . 6
  - 2.2.1 Energy distribution and Composition . . . 6
- 2.3 Cosmic ray Origin and Composition . . . 8

3 **Solar Modulation** 11

- 3.1 Introduction . . . 12
- 3.2 Solar Wind and the Heliosphere . . . 12
- 3.3 Solar Magnetic Field . . . 15
  - 3.3.1 Structure and Solar Activity . . . 16
- 3.4 Solar Modulation . . . 19
  - 3.4.1 Counting Particles . . . 20
  - 3.4.2 Cosmic Ray Transport Equation . . . 21
  - 3.4.3 Particle Diffusion and Drifts . . . 21
- 3.5 Solutions to the Transport Equation . . . 23
  - 3.5.1 The Local Interstellar Flux . . . 25
  - 3.5.2 Force-Field Solution . . . 26
  - 3.5.3 Finite Difference Method . . . 27
  - 3.5.4 1D Numerical Solution . . . 28
  - 3.5.5 2D Numerical Solution . . . 30
- 3.6 Results from numerical simulation . . . 32
  - 3.6.1 Force-Field and 1D numerical solutions . . . 32
  - 3.6.2 2D numerical solutions . . . 35

4 **The AMS-02 Experiment** 37

- 4.1 Introduction . . . 38
  - 4.1.1 Brief History . . . 38

4.1.2 Scientific Goals 38
4.2 Sub-detectors 38
4.2.1 Transition Radiation Detector 39
4.2.2 Time-Of-Flight Detector 40
4.2.3 Magnet 40
4.2.4 Silicon Tracker Detector 40
4.2.5 Ring-Imaging Cherenkov Detector 41
4.2.6 Electromagnetic Calorimeter 41
4.2.7 Anti-Coincidence Counter 41

5 RICH Resolution Study **43**
5.1 The RICH Detector in AMS-02 44
5.1.1 Cherenkov Radiation 44
5.1.2 RICH Velocity Measurement 46
5.1.3 Proton Data Analysis 47
5.2 RICH Resolution Model 50
5.2.1 Tracker Resolution Study 51
5.2.2 Primary Cosmic Ray Flux 55
5.2.2.A Local Interstellar Spectrum 55
5.2.2.B Solar Modulation 56
5.2.2.C Geomagnetic Cutoff 56
5.2.2.D Ring Probability 57
5.2.3 The Full Model 59
5.2.4 Results from Fit to Monte Carlo Data 60
5.2.5 Results from Fit to AMS-02 Data 62
5.3 Particle Estimator 64
5.3.1 Probability and Measurement 64
5.3.2 Monte Carlo Studies 67
5.3.3 Particle Separation and Contamination 71
5.3.4 Relative Probability 73

6 Conclusions and Prospects **77**
6.1 Conclusions and Prospects 78

Bibliography **81**

List of Figures

2.1 Scheme of Wulf's electroscope, drawn by wulf himself. 4

2.2 Hess balloon electroscope observations. 5

2.3 Schematic view of the beginning of an electromagnetic shower. 5

2.4 Fluxes of nuclei of the primary cosmic radiation. 7

2.5 The all-particle spectrum as a function of energy-per-nucleus from air shower measurements. 8

3.1 Comet trail and tail, evidence of the existence of a Solar wind. 12

3.2 Spherically symmetric hydrodynamic expansion velocity of an isothermal Solar corona, with $\mathrm{a} = 10^{11}\,\mathrm{cm}$. 13

3.3 Projection onto the Solar equatorial plane of the lines of the force of the magnetic field. 14

3.4 Schematic diagram of the current best understanding of the heliosphere's interstellar interaction. 15

3.5 Differential rotation of the Sun and magnetic instabilities. 15

3.6 Photo of the sun showing solar activity, sunspots and a solar flare. 16

3.7 Correlation between neutron monitor counts, Sunspot number and tilt angle. 17

3.8 Artistic depiction of the Heliospheric Current Sheet. 18

3.9 Diagram depicting the coordinates of the HCS in the Sun's coordinate system. The blue line represents the Solar system plane and the orange is the HCS plane at the Sun's surface. 18

3.10 Intensity of particles going through the ring. 20

3.11 Trajectories of positively charged particles in and near a neutral plane. 23

3.12 Local Interstellar primary cosmic ray flux for protons and helium nuclei. 26

3.13 Comparison of the computational molecules between forward Euler method and Crank-Nicolson. 28

3.14 Scheme showing the computational molecules of the ADI method. 30

3.15 Simulation of the Solar modulation of galactic cosmic protons, comparison of 1D solution with force-field solution, the thin dashed red line represents the Force-Field solution while the others are 1D solution at different radii, black line representing the $R = 1$ AU solution and orange representing $R = 90$ AU. 33

3.16 Simulation of the Solar modulation of galactic cosmic protons, comparison of 1D solution with force-field solution, scaled, the thin dashed red line represents the Force-Field solution while the others are 1D solution at different radii, black line representing the $R = 1$ AU solution and orange representing $R = 90$ AU. 33
3.17 Simulation of the Solar modulation of galactic cosmic α particles, comparison of 1D solution with force-field solution, the thin dashed red line represents the Force-Field solution while the others are 1D solution at different radii, black line representing the $R = 1$ AU solution and orange representing $R = 90$ AU. 34
3.18 Simulation of the Solar modulation of galactic cosmic α particles, comparison of 1D solution with force-field solution, scaled, the thin dashed red line represents the Force-Field solution while the others are 1D solution at different radii, black line representing the $R = 1$ AU solution and orange representing $R = 90$ AU. 34
3.19 Simulation of the Solar modulation of galactic cosmic protons, comparison of 1D solution with force-field solution, the thin red line represents the Force-Field solution while the others are 1D solution at different radii, black line representing the $R = 1$ AU solution and orange representing $R = 90$ AU. In yellow, the solution is detailed for R=89.0,...,89.9. 35
3.20 Simulation of the Solar modulation of galactic cosmic protons particles in the 2D solution at different radii. Black line represents flux at Earth, orange line the LIS flux and the red dots are AMS-02 2013 proton flux. 35

4.1 Photograph of the AMS-02 detector on the International Space Station. 38
4.2 Detailed schematic representation of the AMS-02 detector. 39
4.3 Depiction of one layer of the straw system used in the Transition Radiation Detector in AMS-02. 39
4.4 Schematic view of the Time-of-Flight detection system. 40
4.5 Photography of the Silicon Tracker being cabled on AMS-02 magnet [48]. 41
4.6 Photography of the Electromagnetic Calorimeter. 42

5.1 Diagram depicting Cherenkov radiation and the process by which it is created. 45
5.2 Cherenkov angle as a function of velocity and rigidity, in Aerogel (n=1.05), for protons. . 45
5.3 Cross-cut view of the RICH detector in AMS-02. 46
5.4 Diagram depicting the geometry of the RICH sub-detector in the AMS-02 overall scheme. 47
5.5 Reconstruction of simulated proton in Aerogel in RICH. 48
5.6 RICH velocity measurement for Aerogel, as a function of rigidity, for a real data proton sample. 49
5.7 RICH velocity measurement for Aerogel, as a function of rigidity, for a Monte-Carlo proton sample. 49
5.8 Velocity distribution width using a Gaussian fit function, applied to AMS-02 data. 50
5.9 Diagram depicting particle interaction with the Tracker detector and track extrapolation. . 51

5.10 Plot highlighting the smearing effect of rigidity measurement by showing the contribution of a 6 GV cosmic ray to the bin 7-8. 52
5.11 Plot showing the contribution of every rigidity to the bin 7-8 GV. 52
5.12 Inverse rigidity relative shift as a function of rigidity, for a MC proton sample. 53
5.13 Comparison between the sigma of one Gaussian model versus the sigma of the main Gaussian in the two Gaussian model, as fitting functions. 54
5.14 Inverse rigidity relative shift fit to slice 6.5-7 GV. 54
5.15 Relative weight between the two Normal distributions fitted to rigidity resolution. 55
5.16 σ_P/P for the second gaussian in the two gaussian model for the rigidity resolution, as a function of particle rigidity. 55
5.17 Local interstellar primary proton flux. 56
5.18 Solar modulation Force-Field factor by which the flux is multiplied. 56
5.19 Probability that a particle of rigidity P is able to reach ISS, through the Earth's magnetic field, averaged out over 3 months. 57
5.20 Mean number of radiated photoelectrons for Aerogel radiator for vertical protons, as a function of rigidity, in AMS-02. 58
5.21 Cherenkov ring probability for AGL, as a function of rigidity, in AMS-02, for protons. . . . 58
5.22 Probability density function of velocity, under the full model, for different rigidity bins. . . 59
5.23 Plot of the model fitted to Monte Carlo data, for several rigidity intervals. 60
5.24 Comparison of rigidity resolution between the full model fit, the single Gaussian fit to relative shift and the double Gaussian fit to relative shift in rigidity (displaying only main Gaussian in the double Gaussian case), applied to a Monte Carlo proton sample. 61
5.25 Aerogel velocity resolution, estimated for a Monte Carlo proton sample, using the full model as a fit function. 61
5.26 Plot of the model fitted to AMS-02 data, for several rigidity intervals. 62
5.27 Rigidity resolutions, from full model, for Monte Carlo and AMS-02 cosmic ray data. . . . 63
5.28 Velocity resolutions, from full model, for Monte Carlo and AMS-02 cosmic ray data. . . . 63
5.29 Scheme depicting the construction of the particles velocity probability density function. . 65
5.30 Diagram depicting the interaction between the RICH and Tracker. 65
5.31 Graph depicting the calculation of velocity probability. 66
5.32 Probability that a particle is a proton as given by the estimator, as a function of rigidity, ran over a Monte Carlo proton sample. 67
5.33 Probability that a particle is a proton as given by the estimator, normalized, as a function of rigidity, ran over a Monte Carlo proton sample. 68
5.34 Probability that a particle is a electron as given by the estimator, normalized, as a function of rigidity, ran over a Monte Carlo proton sample. 69
5.35 Profile of the probability distribution that a particle is a proton as given by the estimator, ran over a Monte Carlo proton sample. 70

5.36 Profile of the probability distribution that a particle is a electron as given by the estimator, ran over a Monte Carlo proton sample. 70
5.37 Probability that a particle is an electron as given by the estimator as a function probability of being an proton, ran over a Monte Carlo proton sample. 71
5.38 Contamination of protons as a function of Prob_e, for the rigidity bin 11-12 GV, estimated using a proton Monte Carlo sample. 72
5.39 Cut in Prob_e that insures a proton contamination lower than 1%, as a function of rigidity, estimated using a proton Monte Carlo sample. 72
5.40 Probability that a particle is a proton as given by the estimator divided by the probability of being a proton plus the probability of being an electron ($\frac{\mathrm{Prob}_p}{\mathrm{Prob}_p+\mathrm{Prob}_e}$), ran over a Monte Carlo proton sample. 73
5.41 Slices in rigidity of $\frac{\mathrm{Prob}_p}{\mathrm{Prob}_p+\mathrm{Prob}_e}$, 2 GV wide, ran over a Monte Carlo proton sample. . . . 74
5.42 Particle velocity as a function of rigidity for particles with $\frac{\mathrm{Prob}_p}{\mathrm{Prob}_p+\mathrm{Prob}_e}$ < 0.1. 75

List of Tables

2.1 Relative abundances F of cosmic-ray nuclei at 10.6 GeV/nucleon normalized to oxygen ($\equiv 1$) 7

Abbreviations

ACR Anomalous Cosmic Rays

ADI Alternating Direction Implicit

AMS Alpha Magnetic Spectrometer

CME Coronal Mass Ejection

ECAL Electromagnetic Calorimeter

GCR Galactic Cosmic Rays

HCS Heliospheric Current Sheet

ISS International Space Station

LIP Laboratório de Instrumentação e Física Experimental de Partículas

LIS Local Interstellar Spectrum

LISM Local Interstellar Medium

MHD Magnetohydrodynamics

NASA National Aeronautics and Space Administration

PDF probability density function

PDG Particle Data Group

PMT Photomultiplier Tube

QLT Quasi-Linear Theory

RICH Ring-Imaging Cherenkov Detector

SCR Solar Cosmic Rays

TAS Tracker Alignment System

TOF Time-of-Flight System

TRD Transition Radiation Detector

TRK Silicon Tracker

1

Introduction

Contents

1.1 Introduction 2

1.1 Introduction

The study of Astroparticle Physics and Cosmology is made by studying the bi-products of the reactions and phenomena of cosmological events. As these cosmic rays traverse the heliosphere to get to Earth's upper atmosphere, they change in energy, direction and may even be absorbed along the way. In order to get an accurate reading on the radiation that is emitted from the Galaxy and the rest of the universe, it is imperative that the propagation mechanisms that lead the cosmic rays to the Solar system is understood.

This thesis seeks to study and simulate the mechanism that governs Solar modulation of galactic cosmic rays and develop a proton/electron (or positron) separation tool that would allow to select particles using the AMS RICH detector.

Solar modulation is the process by which the plasma emitted by the Sun interferes with the entry of Galactic cosmic rays into the Solar system, thereby altering the intensity and energy of the cosmic ray flux detected at Earth.

The study of Solar modulation began with the classical paper made by Parker [51]. In his paper he described how it was possible to have a radial wind of hot gas streaming outwards from the Sun. This interpretation of the Solar wind and the derivation of the magnetic field trapped in it marked the beginning of Solar modulation study.

This work begins with a small introduction to cosmic ray physics, after which a theoretical approach is taken in order to understand the Solar plasma. Still in line with plasma physics, and aided by a Solar magnetic field model, the Parker transport equation is deduced and the Parker model of the Solar plasma is presented in order to establish the framework in which it will be solved.

Several approaches were taken when trying to solve the cosmic ray transport equation. Some of these approaches required aid from numerical methods and the methodology behind developing them was then presented. After establishing the simulation premisses, the results were shown and discussed. In the current literature, only the simulation results are presented and most of the derivations are usually skipped. In this work, all the derivations and simulation details (including models and numerical schemes) are shown and explained in detail.

As a next step, the AMS-02 experiment was presented and the second part of the work began.

On the line of estimating a flux based on data, a C++ framework was developed around the AMS-02 Ring-Imaging Cherenkov Detector (RICH) and Silicon Tracker (TRK). From AMS-02 data and official AMS-02 Monte Carlo simulations of the detectors, the behaviour of the RICH and TRK measurement resolutions were studied in order to develop a statistical model that correctly estimates RICH velocity resolution.

The results were shown and used towards the final part of the thesis, the development of an estimator based on the independent measurements of both RICH and TRK in order to identify particles species, based around a mass hypothesis, for low rigidity events ($P < 15$ GV).

2

Cosmic Rays

Contents

2.1 Introduction 4
2.2 Cosmic Ray Spectrum 6
2.3 Cosmic ray Origin and Composition 8

2.1 Introduction

The Particle Data Group (PDG) offers a definition of cosmic ray as all the cosmic radiation incident at the top of the terrestrial atmosphere, which includes all stable charged particles and nuclei with lifetimes of order 10^6 years or longer[38].

Beginning with a brief historic introduction, this chapter will give an overview of the cosmic ray spectrum, chemical composition and mechanisms responsible for its origin.

2.1.1 Brief History of Cosmic Rays

With the discovery of X-rays in 1895, Röntgen opened the way to the study of radioactivity moving towards the twentieth century.

In 1909, the dominant theory towards ambient radiation was that ionizing radiation would come from the rocks and soil. To test this theory, Theodor Wulf [70] measured the rate of ionization at the bottom and at the top of the Eiffel tower (300 m), using a series of electroscopes of his own design (shown in figure 2.1). He expected an exponential decrease in the rate of ionization measured as he got farther from the ground but this decrease was only of about half of that measured at the surface, contradicting his expectations.

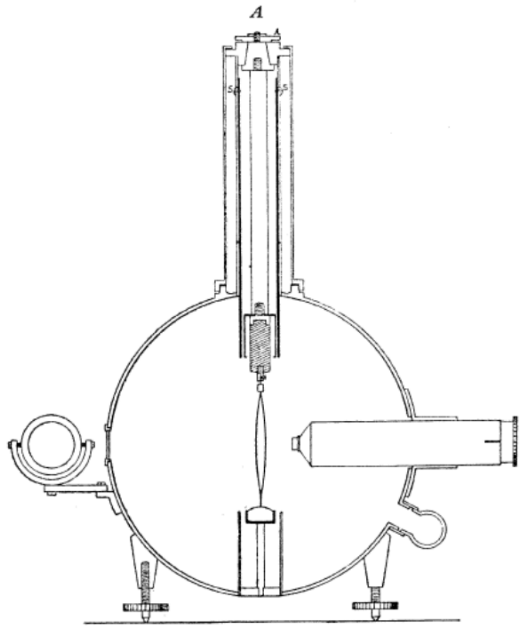

Figure 2.1: Scheme of Wulf's electroscope, drawn by wulf himself.

Victor Francis Hess took the next big step by taking electroscopes in balloon flights. Even though he was not the first to do so [27], he was the first one with the interpretation that lead to the discovering of cosmic rays.

Hess, in 1912, showed, from his balloon flights, that as the altitude increased, the radiation decreased until it reached a minimum, starting to increase again rapidly above 1400 m, as can be seen in figure 2.2. This was a major breakthrough since it proved that the ionizing radiation origin could not be terrestrial, it had to come from above. He also found that the radiation had hourly variations but he did not find a reduction of the radiation's intensity during the night or during a Solar eclipse, thus concluding that the origin of the radiation could not be the Sun, it had to be from outside the Solar System.

This discovery of the natural source of high-energy particles coming from outside the Solar System won him the Nobel Prize in Physics in 1936.

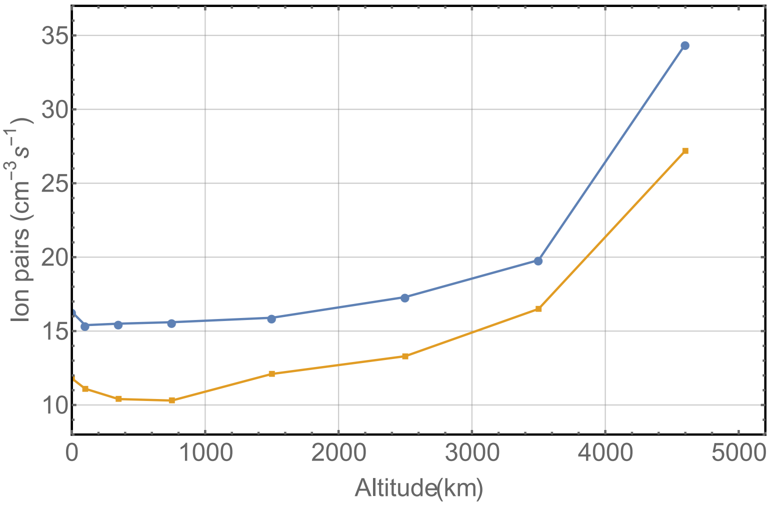

Figure 2.2: Hess balloon electroscope observations [30].

Hess' discoveries were corroborated by later balloon experiments such as those made by Kolhörster [41].

The term **cosmic ray** was coined by Robert Millikan in the 1920's.

In 1927, J. Clay discovered the geomagnetic effect by measuring a variation of cosmic ray intensity with latitude [16].

In 1930, Bruno Rossi predicted a difference between the intensity of cosmic rays arriving from the east and the west, depending on the charge of the primary particles, the **East-West Effect** [58]. His prediction was later proven right by several experiments [3, 33, 59].

After deriving the differential cross-section of the scattering of positrons by electrons (the **Bhabha scattering**),Homi Bhabha, together with Walter Heitler, published in 1937 an article describing how cosmic rays interact with the upper atmosphere to produce particles observed at ground level [7]. They explained cosmic ray shower formation as a cascade production of γ-rays and positron-electron pairs. This discovery was fundamental towards the study of high energy cosmic rays since by studying these air shower, it is possible to use the atmosphere as part of a large detector system (detection principle used in Pierre-Auger Observatory and other experiments).

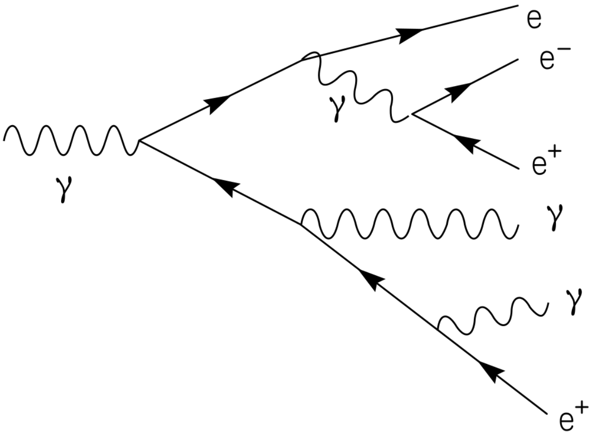

Figure 2.3: Schematic view of the beginning of an electromagnetic shower.

Further study of cosmic rays lead to the discovery of several new particles among which were [6]:

- 1937 - Muon discovery by Neddermeyer (mistaken for a pion until proven wrong in 1947 by Conversi, Pancini and Piccioni)
- 1947 - Pion discovery by Lattes, Occhialini and Powell
- 1947 - Kaon discovered by Rochester and Butler
- 1951 - Λ discovered by Armenteros

In 1949, Enrico Fermi proposed a model explaining how cosmic particles could be accelerated up to relativistic speeds, allowing them to reach Earth [23]. This phenomenon is now known as Fermi acceleration.

As time went by, the study of cosmic rays developed from ground-based study to balloon experiments and, lastly, to upper atmosphere and spacial detectors.

The discovery of this cosmic radiation together with an appropriate interpretation, allows for a deeper understanding of the Universe and the physical phenomena that lead to its current state.

2.2 Cosmic Ray Spectrum

The main difference between a **primary** and a **secundary** cosmic ray is that the first is accelerated by astrophysical sources and the latter is produced by interactions of the primaries with the interstellar gas.

These primaries are bi-products of stellar nucleosynthesis. The study of cosmic rays such as antiprotons and positrons is still up for debate and constitutes one of the objectives of AMS-02 experiment, which will be described further on.

2.2.1 Energy distribution and Composition

Most particles that reach Earth's upper atmosphere come (apart from Solar flares) from outside the Solar System and are **modulated** by the expanding magnetized plasma generated by the Sun. This plasma decelerates and partially excludes the lower energy Galactic cosmic rays [38]. Solar activity is also known to be anti-correlated with the intensity of cosmic rays at low energies as well, the **Forbush decrease** phenomenon.

After passing through the Solar plasma, these Galactic cosmic rays have to overcome another barrier, the geomagnetic field. This magnetic field will cut out any low energy radiation. These two phenomena combined give any cosmic ray on the GeV energy range a dependency on both time and space.

The intensity of primary nucleons in energy range from the GeV to 100 TeV is approximately given by the following power law,

$$I_N(E) \approx 1.8 \times 10^4 \left(\frac{E}{1\,\mathrm{GeV}}\right)^{-\alpha} \left[\frac{\mathrm{nucleons}}{m^2\,s\,sr\,\mathrm{GeV}}\right], \tag{2.1}$$

where α is the differential spectral index of the cosmic ray flux and varies with the energy region in the following way,

$$\begin{cases} \alpha \approx 2.7, & \text{if } E < 10^{15}\text{eV} \\ \alpha \approx 3.0, & \text{if } 10^{15} < E < 10^{18}\text{eV} \\ \alpha \approx 2.8, & \text{if } E < 10^{15}\text{eV} \end{cases} \tag{2.2}$$

The complete spectrum for different particles, as measured by several experiments [1, 5, 19, 22, 28, 29, 39, 44, 45, 60, 63, 67], is shown in figure 2.4.

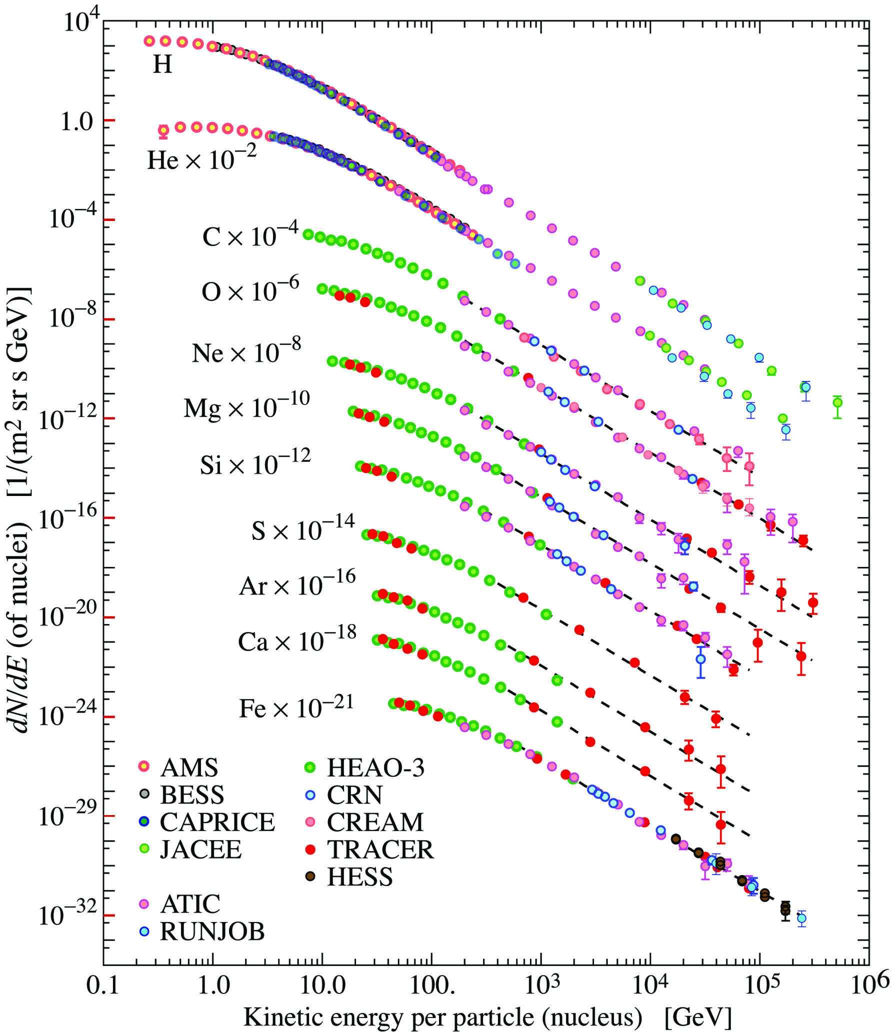

Figure 2.4: Fluxes of nuclei of the primary cosmic radiation [38].

The composition and energy spectrum of nuclei are interpreted using propagation models in which the sources are located within the Galaxy and these travel towards the Solar System by traversing through the Galactic magnetic field. This gives rise to a complex spectrum (detailed in figure 2.4) that shows the average chemical composition, given by table 2.1.

Z	Element	F
1	H	540
2	He	26
3-5	Li-B	0.4
6-8	C-O	2.20
9-10	F-Ne	0.30
11-12	Na-Mg	0.22

Z	Element	F
13-14	Al-Si	0.19
15-16	P-S	0.03
17-18	Cl-Ar	0.01
19-20	K-Ca	0.02
21-25	Sc-Mn	0.05
26-28	Fe-Ni	0.12

Table 2.1: Relative abundances F of cosmic-ray nuclei at 10.6 GeV/nucleon normalized to oxygen ($\equiv 1$) [38]

Cosmic rays display a nearly isotropical structure at most energies but some experiments (such as Milagro and IceCube), showed some anisotropy at very high energies (TeV-PeV scales), that might be correlated to nearby sources.

The spectrum from figure 2.4 extends into higher energies (up to 10^{20} GeV) if the study of cosmic ray showers is taken into account as well (it is very difficult to directly measure particles with such high energies). In this case, the atmosphere is used as part of the detector. A very high energy cosmic ray will interact with the atmosphere and generate a shower of particles that will then be detected in the ground. By studying shower development in air, it's possible to estimate the energy and direction of the primary particle that generated the shower.

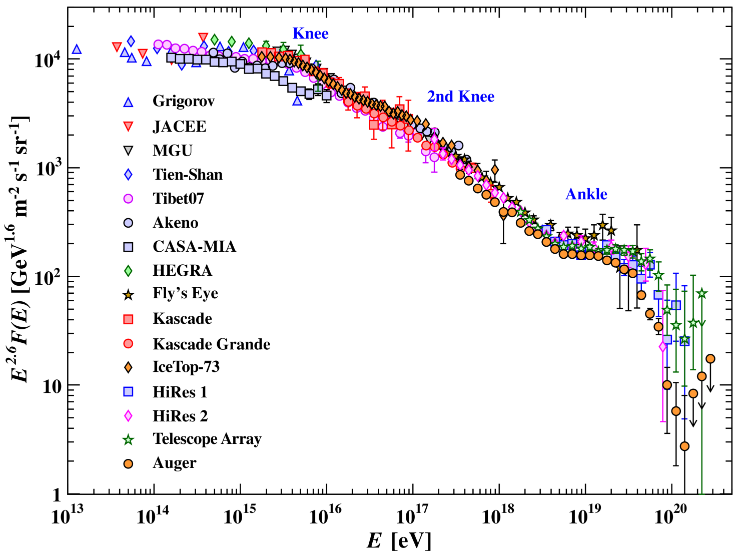

Figure 2.5: The all-particle spectrum as a function of energy-per-nucleus from air shower measurements[38].

Figure 2.5 shows the extended cosmic ray spectrum up to 10^{20} eV.

Observing this more complete spectrum reveals another structure, instead of having just one power law it is possible to identify two more powers law (with different indexes, as shown in expression 2.2), each being separated by a **knee**, and having a so-called **ankle** in the end of the entire spectrum.

2.3 Cosmic ray Origin and Composition

Cosmic rays are divided into three categories, depending on their origin: Galactic Cosmic Rays (GCR), Solar Cosmic Rays (SCR) and Anomalous Cosmic Rays (ACR).

GCR are the most typical cosmic rays, being comprised of $\sim 90\%$ protons, 9% alpha particles and 1% electrons, these extend to energies up to 10^{20} eV. They are accelerated by supernovae remnants[43] in a process called **Fermi Acceleration**. A star, upon turning supernova, will leave behind remnants, capable of lasting up to thousands of years. According to the supernovae remnants cosmic ray hypothesis, particles are accelerated by the shock front of the supernova and then further accelerated by the magnetic fields.

SCR, as their name tells, are particles originating from the Sun. They mostly consist of protons, electrons and helium ions with energy ranging from a few keV up to GeV. They can originate from energization at a Solar flare site or by shock waves associated with coronal mass ejections.

ACR arise mainly from neutral interstellar atoms which are swept into the heliosphere by the motion of the Sun through the interstellar medium[65]. These items then become singly ionized either by photoionization by Solar UV photons or by charge exchange collisions with Solar wind protons.

3

Solar Modulation

Contents

3.1 Introduction 12
3.2 Solar Wind and the Heliosphere 12
3.3 Solar Magnetic Field 15
3.4 Solar Modulation 19
3.5 Solutions to the Transport Equation 23
3.6 Results from numerical simulation 32

3.1 Introduction

The temporal variation of the cosmic-ray intensity in the heliosphere is called Solar Modulation of Galactic cosmic rays [47].

This definition is based on the observation of periodical changes to the cosmic-ray flux measured in Earth, correlated with Solar activity. There are several periods for these variations and the most notorious are the 11-year cycle, due to change in Solar activity, and the 27-day cycle, due to the Sun's rotation. The reasons why there would be these two periodicities will become clearer in the sections ahead.

3.2 Solar Wind and the Heliosphere

In 1951, by observing the tails of comets (as seen in figure 3.1), Biermann [8, 9] suggested that their odd shape was not due to the pressure of the Solar radiation on the molecules in the comet's tail but rather by a gas streaming outwardly from the Sun. His suggestion was that this gas was flowing radially in all directions from the Sun and had to have velocities ranging from 500 to 1500 km/s.

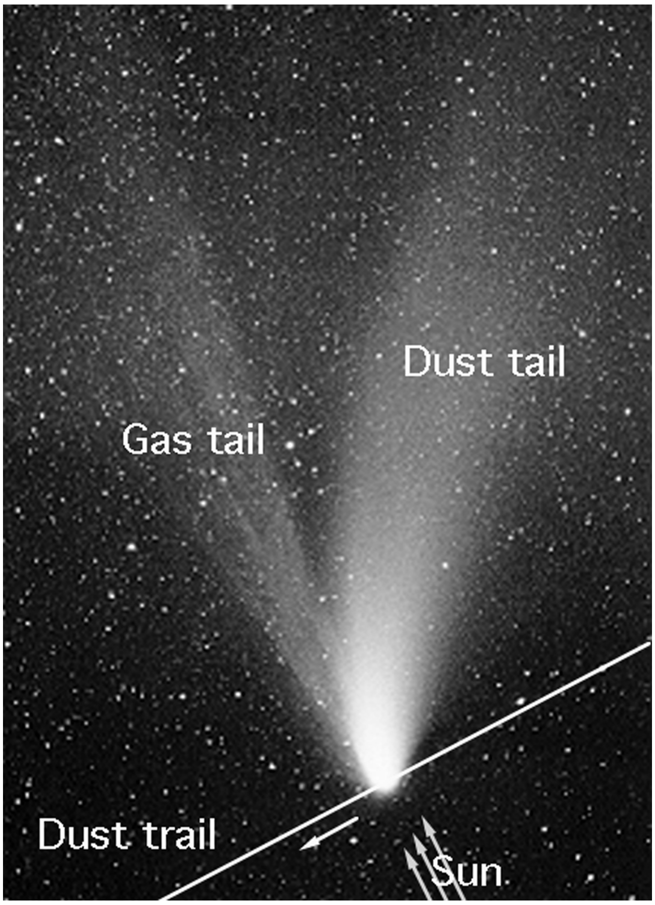

Figure 3.1: Comet trail and tail, evidence of the existence of a Solar wind [49].

This phenomenon is known as Solar wind and its characteristics are essential in understanding Solar Modulation. It permeates the entire Solar system creating the Heliosphere.

In 1958, Parker tried to understand the consequences of having this outward stream of hot gas coming from the Sun. In his famous article [51], he showed that there should be no hydrostatic equilibrium solution for the Solar wind and thus tried to estimate what sort of steady expansion could be expected from the Solar corona.

He started by assuming that the temperature distribution was modelled by a function of only distance, $T(r)$, and then tried to see the consequences of this expanding corona by having the following equation of motion (both assuming a spherical corona and that it is a hot enough so that the gas is fully ionized, thus ensuing a gas pressure given by $2NkT$),

$$NMv\frac{\mathrm{d}v}{\mathrm{d}r} = -\frac{\mathrm{d}}{\mathrm{d}r}(2NkT) - GNMM_{\odot} \tag{3.1}$$

and the following equation of continuity,

$$\frac{\mathrm{d}}{\mathrm{d}r}(r^2Nv) = 0. \tag{3.2}$$

He then derived the expansion velocity of a spherically symmetric and isothermal Solar corona, as can be seen in figure 3.2.

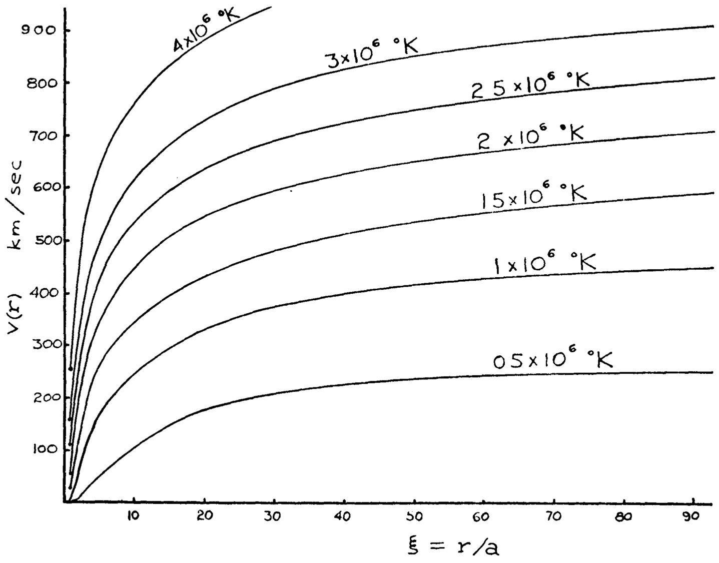

Figure 3.2: Spherically symmetric hydrodynamic expansion velocity of an isothermal Solar corona, with $\mathrm{a} = 10^{11}\,\mathrm{cm}$.

He then hypothesised that if there were no field-free regions in the Sun from which the gas could be emitted, the stream of outward flowing fully-ionized gas, and according to the Alfvén's *frozen-flux* theorem, should carry the magnetic field force lines. This area of study is known as Magnetohydrodynamics (MHD).

If there is a region defined by $r = b$, around the Sun, after which the ejected gas has a completely spherical symmetry, the magnetic field lines should have the same structure.

Assuming a $1/r^2$ radial Solar magnetic field (due to spherically expanding density of field lines) and a constant outward velocity V_w for the Solar wind, the Solar wind velocity should be (as seen from a reference frame co-rotating with the Sun at a frequency of ω),

$$v_r = V_w, \;\; v_\theta = 0, \;\; v_\phi = \omega(r-b)\sin\theta, \tag{3.3}$$

thus having the streamline given by

$$\frac{r}{b} - 1 - \ln\left(\frac{r}{b}\right) = \frac{V_w}{b\omega}(\phi - \phi_0), \tag{3.4}$$

which in turn leads to the, later known as, Parker Solar Magnetic Field (shown in figure 3.3),

$$\begin{aligned}
&B_r(r,\theta,\phi) = B(\theta,\phi_0)\left(\frac{b}{r}\right)^2 \\
&B_\theta(r,\theta,\phi) = 0 \\
&B_\phi(r,\theta,\phi) = B(\theta,\phi_0)\left(\frac{\omega}{V_w}\right)(r-b)\left(\frac{b}{r}\right)^2 \sin\theta.
\end{aligned} \tag{3.5}$$

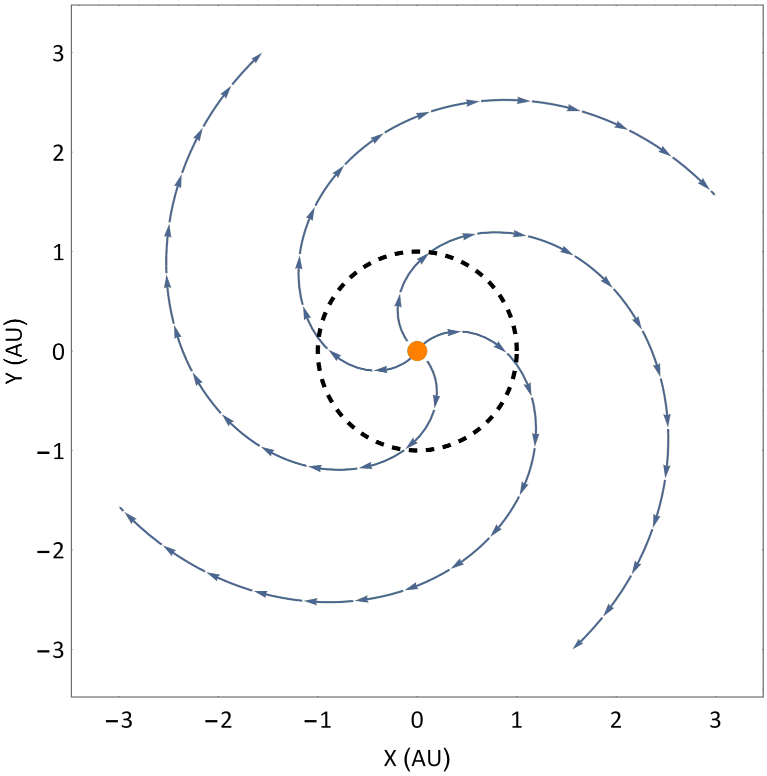

Figure 3.3: Projection onto the Solar equatorial plane of the lines of the force of the magnetic field. Dashed line is $r = 1\,\mathrm{AU}$, Earth's orbit around the Sun.

We now begin to see the crucial role of the Solar wind as the agent behind both the existence of the heliosphere and the shape of the magnetic field inside of it since it will transport the magnetic field lines all across the Solar System.

Even though the idea of a constant speed Solar wind is only an approximation, the first measurements of the mean interplanetary magnetic field at Earth's orbit, made by Ness et al. [50] showed rapid fluctuations ($\Delta B \sim B$). Despite that, they were able to estimate a mean field of $B \sim 0.6 \times 10^{-4}\,\mathrm{Gauss}$ inclined to the expected spiral angle ($\psi = \arctan(r\omega/V_w)$) of $30 - 45°$ [52].

After Parker's original work, there have been numerous theoretical enhancements. In the current understanding of the heliosphere, the plasma keeps expanding until its outward pressure equalizes with the Local Interstellar Medium (LISM)'s pressure and it becomes a boundary called the **heliopause**. Before this boundary, another boundary can be defined, the **Termination Shock**. It is the point after which the Solar wind slows down and becomes subsonic [18]. Spacecrafts were sent across the Solar system to evaluate the behaviour of the heliosphere and the Solar wind. Voyager 1, in 2004, and Voyager 2, in 2007, traversed the Termination Shock.

It is important to note how the influence of the LISM flow in the shape of the heliopause, as is shown figure 3.4.

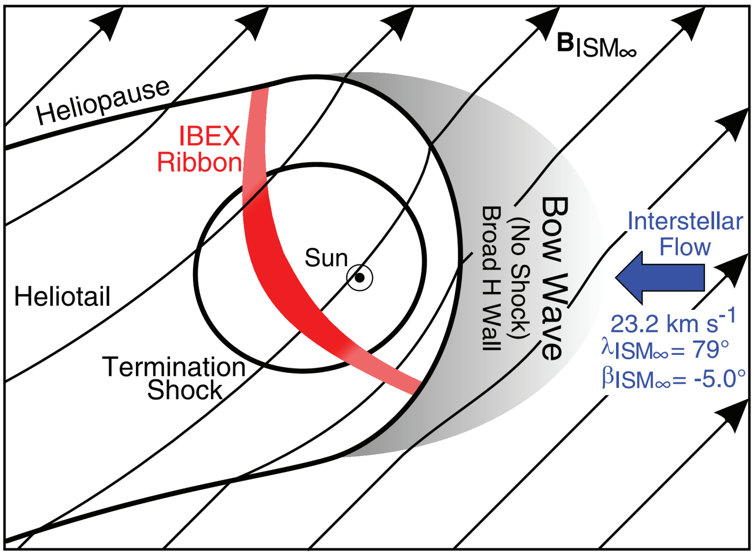
Heliopause
IBEX
Ribbon
Heliotail
Sun
Termination
Shock
$B_{ISM\infty}$
Bow Wave
(No Shock)
Broad H Wall
Interstellar
Flow
23.2 km s^{-1}
$\lambda_{ISM\infty}$= 79°
$\beta_{ISM\infty}$= -5.0°

Figure 3.4: Schematic diagram of the current best understanding of the heliosphere's interstellar interaction [18].

Even though the heliosphere has a very complex shape on its furthest regions, close to Earth $(r = 1\,\mathrm{AU})$, the radial Solar wind (even if it has variable speed) is usually a good start when it comes to the analysis of the magnetic field.

3.3 Solar Magnetic Field

The Sun's plasma displays a highly complex structure of motion. The interaction between the plasma and a magnetic field can be modelled using the principles of MHD in which plasma is treated as a continuous medium.

The Sun also exhibits a differential rotation , spinning faster in the equator than it does in the poles, as depicted in figure 3.5.

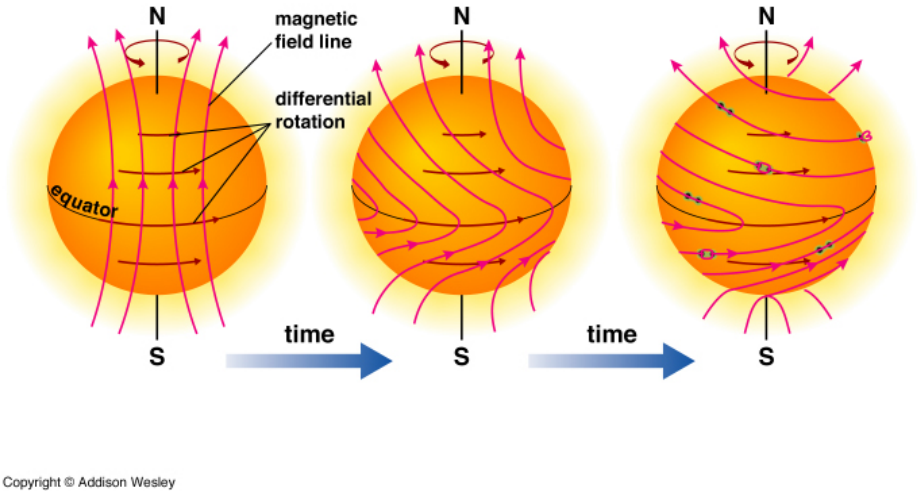
N
magnetic
field line
differential
rotation
equator
S
time
N
S
time
N
S
Copyright © Addison Wesley

Figure 3.5: Differential rotation of the Sun and magnetic instabilities.

The complex flow of the Sun's plasma gives rise to several physical phenomena such as the global magnetic field (dipole), Sunspots and prominences.

3.3.1 Structure and Solar Activity

The main Solar magnetic field component is the dipole created from a major MHD dynamo.

This magnetic dipole inverts its polarity with a periodicity of 11 years, changing the entire spacial environment inside the Solar system. It is known as the **Solar Activity Cycle**. A direct correlation between this cycle, the angle of the Solar magnetic dipole with the rotation axis (known as tilt angle and henceforth shown as α) and the number of observed sunspots was found (as can be seen in figure 3.7). Figure 3.6 shows these sunspots in dark. As the Sun gets closer to flipping its magnetic dipole, the more twisted the magnetic field lines become, creating more areas of instability and Solar sunspots start to emerge in its surface.

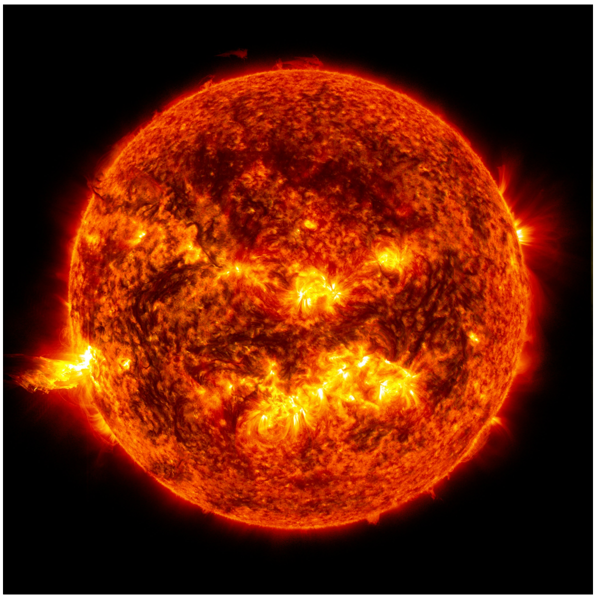

Figure 3.6: Photo of the sun showing solar activity, sunspots and a solar flare[49].

The existence of Sunspots has been known since at least the fourth century B.C. These can be as large as 20000 km and have temperatures of 3000-4500 K, constrasting with the surrounding 5780 K. They are caused by intense magnetic activity which inhibits convection, thus allowing it to cool down [40]. These Sunspots usually appear in pairs of opposing polarities but can also take place under other configurations.

With the increase in Solar activity and magnetic field instability, prominences and their rupture become more frequent. These ruptures originate Coronal Mass Ejection (CME) which in turn will give rise to a decrease in the observed galactic cosmic ray, a **Forbush decrease**. This jet of plasma will change the shape of the magnetic field abruptly and increase the **geomagnetic cutoff** energy (energy required for a charged particle to not be trapped in the geomagnetic field, if the particle has lower energy than the cutoff, it begins gyrating with a very small radius and becomes trapped, never reaching the Earth). This effect is only felt on Earth a few days after the Solar event.

During the Solar Activity Cycle the direction of the dipole changes and the angle it makes with the rotation axis goes from its minimum at $\sim 10^{\circ}$ to its maximum at $\sim 70^{\circ}$, by which time the magnetic field starts degrading and after a time it will start going from the maximum to the minimum but this time with an inverted polarity.

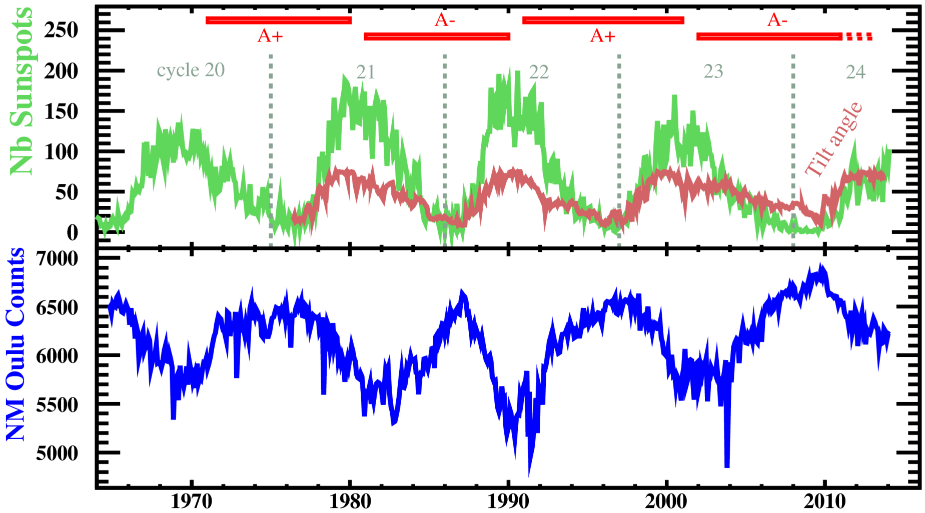

Figure 3.7: Correlation between neutron monitor counts, Sunspot number and tilt angle.

These events all have major significance to the modelling of the Sun's magnetic field. The Sunspots and CME's can create fluctuations in the magnetic field but these are not periodical.

Apart from the 11-year cycle and its effect on the change in the flux, the 26-day rotation of the Sun is also responsible for variations in the magnetic field as a consequence of the tilt angle (α).

The fact that the Sun's magnetic field is mainly a dipole implies the existence of a plane that separates the two major magnetic domains, perpendicular to the dipole direction. This plane is called the Heliospheric Current Sheet (HCS).

By assuming that the magnetic field is reasonably stable across several Solar rotation periods it is possible to describe the topology of this magnetic field. The wind will flow continuously and propagate the magnetic field lines according to the Solar dipole configuration by the time of leaving the corona. The field lines will flow outward continuously and create a peculiar shape, Parker described this phenomenon as a ballerina skirt.

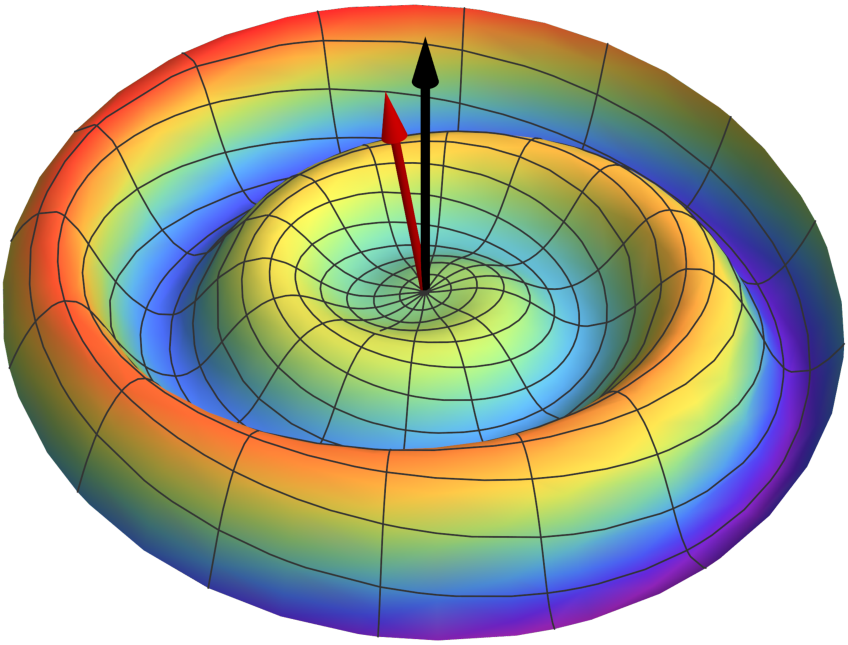

Figure 3.8: Artistic depiction of the Heliospheric Current Sheet. Black arrow indicates the axis of Solar rotation and the red arrow indicates the magnetic dipole direction.

Any point in the Sun's surface is transported through the heliosphere by the Solar wind according to the following equations written in the Sun's coordinate system (one where the rotation axis is aligned with the Z direction),

$$\begin{aligned} r(t) &= V_w t + r_0, \\ \theta(t) &= \theta(t=0), \\ \phi(t) &= -\omega t + \phi_0, \end{aligned} \tag{3.6}$$

where V_w is the Solar wind speed and ω is the Sun's angular frequency for rotation.

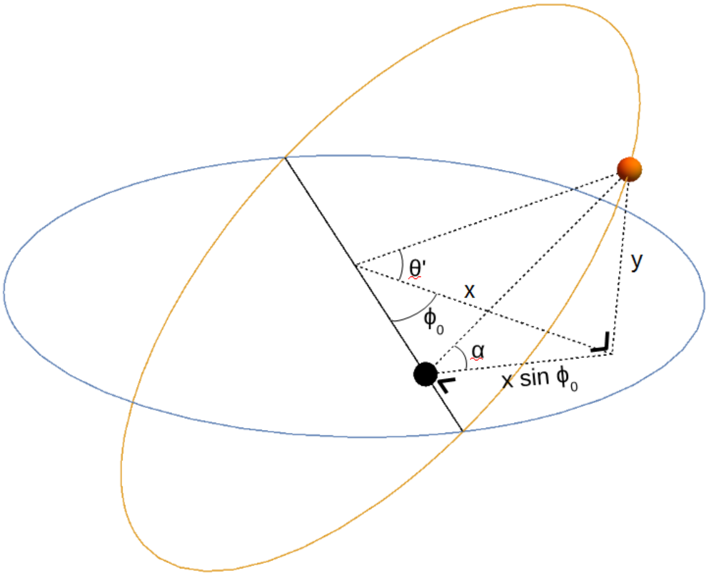

Figure 3.9: Diagram depicting the coordinates of the HCS in the Sun's coordinate system. The blue line represents the Solar system plane and the orange is the HCS plane at the Sun's surface.

In the case of a null tilt angle ($\alpha = 0$), all the points in the HCS are at the same $\theta = \theta_{\mathrm{HCS}} = \pi/2$.

The fact that there is a non-zero tilt angle demands that $\theta_0 = \theta_{\text{HCS}} = f(\phi_0)$. In all calculations that follow, the usage of θ' refers to the angle shown in figure 3.9, which relates to the angle of the point in spherical coordinates as $\theta' = \frac{\pi}{2} - \theta_{\text{HCS}}$.

Refering to figure 3.9, we can start by calculating the spherical coordinates of a point that lies in the HCS plane with respect to the Sun's coordinate system,

$$\begin{aligned} \tan\theta' &= \frac{y}{x} \\ \frac{y}{x\sin\phi_0} &= \tan\alpha \end{aligned} \tag{3.7}$$

which in turn leads to,

$$\tan\theta' = \tan\alpha\sin\phi_0 \Rightarrow \tan\left(\frac{\pi}{2} - \theta_{\text{HCS}}\right) = \tan\alpha\sin\phi_0 \tag{3.8}$$

The only substitution left is to parametrize ϕ_0 as a function of r and ϕ, so we can propagate it across space. This is done by making use of expression 3.6,

$$\phi_0 = \phi - \frac{\omega(r-b)}{v_w}, \tag{3.9}$$

which when inserted into 3.8 gives us $\theta_{\text{HCS}}(r, \phi)$,

$$\theta_{\text{HCS}} = \frac{\pi}{2} - \arctan\left[\tan\alpha\sin\left(\phi - \frac{\omega(r-b)}{v_w}\right)\right] \tag{3.10}$$

Now that we know how the HCS behaves we can derive the full Parker magnetic field from those shown in equation 3.5, by including the wavy neutral current sheet,

$$\vec{B}(r,\theta,\phi) = \frac{\pm B_0 r_0^2}{r^2}\left(\vec{e}_r - \frac{(r-b)\omega}{v_w}\sin\theta\,\vec{e}_\phi\right)[1 - 2H(\theta - \theta_{\text{HCS}})], \tag{3.11}$$

where $B_0 r_0^2$ is a constant which comes from the definition of the magnetic field and H is the Heaviside step function. The ± sign is there to characterize the Solar cycle modelled as being a positive, with fields lines coming out from the northern hemisphere or negative.

Now we understand what is the heliosphere and how it propagates the magnetic field. The next step is understanding how charged particles interact with this magnetic field.

3.4 Solar Modulation

When charged particles pass through a magnetic field they interact with the field lines, shifting their trajectories and changing their energies. The motion of the particle in the magnetic field is characterized by the circular motion around a point (**guiding centre**) and the movement of that point. The radius of the circular motion is known as gyroradius and is defined as

$$r_g = \frac{P}{Bq},\ P = \frac{pc}{Ze}, \tag{3.12}$$

where P is known as magnetic rigidity, p is the momentum of the particle, c is the speed of light, Z is the charge of the particle in electron charge units and e is the unitary charge of the electron.

This gyroradius is essential towards understanding the effect of the magnetic field on particle since irregularities smaller than it do not affect the particle in measurable way but, if the dimension of the irregularities is the same as the gyroradius, the particle will begin a **random walk** process called diffusion.

3.4.1 Counting Particles

The transport equation is the equation of motion of a differential density through phase space[47].

Starting with considering an infinitesimal box of volume $\mathrm{d}^3r = r^2 \sin\theta \mathrm{d}r\mathrm{d}\theta\mathrm{d}\phi$ containing $N = n\mathrm{d}^3r$ particles inside. We also wish to characterize this density in a given interval of kinetic energy $(T, T+dT)$, so we define the differential density, U_T, such that all particles inside the volume are also in the same kinetic energy interval,

$$\mathrm{d}N = U_T\, \mathrm{d}^3r\, \mathrm{d}T = U_T\, r^2 \sin\theta\, \mathrm{d}r\, \mathrm{d}\theta\, \mathrm{d}\phi\, \mathrm{d}T. \tag{3.13}$$

This differential density can be defined as a function of rigidity or momentum as well (U_p, U_P), with the appropriate transformations ($U_P = (\beta c/A)U_T$).

This definition of differential density assumes an isotropic distribution of particles. The problem is that detectors do not measure differential densities, they measure differential intensities, so we must see how many of the particles in our volume will go through an infinitesimal area dA at any given time (as depicted in figure 3.10).

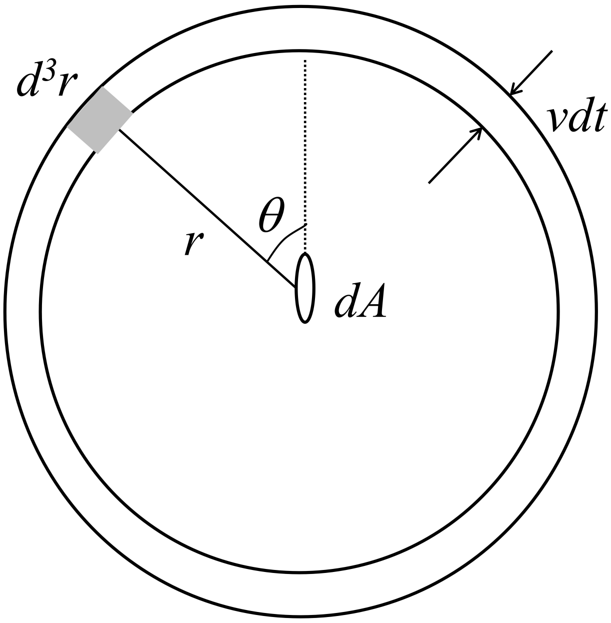

Figure 3.10: Intensity of particles going through the ring. [47]

The number of particles that go through the detector at some given time were moving towards the detector at a speed of v at a time prior to the detection(grey area in figure 3.10) is given by

$$\mathrm{d}n' = U_T\, \mathrm{d}^3r\, \mathrm{d}T = U_T\, r^2 \sin\theta\, v\mathrm{d}t\, \mathrm{d}\theta\, \mathrm{d}\phi\, \mathrm{d}T. \tag{3.14}$$

.

Since these particles are going in all directions, the fraction of them that will actually go through the detector is $\mathrm{d}A|\cos\theta|/4\pi r^2$, making the total number of particles from the previous volume that go through the detector after a time $\mathrm{d}t$ be,

$$\mathrm{d}n'' = \mathrm{d}n' \left(\frac{\mathrm{d}A|\cos\theta|}{4\pi r^2}\right) = U_T \left(\frac{\mathrm{d}A|\cos\theta|}{4\pi r^2}\right) r^2 \sin\theta\, v\mathrm{d}t\, \mathrm{d}\theta\, \mathrm{d}\phi\, \mathrm{d}T. \tag{3.15}$$

.

Integrating the previous expression over θ and ϕ, we get that the number of particles passing through the detector per unit of area, per unit of time, per unit of kinetic energy interval, is

$$j_T = \iint \mathrm{d}n'' \mathrm{d}\theta \mathrm{d}\phi = \frac{v\, U_T}{8\pi} = \left(\frac{A}{8Ze}\right) U_P. \tag{3.16}$$

Since it is common practice to think in terms of the particle distribution function rather than in terms of differential density U, the number of particles in any given point can be written as $\mathrm{d}n = F(\vec{r}, \vec{p}, t)\, \mathrm{d}^3 r\, \mathrm{d}^3 p$ and, from that, we can define our directional average of the distribution function as,

$$f(\vec{r}, p, t) = \frac{\int_\Omega F(\vec{r}, \vec{p}, t) \mathrm{d}\Omega}{\int_\Omega \mathrm{d}\Omega} = \frac{1}{4\pi} \int_\Omega F(\vec{r}, \vec{p}, t) \mathrm{d}\Omega \tag{3.17}$$

3.4.2 Cosmic Ray Transport Equation

Beginning from the continuity principle, we can now develop Parker's transport equation,

$$\frac{\mathrm{d}N}{\mathrm{d}t} = -\oint \vec{S} \cdot \mathrm{d}\vec{A} + Q, \tag{3.18}$$

which, according to the divergence theorem, $\oint \vec{S} \cdot \mathrm{d}\vec{A} = \int (\nabla \cdot \vec{S}) \mathrm{d}\tau$, where $\mathrm{d}\tau$ is the volume element within the surface $\oint \mathrm{d}\vec{a}$, and noting that $N = \int n \mathrm{d}\tau$, we can write out the differential form of the equation as,

$$\frac{\partial f}{\partial t} + \nabla \cdot \vec{S} = q', \tag{3.19}$$

where q' is the source/sink function per unit of volume.

The physics of the problem is contained in processes that cause a given flux $\vec{S}$ [47]. In our case, this flux consists for two parts, a diffusive flux and a convective flux.

3.4.3 Particle Diffusion and Drifts

When a particle encounters sudden changes in the magnetic field lines, its gyroradius abruptly changes (can get either squeezed by a stronger magnetic field or enlarged bye a weaker one). This causes the particle to attach itself to a neighbouring line. Since this is a random process, it leads to a diffusive flux perpendicular to the background magnetic field.

Diffusion parallel to the background magnetic field is studied under the so-called quasi-linear theory of scattering, which holds true for weak fluctuations. This theory goes back to the paper of Jokipii [34].

We can then write the diffusive flux as $\vec{S}_d = k_\parallel \nabla n_\parallel + k_\perp \nabla n_\perp$ (Fick's law), where both k's represent the respective diffusion coefficients. Usually $k_\perp \ll k_\parallel$. This is called the weak-scattering limit. The upper limit for the diffusion coefficients is when $k_\perp = k_\parallel$, in which case the fluctuations in the field are so high that they become as large as the background value, making the notion of a well-ordered background disappear and the diffusion becomes isotropic [47].

Another way to study this phenomenon is by studying the gradient and curvature drifts. It is possible to describe the drifts of particles, under the weak-scattering condition, using the following general expression, as given by Jokipii and Levy [37],

$$\langle \vec{v}_d \rangle = \frac{\beta P}{3} \nabla \times \frac{\vec{B}}{B^2}, \tag{3.20}$$

giving rise to a flux of the form,

$$\vec{S}_d = \frac{\beta P}{3B^2} \vec{B} \times \nabla n. \tag{3.21}$$

For the Parker field, the drift velocity becomes [56],

$$\langle \vec{v}_d \rangle = \frac{2pv(r-b)}{\pm B_0 r_0^2 3q(1+\gamma^2)^2}[1-2H(\theta-\theta_{\mathrm{HCS}})]\left[-\frac{\gamma}{\tan\theta}\vec{e}_r + (2+\gamma^2)\gamma\vec{e}_\theta + \frac{\gamma^2}{\tan\theta}\vec{e}_\phi\right], \tag{3.22}$$

where $\gamma = (r-b)\omega\sin\theta/V_w$, q is the charge, p the momentum and v the velocity.

The drift motion of particles in a magnetic field can be included into the diffusion formalist presented in the beginning of this section by writing it as an antisymmetric element of the cosmic ray diffusion tensor in the following way

$$\mathbf{k} = k_{ij} = \begin{pmatrix} k_{\|} & 0 & 0 \\ 0 & k_\perp & -k_T \\ 0 & k_T & k_\perp \end{pmatrix}, \tag{3.23}$$

where $k_T = \beta P/(3B)$, thus contracting the drift flux and the anisotropic diffusion into a single term, $-\mathbf{k}\cdot\nabla n$. This treatment of the drift effect is completely equivalent to direct usage of equation 3.20. This formalism was first used by Jokipii and Levy [37].

We can now simply write our flux as,

$$\vec{S} = \vec{V}n - \mathbf{k}\cdot\nabla n, \tag{3.24}$$

with $\vec{V}n$ as the simple convective drift of the Solar wind.

This leads us to $\partial n/\partial t + \nabla\cdot(\vec{V}n - \mathbf{k}\cdot\nabla n) = q'$ or, equivalently, $\partial f/\partial t + \nabla\cdot(\vec{V}f - \mathbf{k}\cdot\nabla f) = q$.

After taking this result into consideration and combining it with both the divergence of the flux in momentum space and the adiabatic cooling (this due to the act that particles ride with the fields in the wind and that these fields expand due to the positive divergence of the wind speed at a rate of change of momentum of $\langle\dot{p}\rangle/p = -(1/3)\nabla\cdot\vec{V}$) he reached the final form of the transport equation,

$$\frac{\partial f}{\partial t} + \nabla\cdot(\vec{V}f - \mathbf{k}\cdot\nabla f) - \frac{1}{3p^2}(\nabla\cdot\vec{V})\frac{\partial}{\partial p}(p^3 f) = q, \tag{3.25}$$

which has the simplest form (and the one we will be using further on)

$$\frac{\partial f}{\partial t} + \nabla\cdot(\vec{V}f - \mathbf{k}\cdot\nabla f) - \frac{1}{3}(\nabla\cdot\vec{V})\frac{\partial f}{\partial \ln p} = q. \tag{3.26}$$

As a final remark, the existence of a neutral current sheet, a discontinuity in the magnetic field, generates a drift of particles that follow it if they get close enough that their gyroradius intersects it, as depicted in figure 3.11. This drift is parallel to the surface and perpendicular to the magnetic field. Our calculation assumes that the HCS is locally flat enough to use the approximation of the drift over a flat surface, as was done by Burger et al. [11]. Our expression for this drift then becomes,

$$\left\langle \vec{V}_d \right\rangle = \frac{2pv(r-b)}{\pm B_0 r_0^2 3q(1+\gamma^2)}\delta(\theta-\theta_{\mathrm{HCS}})(\gamma\vec{e}_r + \vec{e}_\phi), \tag{3.27}$$

where $\gamma = (r-b)\omega\sin\theta/V_w$, q is the charge, p the momentum and v the velocity. Burger [12] introduced a parametrization that requires a calculation of the normal to the HCS at every point and the distance to it, which can be quite cumbersome. We shall use the first one in our simulations.

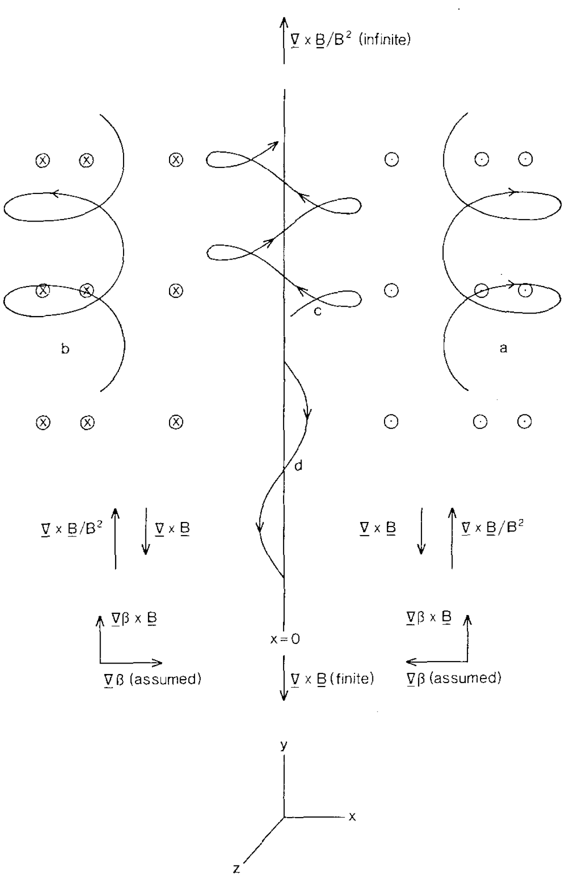

Figure 3.11: Trajectories of positively charged particles in and near a neutral plane [11].

Lastly, another approach was suggested by Potgieter and Moraal [57]. In their paper they studied the 2D model (r and θ) and, due to simetry, the study was only done in $0 < \theta < \pi/2$. He suggested that a transition function could be created so that it was simpler to compute the numerical model near the HCS. This function introduces a drift so that the nothern hemisphere of the heliosphere is defined not with a wavy bottom (due to the HCS) but instead with a flat surface. The required drift velocity had the form

$$\left\langle \vec{V_d} \right\rangle = \frac{K_T \sin\Psi}{r}\left[-\left(2\cos^2\Psi\cot\theta + \frac{\dot{\mathrm{f}}}{\mathrm{f}}\right)\vec{e}_r + 2(\cos^2\Psi + 1)\vec{e}_\theta - \left(2\sin^2\Psi\cot\theta + \frac{\dot{\mathrm{f}}}{\mathrm{f}}\right)\vec{e}_\phi\right], \quad (3.28)$$

where $\Psi = \arctan(r\omega/V_w)$, known as the Parker spiral angle, the f, the smoothing function, is defined as

$$f(\theta) = \frac{1}{\alpha}\arctan\left[\left(1 - \frac{2\theta}{\pi}\right)\tan\alpha\right],$$

and α is

$$\alpha = \arccos\left(\frac{\pi}{2\theta_{1/2}} - 1\right).$$

This method was not used in this work but, for completude sake, had to be mentioned.

3.5 Solutions to the Transport Equation

Now that the mechanism behind Solar modulations is understood, ways to solve the transport equation can be sought.

Three methods will be used to solve the transport equation: the **Force-Field** aproximation, the 1D numerical solution and the 2D numerical solution, which will include the drift due to the wavy neutral current sheet (HCS).

Expanding equation 3.26 in 3 dimensions gives

$$\begin{aligned}\frac{\partial f}{\partial t} &= k_{rr}\frac{\partial^2 f}{\partial r^2} + \frac{k_{\theta\theta}}{r^2}\frac{\partial^2 f}{\partial \theta^2} + \frac{k_{\phi\phi}}{r^2\sin^2\theta}\frac{\partial^2 f}{\partial \phi^2} \\ &+ \frac{k_{\theta r}+k_{r\theta}}{r}\frac{\partial^2 f}{\partial r\partial\theta} + \frac{k_{\phi r}+k_{r\phi}}{r\sin\theta}\frac{\partial^2 f}{\partial r\partial\phi} + \frac{k_{\phi\theta}+k_{\theta\phi}}{r^2\sin\theta}\frac{\partial^2 f}{\partial\theta\partial\phi} \\ &+ \left(\frac{2k_{rr}}{r} + \frac{\cot\theta k_{\theta r}}{r} + \frac{1}{r\sin\theta}\frac{\partial k_{\phi r}}{\partial\phi} + \frac{1}{r}\frac{\partial k_{\theta r}}{\partial\theta} + \frac{\partial k_{rr}}{\partial r}\right)\frac{\partial f}{\partial r} \\ &+ \left(\frac{k_{r\theta}}{r^2} + \frac{\cot\theta k_{\theta\theta}}{r^2} + \frac{1}{r^2\sin\theta}\frac{\partial k_{\phi\theta}}{\partial\phi} + \frac{1}{r^2}\frac{\partial k_{\theta\theta}}{\partial\theta} + \frac{1}{r}\frac{\partial k_{r\theta}}{\partial r}\right)\frac{\partial f}{\partial\theta} \\ &+ \left(\frac{k_{r\phi}}{r^2\sin\theta} + \frac{1}{r^2\sin^2\theta}\frac{\partial k_{\phi\phi}}{\partial\phi} + \frac{1}{r^2\sin\theta}\frac{\partial k_{\theta\phi}}{\partial\theta} + \frac{1}{r\sin\theta}\frac{\partial k_{r\phi}}{\partial r}\right)\frac{\partial f}{\partial\phi} \\ &- \left(V_{wr}\frac{\partial f}{\partial r} + \frac{V_{w\theta}}{r}\frac{\partial f}{\partial\theta} + \frac{V_{w\phi}}{r\sin\theta}\frac{\partial f}{\partial\phi}\right) \\ &+ \frac{1}{3}\left(\frac{2}{r}V_{wr} + \frac{\cos\theta}{r\sin\theta}V_{w\theta} + \frac{1}{r\sin\theta}\frac{\partial V_{w\phi}}{\partial\phi} + \frac{1}{r}\frac{\partial V_{w\theta}}{\partial\theta} + \frac{\partial V_{wr}}{\partial r}\right)\frac{\partial f}{\partial\ln p}\end{aligned} \tag{3.29}$$

If only the r and θ directions are considered and the Parker model for the magnetic field (i.e. radial Solar wind and dipole magnetic field) is assumed we get,

$$\begin{aligned}\frac{\partial f}{\partial t} &= k_{rr}\frac{\partial^2 f}{\partial r^2} + \frac{k_{\theta\theta}}{r^2}\frac{\partial^2 f}{\partial\theta^2} \\ &+ \left(\frac{2k_{rr}}{r} + \frac{\cot\theta k_{\theta r}}{r} + \frac{1}{r}\frac{\partial k_{\theta r}}{\partial\theta} + \frac{\partial k_{rr}}{\partial r}\right)\frac{\partial f}{\partial r} \\ &+ \left(\frac{k_{r\theta}}{r^2} + \frac{\cot\theta k_{\theta\theta}}{r^2} + \frac{1}{r^2}\frac{\partial k_{\theta\theta}}{\partial\theta} + \frac{1}{r}\frac{\partial k_{r\theta}}{\partial r}\right)\frac{\partial f}{\partial\theta} \\ &- V_{wr}\frac{\partial f}{\partial r} + \frac{2V_{wr}}{3r}\frac{\partial f}{\partial\ln p}\end{aligned} \tag{3.30}$$

From equation 3.20 we can see that,

$$\begin{aligned}(\nabla\cdot k_T)_r &= \frac{1}{r}\frac{\partial k_{\theta r}}{\partial\theta} + \frac{\cot\theta}{r}k_{\theta r} = V_{gr}, \\ (\nabla\cdot k_T)_\theta &= \frac{\partial k_{r\theta}}{\partial r} + \frac{k_{r\theta}}{r} + \frac{1}{r\sin\theta}\frac{\partial k_{\phi\theta}}{\partial\phi} = V_{g\theta}, \\ (\nabla\cdot k_T)_\phi &= \frac{1}{r}\frac{\partial k_{\theta\phi}}{\partial\theta} = V_{g\phi},\end{aligned} \tag{3.31}$$

which makes equation 3.30 become,

$$\begin{aligned}\frac{\partial f}{\partial t} &= k_{rr}\frac{\partial^2 f}{\partial r^2} + \frac{k_{\theta\theta}}{r^2}\frac{\partial^2 f}{\partial\theta^2} + \left(\frac{2k_{rr}}{r} + \frac{\partial k_{rr}}{\partial r} - V_{wr} + V_{gr}\right)\frac{\partial f}{\partial r} \\ &+ \left(\frac{\cot\theta k_{\theta\theta}}{r} + V_{g\theta}\right)\frac{1}{r}\frac{\partial f}{\partial\theta} + \frac{2V_{wr}}{3r}\frac{\partial f}{\partial\ln p}.\end{aligned} \tag{3.32}$$

These drift velocities were calculated in 3.22.

Since the diffusion tensor was defined in terms of the parallel and perpendicular directions to the magnetic field lines, the coordinate transformation from the spherical referential to the magnetic field referential has to be calculated. As can be seen in equation 3.11, the magnetic field has no θ component. This simplifies the problem since we can start by defining the θ direction as $\vec{e}_{\perp\theta}$, making

$\vec{e}_{\parallel} = \frac{\overrightarrow{B}}{B}$ and the third as perpendicular to the other two,

$$\begin{aligned} \vec{e}_{\parallel} &= \cos\Psi\vec{e}_r - \sin\Psi\vec{e}_\phi \\ \vec{e}_{\perp\theta} &= \vec{e}_\theta \\ \vec{e}_{\perp r} &= \vec{e}_{\parallel} \times \vec{e}_{\perp\theta}. \end{aligned} \tag{3.33}$$

This gives out the following change of coordinates between the two systems,

$$\begin{pmatrix} k_{\mathrm{rr}} & k_{\mathrm{r}\theta} & k_{\mathrm{r}\phi} \\ k_{\theta\mathrm{r}} & k_{\theta\theta} & k_{\theta\phi} \\ k_{\phi\mathrm{r}} & k_{\phi\theta} & k_{\phi\phi} \end{pmatrix} = \begin{pmatrix} k_{\parallel}\cos^2\Psi + k_{\perp\mathrm{r}}\sin^2\Psi & -k_{\mathrm{T}}\sin\Psi & (k_{\perp\mathrm{r}} - k_{\parallel})\cos\Psi\sin\Psi \\ k_{\mathrm{T}}\sin\Psi & k_{\perp\theta} & k_{\mathrm{T}}\cos\Psi \\ (k_{\perp\mathrm{r}} - k_{\parallel})\cos\Psi\sin\Psi & -k_{\mathrm{T}}\cos\Psi & k_{\parallel}\sin^2\Psi + k_{\perp\mathrm{r}}\cos^2\Psi, \end{pmatrix} \tag{3.34}$$

where $\tan\Psi = \frac{\omega(r-b)\sin\theta}{V_w}$. This transformation was the same used in Burger et al. [13].

The coefficient chosen in this work was the one used by Pei et al. [55]. Even though there is still constant debate over the general form of the diffusion coefficient, one of the most used as a benchmark [10, 35, 42] (which comes from Quasi-Linear Theory (QLT) of plasma) is

$$k_{\parallel} = k_0\beta P\frac{B_{\odot}}{B}, \tag{3.35}$$

where $B_{\odot}$ is the Solar magnetic field measured near Earth.

For the perpendicular diffusion coeficient, a common choice is $k_{\perp}/k_{\parallel} = 0.1$. Ways to determine the appropriate diffusion coefficient usually envolve the study of turbulence models based on spacecraft measurements [54, 71], which is out of the scope of this work.

Some times the following simpler version is used [36, 47],

$$k_{\parallel} = k_0\beta P. \tag{3.36}$$

3.5.1 The Local Interstellar Flux

The Solar modulation of Galactic cosmic-rays is an initial-value problem, one must somehow know what the Galactic cosmic ray spectrum is before we can estimate how the Solar magnetic field affects it. The initial spectra used in the solutions to follow were those introduced by Webber and Higbie [68]. They were created using a Monte-Carlo Diffusion model and a Leaky Box Model for the propagation in the Galaxy and based on data provided from the Voyager 1 experiment (as can be seen in figure 3.12). Their forms are given by

$$\begin{aligned} J_{\mathrm{LIS}}^{\mathrm{Proton}}(T) = \frac{dN}{dT} &= \frac{18.9\left(\frac{T}{1\,\mathrm{GeV}}\right)^{-2.79}}{1 + 6.75\left(\frac{T}{1\,\mathrm{GeV}}\right)^{-1.22} + 1.30\left(\frac{T}{1\,\mathrm{GeV}}\right)^{-2.80} + 0.0087\left(\frac{T}{1\,\mathrm{GeV}}\right)^{-4.32}}, \\ J_{\mathrm{LIS}}^{\mathrm{Helium}}(T) = \frac{dN}{dT} &= \frac{0.99\left(\frac{T}{1\,\mathrm{GeV}}\right)^{-2.77}}{1 + 4.14\left(\frac{T}{1\,\mathrm{GeV}}\right)^{-1.09} + 0.65\left(\frac{T}{1\,\mathrm{GeV}}\right)^{-2.79} + 0.0094\left(\frac{T}{1\,\mathrm{GeV}}\right)^{-4.20}}. \end{aligned} \tag{3.37}$$

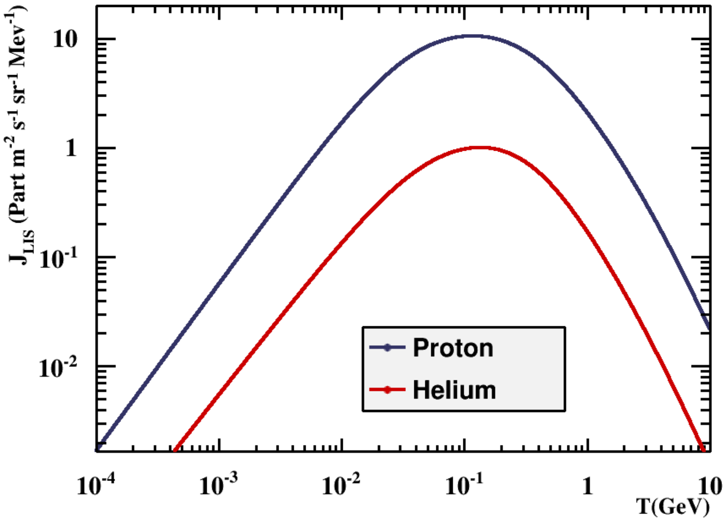

Figure 3.12: Local Interstellar primary cosmic ray flux for protons and helium nuclei [68].

3.5.2 Force-Field Solution

In 1968, Gleeson and Axford [25] proposed a solution to the cosmic ray transport equation, the **Force-Field** solution. Due to its simplicity, this is the most used approximation to describe the Solar modulation phenomenon. It takes the final form of

$$\frac{J(r,E)}{E^2 - E_0^2} = \frac{J_{\mathrm{LIS}}(E+\Phi)}{(E+\Phi)^2 - E_0^2}, \tag{3.38}$$

where J is the observed intensity, E is the total energy and Φ is the so-called Force-Field energy loss that particles suffer as they propagate inwards into the heliosphere.

In the literature, the most commonly used modulation parameter is not Φ but ϕ which comes from $\phi = \Phi/(Ze)$. Since Φ represents an energy lost, the ϕ represents a modulation potential. In this view, Gleeson and Urch [26], in 1973, re-derived the Force-Field solution in a more transparent way, which will be presented here.

This solution comes from assuming that the Solar wind is constant, the diffusion coefficient is isotropic, the solution is spherically symmetric, that there is no drift and, in addition, that the solution is stationary ($\frac{\mathrm{d}f}{\mathrm{d}r} = 0$) and steady-state, which leads to

$$\frac{VP}{3}\frac{\partial f}{\partial P} - k\frac{\partial f}{\partial r} = 0. \tag{3.39}$$

The solutions of 3.39 are characteristic curves where f is constant in the (r,P) plane since

$$\frac{\mathrm{d}f}{\mathrm{d}r} = \frac{\partial f}{\partial r} + \frac{\partial P}{\partial r}\frac{\partial f}{\partial P} = 0, \tag{3.40}$$

which in turn implies,

$$\frac{\partial P}{\partial r} = \frac{VP}{3k}. \tag{3.41}$$

If $k = k_0\beta P$, which is one result of QLT, we get

$$\frac{\partial P}{\partial r} = \frac{VP}{3k_0\beta P}, \tag{3.42}$$

or

$$\beta\frac{\partial P}{\partial r} = \frac{V}{3k_0}, \tag{3.43}$$

which amounts to

$$\frac{\partial E}{\partial r} = \frac{V}{3k_0}, \tag{3.44}$$

since $\mathrm{d}E/\mathrm{d}P = \beta$. Integrating both side in $\mathrm{d}r$ from some distance r up to the heliosphere (r_H), we get

$$E(r = r_H) - E(r) = \Phi_{SM}\frac{r_H - r}{r_H - 1(AU)},\ \Phi_{SM} = \int_{1\,AU}^{r_H} \frac{V}{3k_0}dr = V\frac{r_H - 1}{3k_0}. \tag{3.45}$$

Finally, since f is constant along the characteristic curve

$$f(1AU, E(r_H) - \Phi_{SM}) = f(r_H, E(r_H)) \implies \frac{J_T(1AU, E(r_H) - \Phi_{SM})}{(E(r_H) - \Phi_{SM})^2 - m^2)} = \frac{J_T(r_H, E(r_H))}{E^2(r_H) - m^2}, \tag{3.46}$$

or, rearranging the terms and making them clearer, so that the flux becomes a function of energy measured in Earth instead of original energy,

$$J_T(1\,AU, E) = J_{\mathrm{LIS}}(E + \Phi_{SM})\frac{E^2 - m^2}{((E + \Phi_{SM})^2 - m^2)}. \tag{3.47}$$

Typical values range from 0.2 GeV to 1.3 GeV [66]. It is important to emphasize that this is only valid in the case where $k \propto P$.

This analytical solution is a good way to parametrize the problem in broad terms, it describes the entire Solar modulation phenomenon as a simple mean energy loss suffered by Galactic cosmic rays as they traverse the heliosphere. This simple solution does not take into account the particular shape of the magnetic field and assumes a diffusion coefficient proportional to $k \propto P$. Since Parker's transport equation does not have an analytical solution in its most complex form (taking into account complex drifts, diffusion coefficients and the general shape of the magnetic field), the only way to properly include all effects is to solve it numerically, which will be the focus of the sections to come.

3.5.3 Finite Difference Method

Numerical resolution of differential equations involves a discretization of space and the corresponding approximation to all derivatives. These are known as the Finite Difference Methods.

The discretization chosen was

$$\begin{aligned} r_i &= i\,h + r_0 \\ \theta_j &= j\,l + \theta_0 \\ p_n &= p_0\,e^{-n\,k}, \end{aligned} \tag{3.48}$$

where the minus sign in p_n was chosen since the solution will be taken as walking from the maximum momentum to the minimum.

The most general numerical method for solving differential equations is the Euler method which makes use of the first order approximation of Taylor series expansion. The 1D numerical solution demands the usage of another scheme, the Crank-Nicolson scheme.

Going from forward Euler method to Crank-Nicolson consists of taking the average between the derivative at time $n+1$ and at time n, leading to the following discrete first and second derivatives,

$$\begin{aligned} \left.\frac{\partial f}{\partial x}\right|_i^n &\approx \frac{f_{i+1}^{n+1} - f_{i-1}^{n+1} + f_{i+1}^n - f_{i-1}^n}{4\Delta x} \\ \left.\frac{\partial^2 f}{\partial x^2}\right|_i^n &\approx \frac{f_{i+1}^{n+1} - 2f_i^{n+1} + f_{i-1}^{n+1} + f_{i+1}^n - 2f_i^n + f_{i-1}^n}{2\Delta x^2}, \end{aligned} \tag{3.49}$$

Crank-Nicolson scheme creates an implicit solution to the problem. Instead of having an explicit system in which the next iteration $f(i, j, n+1)$ is a function of only previous iterations in time (or momentum), $f(i, j, n+1) = g[f(i, j, n), f(i+1, j, n), ...]$, in the implicit case the next iteration is a linear combination of several steps from both the current and the next iteration. This demands the solving of a linear system of equations (as seen in figure 3.13).

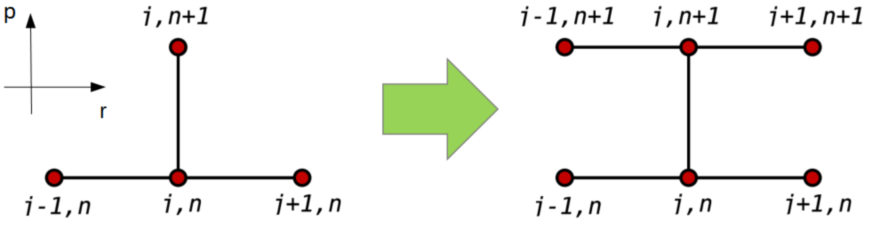

Figure 3.13: Comparison of the computational molecules between forward Euler method and Crank-Nicolson.

The 2D equation will use an alternative method, the Alternating Direction Implicit method

3.5.4 1D Numerical Solution

The one-dimensional solution to the Parker transport equation stands on some of the same approximations as the Force-Field equation, it takes into consideration a flat Solar wind speed, a solution variable with r, adiabatic energy lost, and particle drifts. Aside from a complex diffusion coefficient that varies with the magnetic field, this solution, same as in the Force-Field, does not take into account the complex structure of the magnetic field.

Considering solely the r direction we can rewrite the Parker equation as

$$\frac{\partial f}{\partial t} = k_{rr}\frac{\partial^2 f}{\partial r^2} + \left(\frac{2k_{rr}}{r} + \frac{\partial k_{rr}}{\partial r} - V_{wr} + V_{gr}\right)\frac{\partial f}{\partial r} + \frac{2V_{wr}}{3r}\frac{\partial f}{\partial \ln p}. \tag{3.50}$$

By defining redefining the first and second derivative operator, with respect to X, as δ_X and δ_{XX}, respectively, the steady state Parker transport equation for one dimension can be rewritten as

$$a\,\delta_{rr}f + b\,\delta_r f + c\,\delta_{\ln p}f = 0, \tag{3.51}$$

by making use of the following substitutions,

$$\begin{aligned} a &= k_{rr}, \\ b &= \left(\frac{2k_{rr}}{r} + \frac{\partial k_{rr}}{\partial r} - V_{wr} + V_{gr}\right), \\ c &= \frac{2V_{wr}}{3r}. \end{aligned} \tag{3.52}$$

As seen previously, passing equation 3.51 to the finite difference framework in a Crank-Nicolson scheme gives rise to

$$\begin{aligned} a\,\frac{f_{i+1}^{n+1} - 2f_i^{n+1} + f_{i-1}^{n+1} + f_{i+1}^{n} - 2f_i^{n} + f_{i-1}^{n}}{2\Delta x^2} + b\,\frac{f_{i+1}^{n+1} - f_{i-1}^{n+1} + f_{i+1}^{n} - f_{i-1}^{n}}{4\Delta x} + \\ + c\,\frac{f_{i+1}^{n+1} - f_{i-1}^{n+1} + f_{i+1}^{n} - f_{i-1}^{n}}{4\Delta \ln p} = 0. \end{aligned} \tag{3.53}$$

The equation can be made adimensional by dividing the variable r (since θ is adimensional already) by a scale factor, meaning

$$r = s_r\, r^* \implies \frac{\partial f}{\partial r} = \frac{1}{s_r}\frac{\partial f}{\partial r^*}. \tag{3.54}$$

This allows for a reduction in truncation error and for a better understanding of how stability changes with the parameters of the equation.

Making the apropriate substitutions we can see that equation 3.53 can be rewritten in the following fashion,

$$\begin{aligned}&\overbrace{\left(\frac{a}{2h^2}+\frac{b}{4h}\right)}^{C_i} f_{i+1}^{n+1} + \overbrace{\left(-\frac{a}{h^2}+\frac{c}{k}\right)}^{B_i} f_i^{n+1} + \overbrace{\left(\frac{a}{2h^2}-\frac{b}{4h}\right)}^{A_i} f_{i-1}^{n+1} = \\ &\qquad = \underbrace{\left(-\frac{a}{2h^2}-\frac{b}{4h}\right) f_{i+1}^{n} + \left(\frac{a}{h^2}+\frac{c}{k}\right) f_i^{n} + \left(-\frac{a}{2h^2}+\frac{b}{4h}\right) f_{i-1}^{n}}_{D_i}\end{aligned} \tag{3.55}$$

which, when written in a matrix form, is simply

$$\begin{pmatrix} \mathrm{B_0} & \mathrm{C_0} & 0 & \cdots & 0 \\ \mathrm{A_1} & \mathrm{B_1} & \mathrm{C_1} & \cdots & 0 \\ 0 & \mathrm{A_2} & \mathrm{B_2} & \mathrm{C_2} & 0 \\ \vdots & \vdots & \vdots & \ddots & \vdots \\ 0 & 0 & 0 & \mathrm{A_{i_{max}}} & \mathrm{B_{i_{max}}} \end{pmatrix} \begin{bmatrix} \mathrm{f_0^{n+1}} \\ \mathrm{f_1^{n+1}} \\ \mathrm{f_2^{n+1}} \\ \vdots \\ \mathrm{f_{i_{max}}^{n+1}} \end{bmatrix} = \begin{pmatrix} \mathrm{D_0} \\ \mathrm{D_1} \\ \mathrm{D_2} \\ \vdots \\ \mathrm{D_{i_{max}}} \end{pmatrix} \tag{3.56}$$

For each momentum step, n, the matrix system has to be solved for all radial positions, i. The tridiagonal matrix in the left is evaluated at momentum step $n+1$ while the vector with the elements named D_i is evaluated for step n. By solving this matrix in a loop, and using the solution from the previous iteration, the next iteration can be calculated.

These sort of systems are very particular and involve only first neighbours of the current point (n, i) being evaluated, making the matrix one with three diagonals and zeros elsewhere. This simple matrix can be rewriten based on each row in the following way,

$$\begin{aligned}&A_i f_{i-1} + B_i f_i + C_i f_{i+1} = D_i,\ i = 0,\ 1,\ ...,\ i_{\max}\\ &A_0 = 0\\ &C_{i_{\max}} = 0.\end{aligned} \tag{3.57}$$

This way of writing it will be useful for solving it in an optimized way.

To solve this matrix we can make use of the **Tridiagonal Matrix Algorithm**, also known as Thomas algorithm (named after Llewellyn Thomas), which consists of the following steps,

$$\begin{aligned}&C'_i = \begin{cases} \frac{C_i}{B_i} & i = 0 \\ \frac{C_i}{B_i - A_i C'_{i-1}} & i = 1, 2, ..., i_{\max} - 1 \end{cases}\\ &D'_i = \begin{cases} \frac{D_i}{B_i} & i = 0 \\ \frac{D_i - A_i D'_{i-1}}{B_i - A_i C'_{i-1}} & i = 1, 2, ..., i_{\max} - 1 \end{cases}\\ &f_{i_{\max}} = D'_{i_{\max}}\\ &f_i = D'_i - C'_i f_{i+1},\ i = i_{\max} - 1, i_{\max} - 2, ..., 1, 0\end{aligned} \tag{3.58}$$

Because this is a parabolic equation, we need an initial condition and two boundary conditions. Solar modulation is a phenomenon that affects low energy particles, high energy particles are less affected by magnetic fields since their rigidity becomes very high. If the flux measured is $J_T = p^2 f$, as we saw in section 3.4.1, for a big enough p we have that

$$J_T(r, p_{max}) = J_{\mathrm{LIS}}(p_{max}). \tag{3.59}$$

This is our initial condition and we are going to go down in energy from the arbitrary maximum of the simulation. This is a good aproximation if we choose a momentum high enough.

The boundary conditions are at $r = b$ (place after which the Solar wind becomes radial, as seen in section 3.2), and at $r = r_{\mathrm{heliopause}}$ (after which the Solar plasma should end). Since we are working with the densitiy of cosmic rays, the flux $S = 4\pi p^2 \left(V_w - k\frac{\partial f}{\partial r}\right)$ must vanish at the origin ($r = b$). The other boundary condition comes from the fact that there should be no modulation in the absence of plasma, meaning that,

$$\begin{aligned} \left.\frac{\partial f}{\partial r}\right|_{r=b} &= 0 \\ J_T(r_{max}, p) &= J_{\text{LIS}}(p). \end{aligned} \tag{3.60}$$

The 1D resolution included a flat Solar wind speed of $\vec{V_w} = 400\text{kms}^{-1}\vec{e}_r$ and a diffusion coefficient of the form

$$k_\parallel = k_0 \beta P \frac{B_\odot}{B} \quad \text{with} \quad k_0 = 4.56 \times 10^{22}\text{cm}^2\text{s}^{-1} \tag{3.61}$$

3.5.5 2D Numerical Solution

The two-dimensional solution to the Parker transport equation uses almost all the same approximations as the 1D solution but, besides including variation in θ coordinate, includes the complex particle drifts due to gradient and divergence in the Parker magnetic field and the HCS drift. Same as in the 1D solution, the 2D solution will also be calculated in the steady state regime ($\frac{\partial f}{\partial t} = 0$).

Solving a 2D in space equation using the Crank-Nicolson method generates a very complex set of equations. An alternative to solving a parabolic equation with two dimensions in space was developed by Peaceman and Rachford [53]. This method has the particularity that it is unconditionably stable for any Δt chosen (which in our case is $\Delta \ln p$). This stability criteria does not apply to the other coordinates, which was duly demonstrated by the number of steps needed to be employed in order to get a stable solution (for protons, around 400 steps in momentum, 2000 steps in R and 400 steps in θ). If the models have faster varying derivatives in the coefficients or some of the constants change, a more abundant number of steps has to be employed.

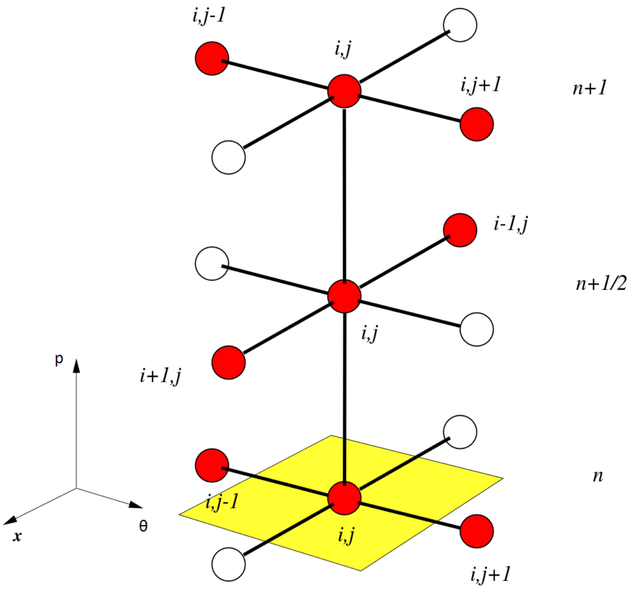

Figure 3.14: Scheme showing the computational molecules of the ADI method.

Same as before, the system goes from the analytical form

$$\begin{aligned} \frac{\partial f}{\partial t} = k_{rr}\frac{\partial^2 f}{\partial r^2} + \frac{k_{\theta\theta}}{r^2}\frac{\partial^2 f}{\partial \theta^2} + \left(\frac{2k_{rr}}{r} + \frac{\partial k_{rr}}{\partial r} - V_{wr} + V_{gr}\right)\frac{\partial f}{\partial r} \\ + \left(\frac{\cot\theta k_{\theta\theta}}{r} + V_{g\theta}\right)\frac{1}{r}\frac{\partial f}{\partial \theta} + \frac{2V_{wr}}{3r}\frac{\partial f}{\partial \ln p}, \end{aligned} \tag{3.62}$$

to the simplified form,

$$\begin{aligned}
&a\,\delta_{rr}f + b\,\delta_{\theta\theta}f + c\,\delta_r f + d\,\delta_\theta f + e\,\delta_{\ln p}f = 0\\
&a = k_{rr},\\
&b = \frac{k_{\theta\theta}}{r^2},\\
&c = \left(\frac{2k_{rr}}{r} + \frac{\partial k_{rr}}{\partial r} - V_{wr} + V_{gr}\right),\\
&d = \left(\frac{\cot\theta k_{\theta\theta}}{r} + V_{g\theta}\right),\\
&e = \frac{2V_{wr}}{3r}.
\end{aligned} \tag{3.63}$$

This equation is far more complicated to solve, it involves solving an equation with two spacial dimensions and one momentum dimension. To solve this type of system a method was used where the iteration $n \to n+1$ is taken in two half steps $n \to n+1/2 \to n+1$. This method is called Alternating Direction Implicit (ADI) and it's a two step numerical scheme which involves solving a forward in time centred in space finite difference system twice. Its particularity is that the forward in time derivation is done for one of the spacial coordinates at a time, as is shown in figure 3.14.

Rewriting expression 3.63 in the ADI finite difference scheme gives

$$\begin{aligned}
&\textbf{1)}\quad a\delta_{rr}f^{n+1/2} + b\delta_{\theta\theta}f^{n} + c\delta_r f^{n+1/2} + d\delta_\theta f^{n} + e\delta_{\ln p}f^{n} = 0\\
&\textbf{2)}\quad a\delta_{rr}f^{n+1/2} + b\delta_{\theta\theta}f^{n+1} + c\delta_r f^{n+1/2} + d\delta_\theta f^{n+1} + e\delta_{\ln p}f^{n+1/2} = 0.
\end{aligned} \tag{3.64}$$

Substituting the finite difference derivatives and solving the resulting system (same as in the 1D case), one gets

$$\begin{aligned}
&\textbf{1)}\quad \overbrace{\left(\frac{a}{h^2} + \frac{c}{2h}\right)}^{C_i} f^{n+1/2}_{i+1,j} + \overbrace{\left(-\frac{2a}{h^2} + \frac{e}{2k}\right)}^{B_i} f^{n+1/2}_{i,j} + \overbrace{\left(\frac{a}{h^2} - \frac{c}{2h}\right)}^{A_i} f^{n+1/2}_{i-1,j} =\\
&\qquad = \underbrace{\left(-\frac{b}{l^2} - \frac{d}{2l}\right) f^{n}_{i,j+1} + \left(\frac{2b}{l^2} + \frac{e}{2k}\right) f^{n}_{i,j} + \left(-\frac{b}{l^2} + \frac{d}{2l}\right) f^{n}_{i,j-1}}_{D_i}\\
&\textbf{2)}\quad \overbrace{\left(\frac{b}{l^2} + \frac{d}{2l}\right)}^{C'_j} f^{n+1}_{i,j+1} + \overbrace{\left(-\frac{2b}{l^2} + \frac{e}{2k}\right)}^{B'_j} f^{n+1}_{i,j} + \overbrace{\left(-\frac{b}{l^2} - \frac{d}{2l}\right)}^{A'^j} f^{n+1}_{i,j-1} =\\
&\qquad = \underbrace{\left(-\frac{a}{h^2} - \frac{c}{2h}\right) f^{n+1/2}_{i+1,j} + \left(\frac{2a}{h^2} + \frac{e}{2k}\right) f^{n+1/2}_{i,j} + \left(-\frac{a}{h^2} + \frac{c}{2h}\right) f^{n+1/2}_{i-1,j}}_{D'_j}
\end{aligned} \tag{3.65}$$

As expected, instead of one matrix system to solve, there are two,

$$\begin{aligned}
&\textbf{1)}\quad \begin{pmatrix} ... & ... & ... & ... & ... \\ A_{j-1} & B_{j-1} & C_{j-1} & 0 & ... \\ 0 & A_j & B_j & C_j & 0 \\ ... & 0 & A_{j+1} & B_{j+1} & C_{j+1} \\ ... & ... & ... & ... & ... \end{pmatrix} \begin{bmatrix} ... \\ f^{n+1/2}_{i-1,j} \\ f^{n+1/2}_{i,j} \\ f^{n+1/2}_{i+1,j} \\ ... \end{bmatrix} = \begin{pmatrix} ... \\ D_{j-1} \\ D_j \\ D_{j+1} \\ ... \end{pmatrix}\\
&\textbf{2)}\quad \begin{pmatrix} ... & ... & ... & ... & ... \\ A_{i-1} & B_{i-1} & C_{i-1} & 0 & ... \\ 0 & A_i & B_i & C_i & 0 \\ ... & 0 & A_{i+1} & B_{i+1} & C_{i+1} \\ ... & ... & ... & ... & ... \end{pmatrix} \begin{bmatrix} ... \\ f^{n+1}_{i,j-1} \\ f^{n+1}_{i,j} \\ f^{n+1}_{i,j+1} \\ ... \end{bmatrix} = \begin{pmatrix} ... \\ D'_{i-1} \\ D'_i \\ D'_{i+1} \\ ... \end{pmatrix}.
\end{aligned} \tag{3.66}$$

In general terms, we first calculate the entire solution for a given P in slices of constant r, running over θ, after which, we run those values over the second system of equations in slices of constant θ, running over r.

Similarly to the 1-dimensional case, we have a parabolic equation but, in this case its 2-dimensional in space and 1-dimensional in time. This requires us to have one initial value and four boundary conditions. The boundary conditions in r will be the same as 1D but the θ coordinate demands we take another two in consideration.

As before, since Solar modulation is a phenomenon that affects low energy particles, meaning that our initial condition in $P = P_{\max}$ will again be

$$J_T(r, \theta, p_{max}) = J_{\text{LIS}}(p_{max}). \tag{3.67}$$

The boundary conditions at $r = b$ and at $r = r_{heliopause}$ is as before

$$\begin{aligned} \left.\frac{\partial f}{\partial r}\right|_{r=b} &= 0 \\ J_T(r_{max}, \theta, p) &= J_{\text{LIS}}(p). \end{aligned} \tag{3.68}$$

Due to a ϕ-symmetry, we can consider that at $\theta = 0$ and at $\theta = \pi$, the gradient of the density function in the θ direction should be 0 since,

$$\begin{aligned} \phi - \text{symmetry} \implies & f(r, \theta, \phi) = f(r, \theta, \phi + \delta), \forall_\delta \\ & f(r, 0 - \epsilon, \phi) = f(r, 0 + \epsilon, \phi + \pi) = f(r, \epsilon, \phi) \\ & f(r, -\epsilon, \phi) = f(r, \epsilon, \phi) \implies \left.\frac{\partial f}{\partial \theta}\right|_{\theta=0} = 0 \end{aligned} \tag{3.69}$$

The same exact logic can be applied to the other pole of the sphere, thus showing our other two boundary conditions,

$$\begin{aligned} \left.\frac{\partial f}{\partial \theta}\right|_{\theta=0} &= 0 \\ \left.\frac{\partial f}{\partial \theta}\right|_{\theta=\pi} &= 0 \end{aligned} \tag{3.70}$$

The diffusion coefficient, magnetic field and Solar wind used were the same as in the 1D case. The tilt angle used was $\alpha = 30\,\text{deg}$. This two dimensional simulation included additionally the drift by the heliospheric neutral current sheet as given by

$$\left\langle \vec{V_d} \right\rangle = \frac{2pv(r-b)}{\pm B_0 r_0^2 3q(1+\gamma^2)} \delta(\theta - \theta_{\text{HCS}})(\gamma \vec{e}_r + \vec{e}_\phi), \tag{3.71}$$

where $\gamma = (r - b)\omega \sin\theta / V_w$, q is the charge, p the momentum, v the velocity and θ_{HCS} as given by

$$\theta_{\text{HCS}} = \frac{\pi}{2} - \arctan\left[\tan\alpha \sin\left(\phi - \frac{\omega(r-b)}{v_w}\right)\right]. \tag{3.72}$$

3.6 Results from numerical simulation

3.6.1 Force-Field and 1D numerical solutions

We now present the results for the numerical simulations for a maximum momentum of 100 GV (even though the plots are shown in terms of kinetic energy per nucleon since those are the units commonly used in the field) and a heliosphere of 90 AU radius.

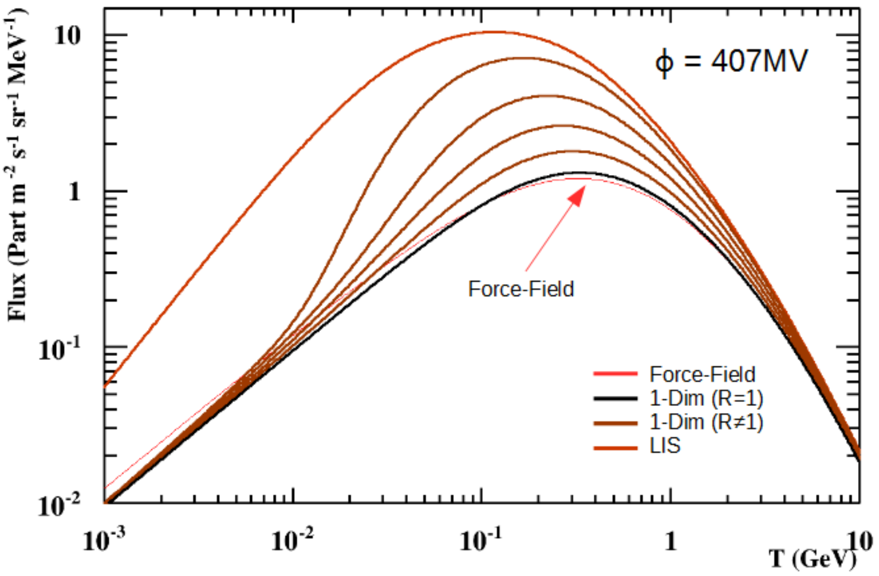

Figure 3.15: Simulation of the Solar modulation of galactic cosmic protons, comparison of 1D solution with force-field solution, the thin dashed red line represents the Force-Field solution while the others are 1D solution at different radii, black line representing the $R = 1$ AU solution and orange representing $R = 90$ AU.

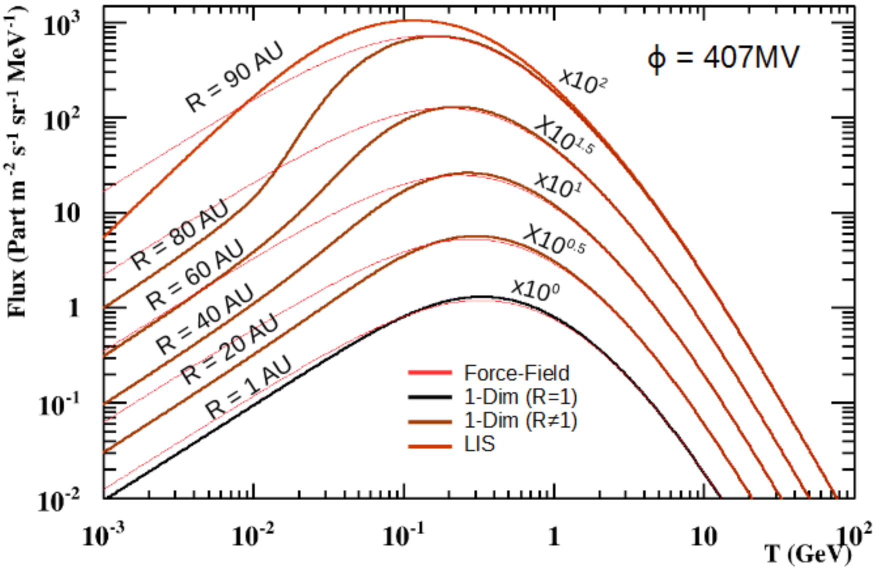

Figure 3.16: Simulation of the Solar modulation of galactic cosmic protons, comparison of 1D solution with force-field solution, scaled, the thin dashed red line represents the Force-Field solution while the others are 1D solution at different radii, black line representing the $R = 1$ AU solution and orange representing $R = 90$ AU.

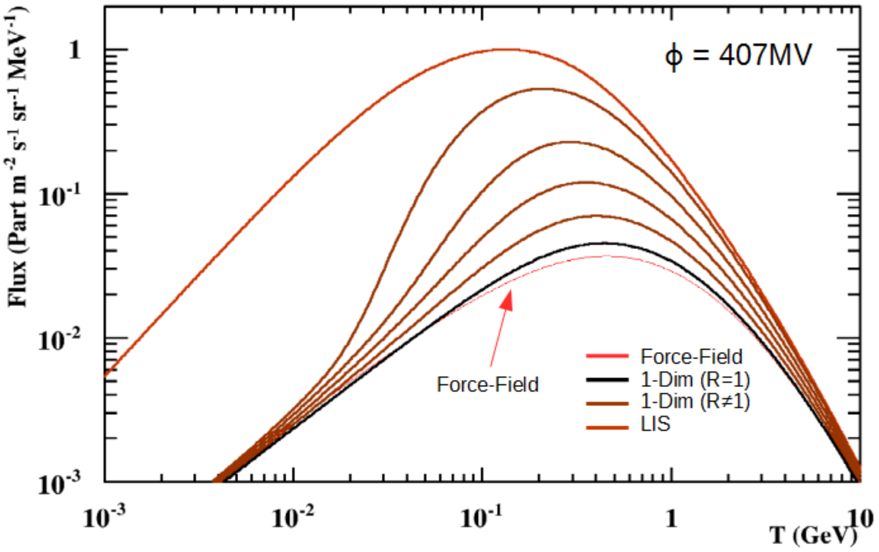

Figure 3.17: Simulation of the Solar modulation of galactic cosmic α particles, comparison of 1D solution with force-field solution, the thin dashed red line represents the Force-Field solution while the others are 1D solution at different radii, black line representing the $R = 1$ AU solution and orange representing $R = 90$ AU.

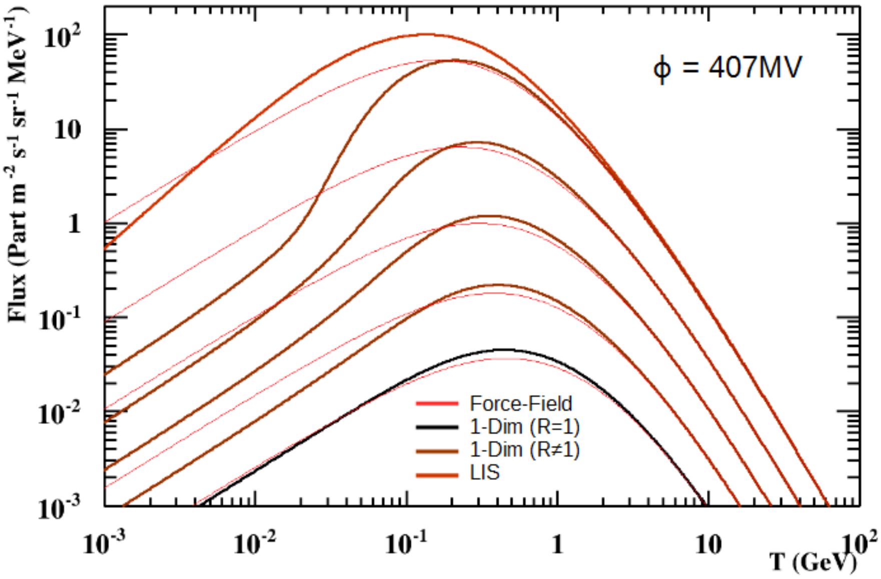

Figure 3.18: Simulation of the Solar modulation of galactic cosmic α particles, comparison of 1D solution with force-field solution, scaled, the thin dashed red line represents the Force-Field solution while the others are 1D solution at different radii, black line representing the $R = 1$ AU solution and orange representing $R = 90$ AU.

As can be seen in the previous figures the Force-Field solution gives out a very close approximation to the 1D resolution of the equation at R = 1AU and for large energies. As the observer moves farther away from the earth, the Force-Field solution starts to deteriorate rapidly for lower energies.

For low rigidities, the solution deviates from the flux very rapidly as distance increases. Figure 3.19 depicts this effect by showing a more detailed simulation where the flux is shown for radii ranging from 89 AU to 89.9 AU.

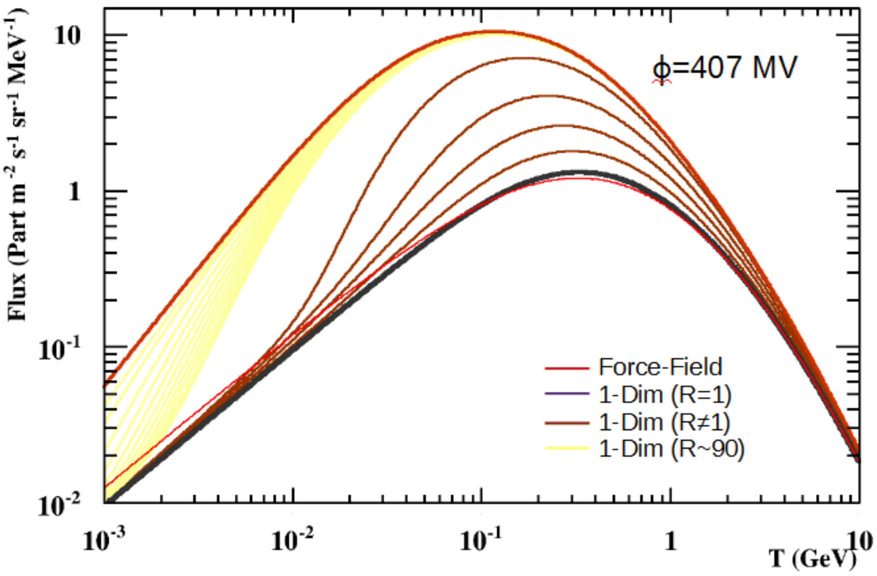

Figure 3.19: Simulation of the Solar modulation of galactic cosmic protons, comparison of 1D solution with force-field solution, the thin red line represents the Force-Field solution while the others are 1D solution at different radii, black line representing the $R = 1$ AU solution and orange representing $R = 90$ AU. In yellow, the solution is detailed for R=89.0,...,89.9.

3.6.2 2D numerical solutions

We now present the results for the numerical simulations for a maximum momentum of 100 GV and a heliosphere of 90 AU of radius, where the function may vary when going from 0 to π as well.

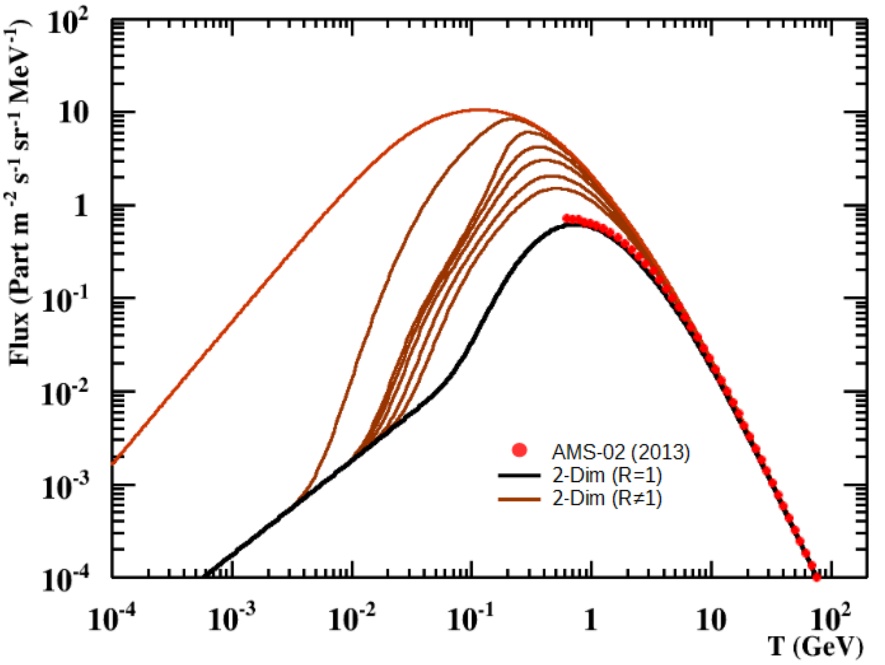

Figure 3.20: Simulation of the Solar modulation of galactic cosmic protons in the 2D solution at different radii. Black line represents flux at Earth, orange line the LIS flux and the red dots are AMS-02 2013 proton flux[61].

As can be seen in figure 3.20, the simulation shows great agreement with the measured flux by AMS-02. The solution diverges a bit from data at the low-end. That might entice a small error in the parameters that go into the simulation. The data points on the plot were not scaled to fit the numerical solution. Other datasets from other experiments are available but they are commonly probes that travel across the Solar system, changing their position with time. This entails that for every data point, a simulation had to be done since it is a snapshot in time.

Even though 2D solution presents a very similar behaviour to the previous for high and low momenta, in the middle range, close to the maximum, it has a structure that is a little different from the other simulations. This is related to the shape of the diffusion coefficient, as was shown by Caballero-Lopez and Moraal [14] and to the HCS drift used. Their two dimensional shape creates a particle drift that is not present in the simpler 1D simulation. The diffusion coefficient is still under study and open for debate by the scientific community as different methods are used to estimate its shape and dependency on basic variables such as velocity, rigidity and the magnetic field itself [46, 54].

The convergence, at higher energy, with the interstellar flux is one of the expected limits for Solar modulation. Solar modulation is a low energy process and should, therefore, have little to no effect on high energy particles, making the flux remain unchanged.

The next step in the study would be the usage of AMS-02 to estimate the cosmic ray flux and, from it, extract the parameters required. These parameters are time dependent and require that the simulation is done for several periods of time and with high enough data. The particle flux is also charge dependent, different species will be modulated differently, thus requiring a very accurate data selection. Unfortunately this was not done due to time constraints.

Even though a flux was not calculated, a framework of detector analysis was established and selection tools were developed in order to be able to do so in the future. This will be the focus of the next chapters.

4

The AMS-02 Experiment

Contents

4.1 Introduction 38
4.2 Sub-detectors 38

4.1 Introduction

The Alpha Magnetic Spectrometer (AMS) (as shown in figure 4.1) is a state-of-the-art particle physics detector mounted on the International Space Station (ISS). It was built, tested and is being operated by an international collaboration of 56 institutions from 16 countries, under the sponsorship of the United States Department of Energy.

It was installed in the ISS by National Aeronautics and Space Administration (NASA) and is designed to operate during the remainder of the station's lifetime.

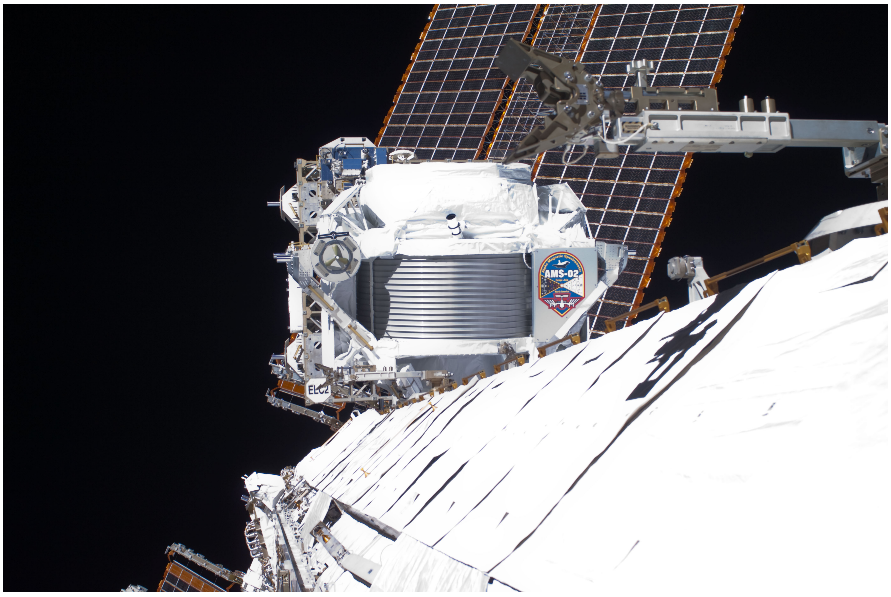

Figure 4.1: Photograph of the AMS-02 detector on the International Space Station.[4]

4.1.1 Brief History

AMS-02 is the second iteration of the Alpha Magnetic Spectrometer proposed by Samuel Ting in 1995. Under Professor Ting's direction, the prototype, AMS-01, was built and made a 2 day flight in orbit in June 1998.

AMS-01 proved that the prototype worked in space and was a fundamental step towards the building of the AMS-02. In addition, it was able to establish an upper limit of 1.1×10^{-6} for the antihelium to helium flux ration [2].

In 16 May of 2011, the Space Shuttle Endeavour carried AMS-02 into space, in the flight STS-134. AMS-02 was installed 3 days later, beginning its data acquisition and, counting over 53 billion events up to September 2014.

4.1.2 Scientific Goals

The AMS experiment has several goals: the detailed measurement of the cosmic ray spectrum, the search for cosmological antimatter and the indirect search for dark matter signals. It is also able to detect γ-rays using its electromagnetic calorimeter and its Silicon Tracker.

4.2 Sub-detectors

The AMS-02 detector is constituted by several sub-detectors and sub-systems (as seen in figure 4.2). As a whole, it's designed to make independent measurements of several physical properties (electric charge, rigidity, velocity and energy) in order to identify the particle species and be able to determine a precise cosmic ray spectrum.

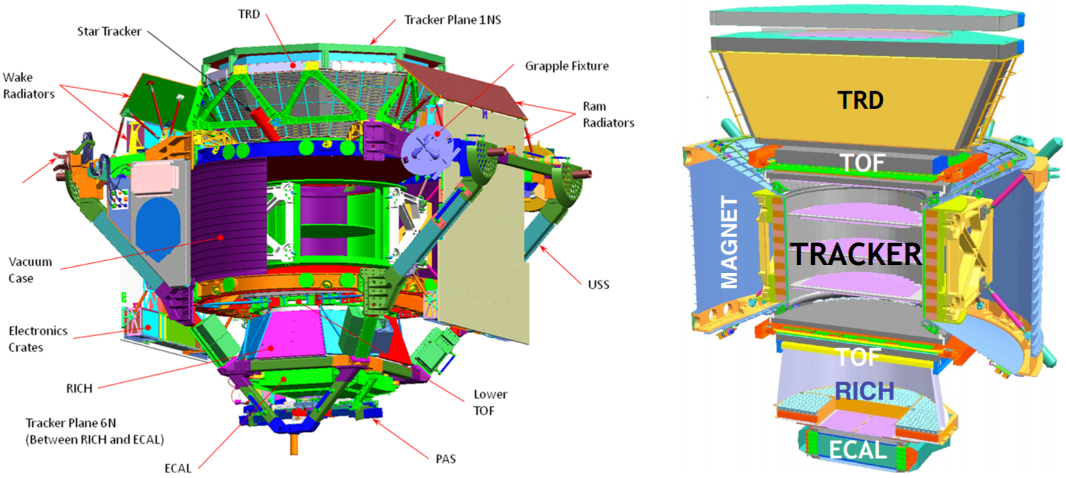
TRD
Tracker Plane 1NS
Star Tracker
Grapple Fixture
Wake Radiators
Ram Radiators
Vacuum Case
USS
Electronics Crates
RICH
Lower TOF
Tracker Plane 6N (Between RICH and ECAL)
PAS
ECAL
TRD
TOF
MAGNET
TRACKER
TOF
RICH
ECAL

(a) Full View **(b)** Detailed View

Figure 4.2: Detailed schematic representation of the AMS-02 detector [4, 64].

4.2.1 Transition Radiation Detector

The Transition Radiation Detector (TRD) is a sub-detector specialized in particle identification. When a charged particle crosses a boundary between two media with different dielectric constants, it emits photons. This radiation is known as transition radiation and is on the X-ray range.

At high energies, photon production is highly dependent on the Lorentz factor, γ. Due to its mass being ~ 1836 times that of an electron, a proton with kinetic energy 1 TeV, would behave like a 0.5 GeV electron in terms of transition radiation. This differentiation is the core of TRD's detection principle.

The TRD is constituted of several of these interfaces together with several straws with a thin wire in the centre and filled with a $\mathrm{Xe}-\mathrm{CO_2}$ mixture which will then ionize as the particle goes through, as shown in figure 4.3. The electron/positron case will have a greater component of X-rays.

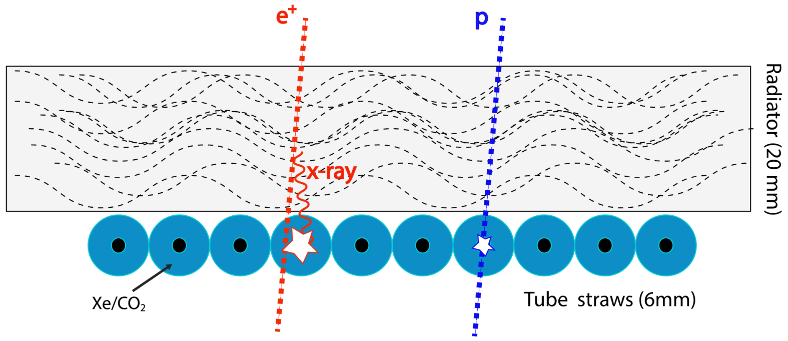
e+
p
x-ray
Radiator (20 mm)
Xe/CO2
Tube straws (6mm)

Figure 4.3: Depiction of one layer of the straw system used in the Transition Radiation Detector in AMS-02[69].

The TRD then makes use of a likelihood function which takes into account the contribution of each tube fired by the particle making the geometric average of the different probabilities estimated from each tube ($\mathcal{L} = \sqrt[n]{\prod_{i=0}^{n} P_i}$). This likelihood estimator is then used to estimate the probability of a particle being of a given mass.

4.2.2 Time-Of-Flight Detector

The Time-of-Flight System (TOF) is a detector designed to measure the times of impact with the different planes and from them estimate particle velocity.

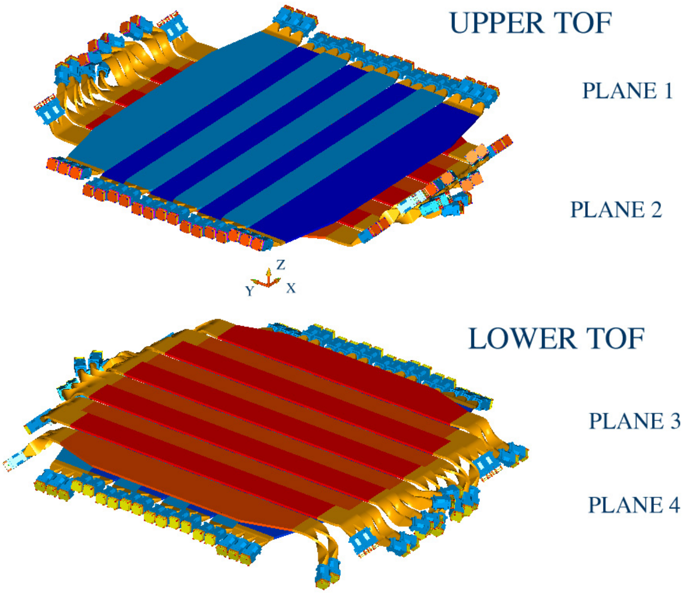

Figure 4.4: Schematic view of the Time-of-Flight detection system[31].

It also plays a fundamental role as a key integrand of the AMS trigger system (particle has to leave a signal in 3 of the 4 planes).

It is composed of 4 planes of scintillation counters, 2 above and 2 below the magnet, containing 8-10 scintillator paddles (8,8,10,8 from top to bottom) with Photomultiplier Tube (PMT)'s on both sides. Each TOF plane consists of paddles aligned along the x and y coordinates, respectively, as depicted in figure 4.4.

4.2.3 Magnet

In the centre of the detector lies a Neodimium-Iron-Boron permanent magnet. This magnet surrounds most of the TRK making possible rigidity measurement. It is fundamental in AMS since it is the only sub-detector to allow for a direct electric charge sign measurement (particles of different electric charge signs bend in different directions).

4.2.4 Silicon Tracker Detector

The Silicon Tracker Detector (TRK) consists of a series of planes made up of 2264 double-sided silicon sensors.

With a position resolution of 10 μm in the bending direction, the TRK is responsible for measuring the particle's rigidity.

By making use of the hits from each plane, the TRK is able to measure rigidity by estimating the curvature in the particle's trajectory inside AMS's permanent magnetic field. It is also possible to extrapolate the particle's trajectory, allowing for a precise estimation of the particle's entry point in the different sub-detectors (RICH depends on this estimation in order to make its own, as will be explained later).

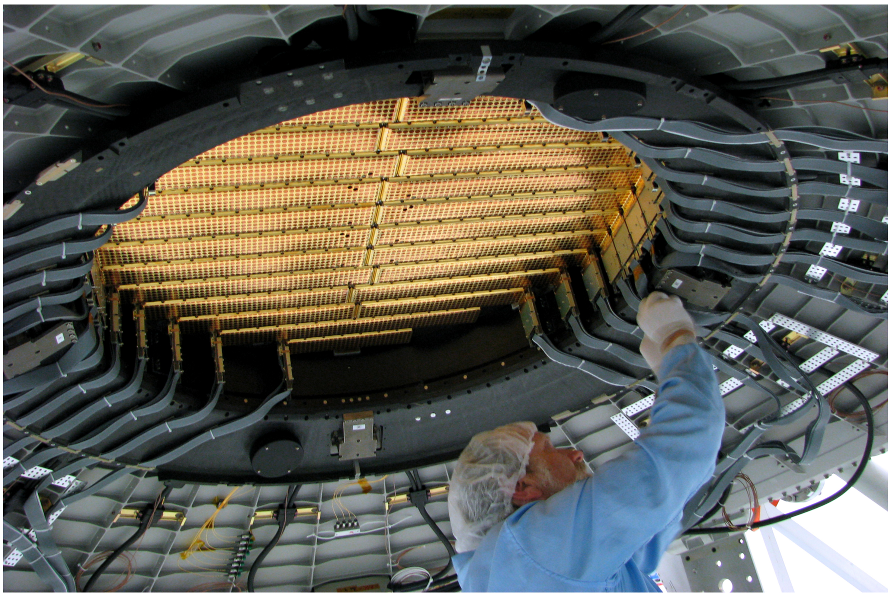

Figure 4.5: Photography of the Silicon Tracker being cabled on AMS-02 magnet.

The TRK is kept aligned by the Tracker Alignment System (TAS). This device is used to periodically keep track of the TRK's mechanical deformations due to temperature changes (ISS has an orbital period of ~ 93 minutes, changing rapidly from daylight to darkness depending on the orbit).

4.2.5 Ring-Imaging Cherenkov Detector

The RICH is a sub-detector of AMS capable of measuring both velocity and charge of the traversing cosmic ray by making use of the Cherenkov radiation phenomenon. It allows for the best velocity measurement of AMS.

A more detailed description will be given in the next chapter.

4.2.6 Electromagnetic Calorimeter

At the bottom of AMS-02 lies Electromagnetic Calorimeter (ECAL). The ECAL consists of a series of 9 super-layers, each with a thickness of 18.5 mm and composed of 11 grooved, 1 mm thick lead foils interleaved with layers of 1 mm diameter scintillating fibbers, glued together with epoxy resin.

The detector's imaging capability is obtained by stacking super-layers with fibres, alternatively parallel to the x-axis (4 layers) and y-axis (5 layers). The detector has an average density of 6.9 $\mathrm{g/cm^3}$ for a total weight of 496 kg.

As the cosmic ray passes through ECAL, it creates a shower of particles whose shape is related to the nature of the primary particle (electromagnetic shower for fermions and hadronic shower for hadrons). ECAL is then able to reconstruct a 3D shower profile at 18 different depths, thus identifying the species and direction of the incident particle. The sum of all layer signals in ECAL is proportional to the particle's deposited energy. It also allows for the AMS γ-ray measurement.

4.2.7 Anti-Coincidence Counter

The Anti-Coincidence Counter is a system built around the inside of AMS's magnet in order to reject particles which would transverse the detector from the side. These particles would interfere with the detection of other particles.

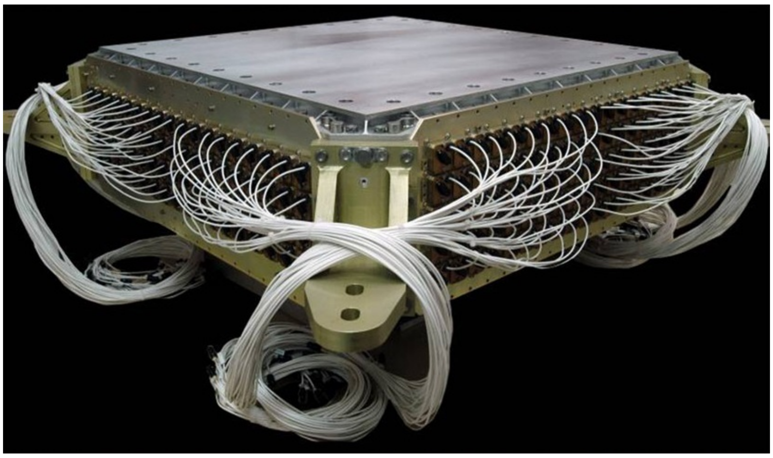

Figure 4.6: Photography of the Electromagnetic Calorimeter [48].

With this brief introduction to the detector's composition and basic functioning, the road is paved towards the detailed study of RICH.

5

RICH Resolution Study

Contents

5.1 The RICH Detector in AMS-02 44
5.2 RICH Resolution Model 50
5.3 Particle Estimator 64

5.1 The RICH Detector in AMS-02

This chapter will be dedicated to the understanding the basic functioning principles behind the RICH detector. It will begin with the estimation of the velocity measurement resolution and end with the development of an estimator of particle species to be used in data selection (namely, proton/electron-positron separation).

The process of selecting particles from a dataset consists of establishing a set of rules and then making the **decision** of whether of not a particle is of a given species. The decision is made by comparing the measurements of the different detectors (keeping in mind their resolutions and uncertainties) against particle properties. Due to the innate imperfection associated with a measurement, every selection rule (commonly known as a selection cut) will have a given efficiency. This efficiency is the estimation of how the rule affects data, how many *good* events are being accepted against all the *good* events present in the dataset. It is then essential to properly understand the detector being used, a bad estimation of a detector resolution may lead to inaccurate selection cuts and, consequently, to a bad estimation of the physical quantity being studied.

As the name would indicate, RICH detection principle is based around Cherenkov radiation.

5.1.1 Cherenkov Radiation

When fast particles traverse a dielectric medium with a velocity greater than the speed of light in that medium, coherent light in a characteristic conical pattern is created. This is known as Cherenkov radiation.

Cherenkov radiation was discovered experimentally in 1934 by P. A. Cherenkov, under the supervision of S. I. Vavilov [15]. This phenomenon was later theoretically interpreted by I. E. Tamm and I. M. Frank [24] which, in 1958, were awarded the Nobel Prize in Physics for the discovery and interpretation of the Cherenkov effect.

As charged particles pass through a dielectric medium they polarize the medium. This polarization stays close to the particle as it moves along the medium and relaxes after a short time, emitting radiation. If the speed of the particle is lower than the speed of light in the medium, $c_n = c/n$, the spherically symmetric wavelets generated around the particle never meet. On the other hand, if the speed of the particle is higher than c_n, the wave-fronts meet, interfere constructively and coherent radiation is generated, as can be seen in figure 5.1.

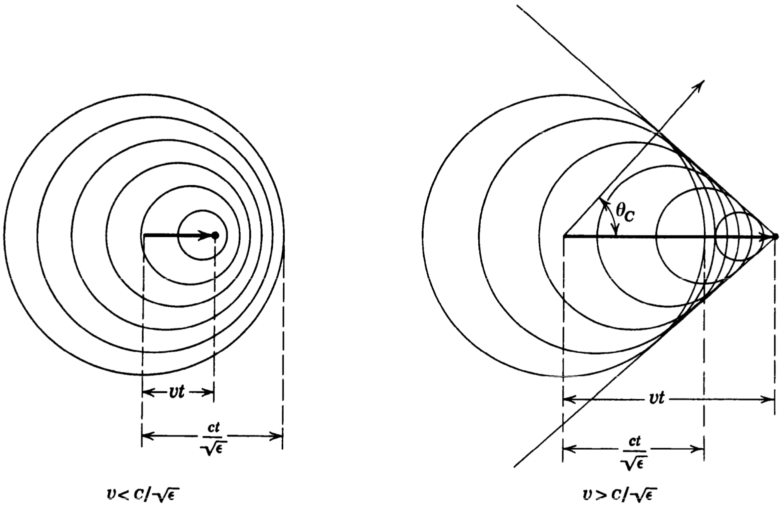

Figure 5.1: Diagram depicting Cherenkov radiation and the process by which it is created [32].

These waves propagate at the speed of c/n from the point from which they were emitted. After a time t passes, all the wave-fronts are in a cone (as can be seen in figure 5.1) around the particle. The direction of propagation of this *shock wave* (exterior normal vector to the conic surface) is the direction angled with θ_C, which can be calculated using trigonometry,

$$\cos\theta_C = \frac{ct/n}{\beta ct} = \frac{1}{\beta n}. \tag{5.1}$$

The Cherenkov angle relates to the velocity via this principle, as shown in figure 5.2.

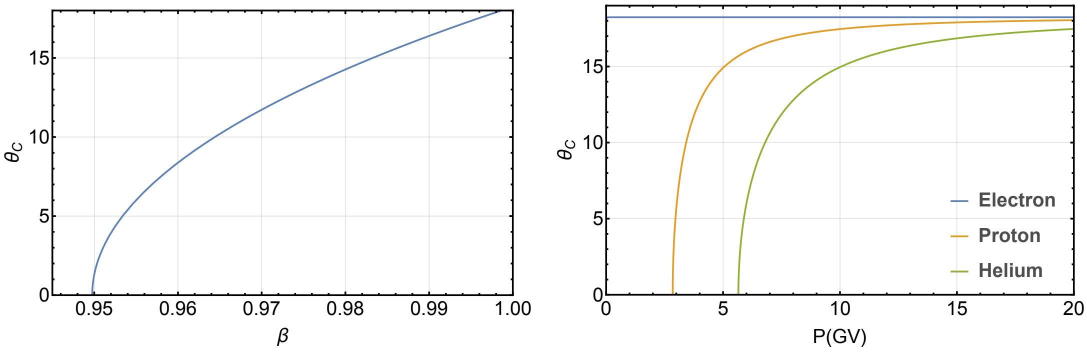

(a) $\theta_C(\beta)$ **(b)** $\theta_C(P)$

Figure 5.2: Cherenkov angle as a function of velocity and rigidity, in Aerogel, for protons.

Frank and Tamm [24] were able to calculate the energy lost as a function of the crossed distance in the material and of photon frequency, ω,

$$\frac{\mathrm{d}^2 E}{\mathrm{d}l\mathrm{d}\omega} = \frac{Z^2\alpha\hbar}{c}\omega\left(1 - \frac{1}{\beta^2 n^2(\omega)}\right), \tag{5.2}$$

which when converted to photons of energy $E_\gamma = \hbar\omega$ becomes,

$$\frac{\mathrm{d}^2 N_\gamma}{\mathrm{d}l\mathrm{d}E_\gamma} = \frac{2\pi Z^2\alpha}{hc}\left(1 - \frac{1}{\beta^2 n^2(\omega)}\right), \tag{5.3}$$

Using this principle, a RICH detector is able to measure the Cherenkov angle and estimate particle velocity from it. It is also possible to determine the charge of the particle by studying the number of measured photoelectrons.

This method of identifying and measuring particles was first proposed by Jacques Séguinot and Tom Ypsilantis in 1977 [62].

As it was seen in chapter 4, AMS-02 contains a RICH detector. This detector will be the main focus of the sections to follow.

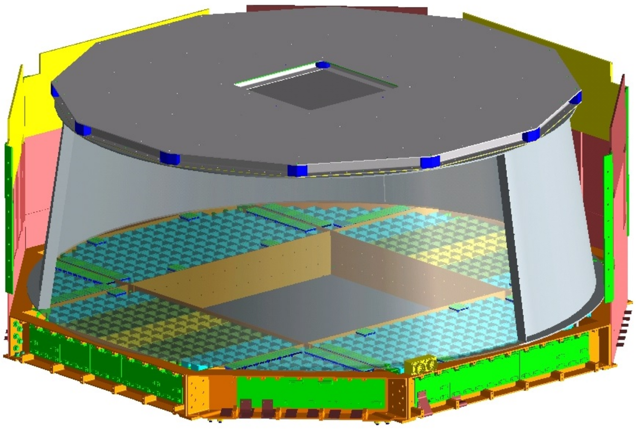

Figure 5.3: Cross-cut view of the RICH detector in AMS-02 [21].

5.1.2 RICH Velocity Measurement

As seen in the previous section, it is possible to estimate the particle's velocity by determining the Cherenkov radiation angle, θ_C.

The RICH detector in AMS-02 consists of a matrix of PMT surrounded by a conic mirror surface, closed off by a dual radiator at the top made of a sodium fluoride central square section ($n = 1.33$ and thickness 0.5 cm), surrounded by Aerogel ($n = 1.05$ and thickness 2.5 cm), as can be seen in figure 5.3. This radiator configuration was chosen to increase ring acceptance since it allows for wider rings near the centre of the detector, where the hole in the PMT matrix due to the ECAL lies.

The detector is built in such a way that fast enough particles that traverse the radiator will create a ring of photoelectrons in the PMT matrix below, which will then serve to estimate the Cherenkov angle. The mirror helps increase ring acceptance by reflecting back onto the matrix any rings that would be too close to the sides to have the full ring inside the detector.

In order to reconstruct the velocity of the particle, the LIP AMS group [20] developed a complex algorithm that takes into account an average emission point in the radiator, the impact point of the cosmic ray in the PMT matrix and the uniformity of the hit distribution in the ring (keeping in mind the deformation of the intersection of the Cherenkov cone with the matrix). Figure 5.4 shows the trajectory of a particle inside the detector and the formation of a Cherenkov ring. The algorithm is based in calculating the probability that a given hit in the matrix belongs to a ring, turning the problem into one of finding the ring that maximizes a likelihood function $L(\theta_C)$,

$$L(\theta_C) = \prod_{i=1}^{N_{pe}} P^{w_i}(r_i(\theta_C)) \tag{5.4}$$

where N_{pe} is the number of hits in the event (except those associated with the impact point of the particle in the matrix), w_i is the hit's weight and r_i is the linear distance of the hit to the ring pattern being tested. Figure 5.5 depicts a reconstruction of a ring.

A very basic way of understanding this reconstruction is that the track extrapolated from the silicon Tracker measurement gives particle direction and impact point in the radiator and the hits give the

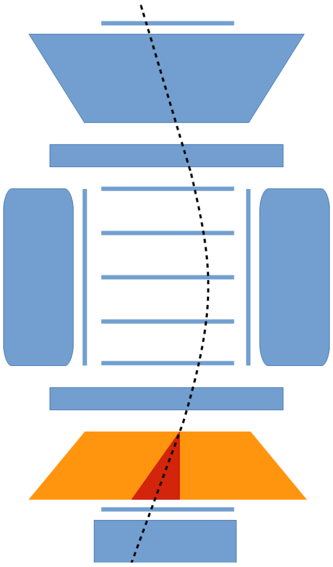

Figure 5.4: Diagram depicting the geometry of the RICH sub-detector in the AMS-02 overall scheme.

cone aperture. In order to do so, it was determined that at least three hits in the PMT matrix were required to be able to measure the Cherenkov angle accurately [20].

5.1.3 Proton Data Analysis

The RICH velocity measurement can be studied by making use of the the large amount of proton data collected by AMS. These protons have to be selected from the complete dataset.

A dataset was created from 2 years of data (2011 to 2013) in order to study RICH performance. The following selection criteria were applied to every event in this dataset.

- **Pre-selection**
  1. Have a level 1 trigger (TOF based)
  2. Have a DAQ event
  3. No Hardware errors
  4. Detector livetime larger than 0.65 for the acquisition second
  5. Particle rigidity larger than the geomagnetic cutoff rigidity
- **General Selection**
  1. Have only one particle track reconstructed coherent with the different sub-detectors (TRK, RICH, TOF,...)
  2. Have only one RICH ring
  3. Have only one TRK track
- **Species Cut**
  1. Particle rigidity > 0
  2. Being selected as a proton by the TRD estimator
  3. Having a charge measured by the silicon Tracker between 0.5 and 1.5

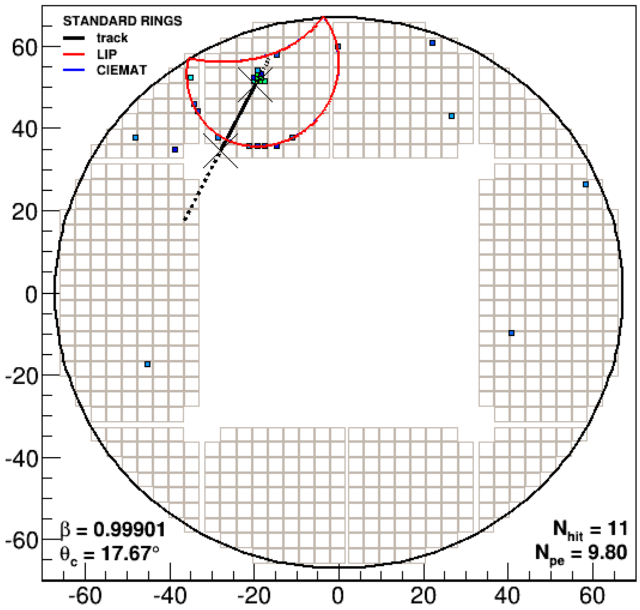

Figure 5.5: Reconstruction of simulated proton in Aerogel in RICH. [20]

- **Tracker Cuts**
  1. Have at least the complete Inner Tracker (planes inside the magnet) to reconstruct rigidity
  2. Track fit reconstruction χ^2 < 10 in the bending direction
- **RICH cuts**
  1. Particle track extrapolation in RICH acceptance
  2. Ring from Aerogel radiator
  3. particle track extrapolation pass within 1 cm of the radiator tile border
  4. Kolmogorov test > 0.1 (hit distribution flatness along the ring)
  5. Ring acceptance higher than 0.4
  6. Number of hits not used in the reconstruction has to be smaller than those used

These cuts were done keeping in mind that they can be applied to both Monte-Carlo and real data. Since the Monte-Carlo used was a pure proton sample, only the **General Selection**, the **Tracker Cuts** and the **RICH Cuts** were applied to it. When being used in the C++ analysis code, the order of the cuts was optimized for the analysis, the existence of a RICH ring was demanded before anything else.

The AMS data production used on both Monte-Carlo and ISS data was B800 and the results are presented in figures 5.6 and 5.7.

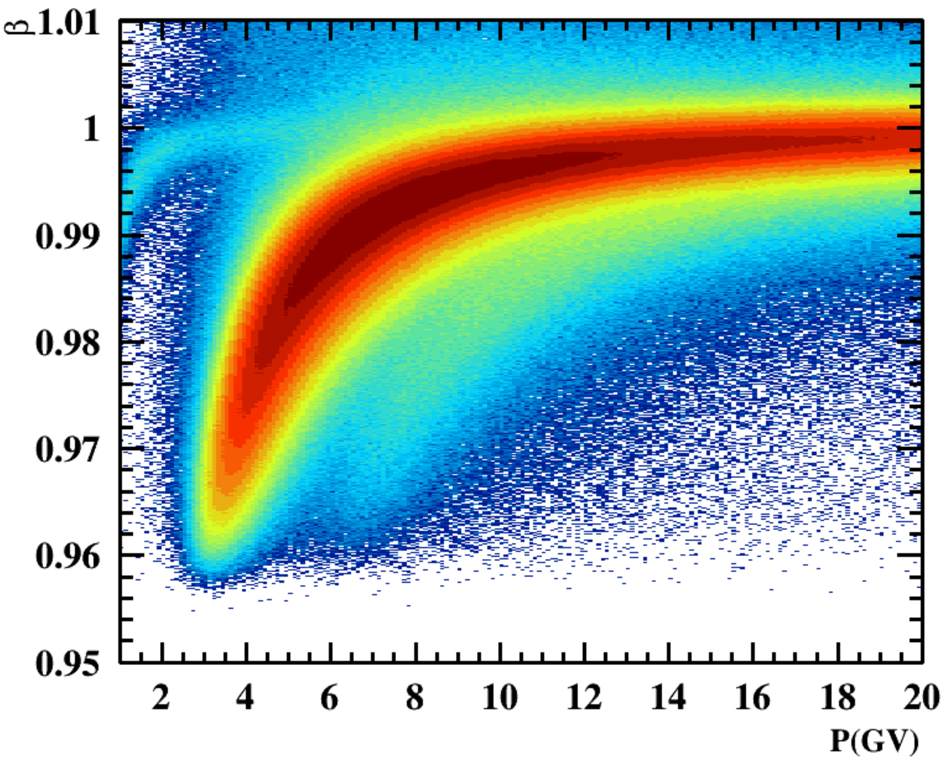

Figure 5.6: RICH velocity measurement for Aerogel, as a function of rigidity, for a real data proton sample.

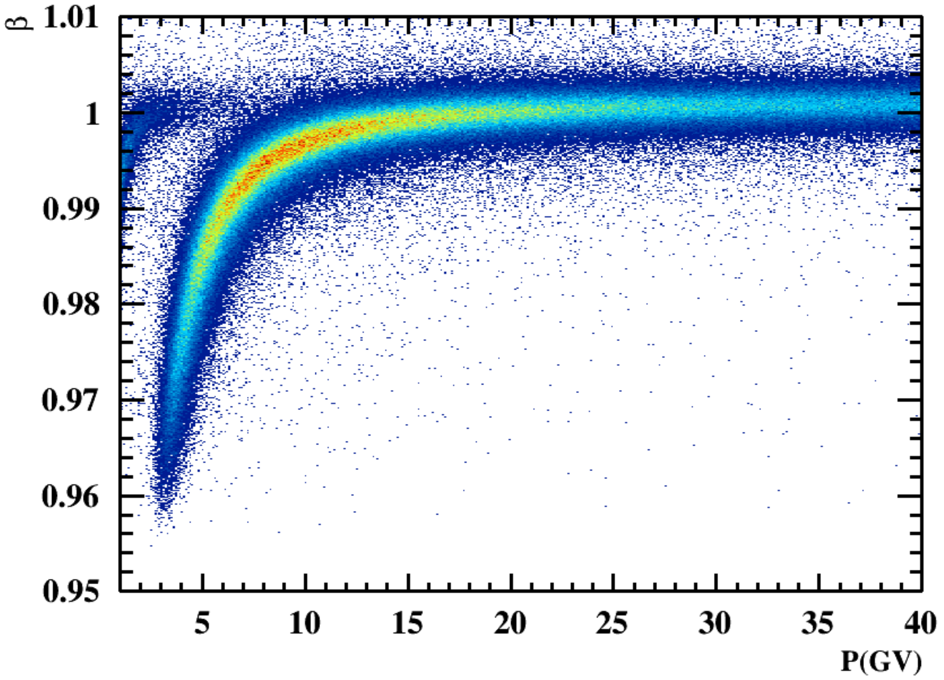

Figure 5.7: RICH velocity measurement for Aerogel, as a function of rigidity, for a Monte-Carlo proton sample.

Looking at figures 5.6 and 5.7, we can see that the main curve is the proton curve while the signal to the left (remembering that protons in Aerogel only starts radiating at $\sim 2.5\,\mathrm{GV}$) are secondary particles that are created when the primary passes through the detector. A mass cut could be used here (in this case, a mass cut would constitute of choosing only particles in a certain band around the proton curve, for example $P{\pm}0.5P \wedge \beta{\pm}0.01\beta$). It was chosen to not do cut the secondaries off with a mass cut for two reasons: they constitute a very small part of the data (they are very localized to small momenta and to velocities very close to unity) and cutting them off might adulterate the resolution.

Now that it is known how many particles pass the selection, how these are measured will be the next subject in focus.

5.2 RICH Resolution Model

As shown in the previous section, proton data will be organized in bins of momentum and velocity $(\mathrm{d}p, \mathrm{d}\beta)$.To each slice in momentum, the velocity distribution was fitted according to a normal distribution. The width of fitted the distribution is shown in 5.8.

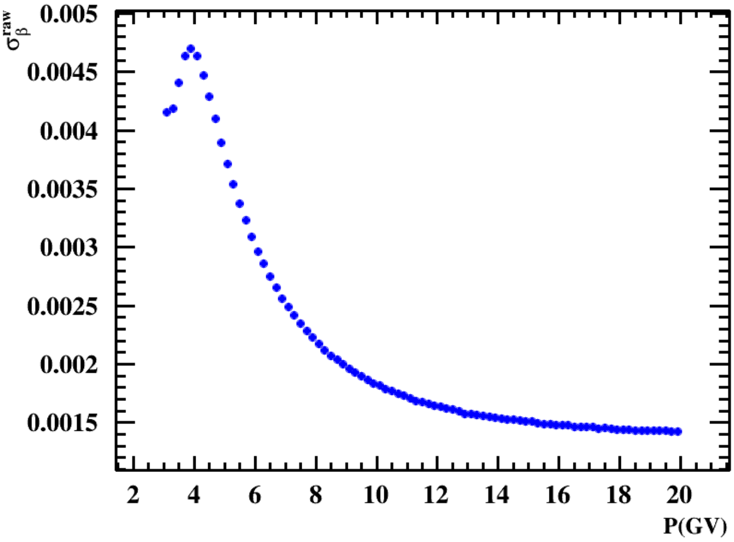

Figure 5.8: Velocity distribution width using a Gaussian fit function, applied to AMS-02 data.

This velocity resolution does not reflect the RICH velocity resolution, it includes both the velocity resolution and the spread caused by the contribution of particles from rigidities outside the momentum bin considered.

The arbitrary choice of a bin $[p_1, p_2]$ does not mean that every particle within it had their true momentum lie between p_1 and p_2. Taking into account the spread of momentum measurement, the particle's true momentum lies in a bin with the width given by

$$\Delta p_0 \sim (p_2 - p_1) + 6\sigma_p. \tag{5.5}$$

This expression means that the measured resolution is a function of both momentum and velocity resolution and that the following relation can be written,

$$\left(\frac{\sigma_\beta}{\beta}\right) = \left(\frac{\sigma_\beta}{\beta}\right)_p \oplus \left(\frac{\sigma_\beta}{\beta}\right)_{\mathrm{RICH}} = \frac{1}{(p_0/m)^2 + 1}\left(\frac{\sigma_{p_0}}{p_0}\right)_p \oplus \left(\frac{\sigma_\beta}{\beta}\right)_{\mathrm{RICH}}. \tag{5.6}$$

To estimate RICH resolution from this dataset, a likelihood function was built, $\mathcal{L}(\beta)$. This function is used to calculate the probability, $P = \mathcal{L}(\beta)\mathrm{d}\beta$, that a given velocity measurement β, comes from a particle whose measured momentum lies with the momentum bin, $[p_1, p_2]$. It takes into account that a particle with a measured momentum lying in the interval $[p_1, p_2]$ has its true momentum belong to a larger range, $p_1 - 3\sigma_p < p_0 < p_2 + 3\sigma_p$, as shown previously.

Defining $L(p_0)$ as the probability of having a particle of momentum p_0 belong to the interval $[p_1, p_2]$, defining $g(\beta, \beta_0)$ as the probability that a true velocity β_0 is measured as a velocity β and integrating over true momentum p_0, one can write the likelihood function $\mathcal{L}(\beta)$ as

$$\mathcal{L}(\beta, \sigma_\beta, \sigma_p) = A \int_{p_1-3\sigma_p}^{p_2+3\sigma_p} \mathrm{d}p_0 \Phi(p_0) L(p_0, \sigma_p) g[\beta, \beta_0(p_0, m), \sigma_\beta]. \tag{5.7}$$

Assuming velocity measurement is given by a normal distribution, one can write

$$g[\beta, \beta_0(p_0, m), \sigma_\beta] = \frac{1}{\sqrt{2\pi}\sigma_\beta} \exp\left[-\frac{1}{2}\left(\frac{\beta-\beta_0}{\sigma_\beta}\right)^2\right]. \tag{5.8}$$

The two missing elements come from the parametrization of the smearing in rigidity measurement ($L(p_0)$) and the estimation of the primary flux.

5.2.1 Tracker Resolution Study

In order to calculate $L(p_0)$, one must first understand how momentum is measured and with what uncertainty. As it was seen previously, the sub-detector responsible for the rigidity measurement is the Tracker. The process of reconstructing the particle's rigidity is based on estimating the sagitta of the trajectory, a value proportional to $1/R$, where R is the curvature radius of the trajectory inside the magnetic field, as depicted in figure 5.9. From electromagnetism it is known that, $R = mv_\perp/(|q|B) = P/B$, where P is the particle's rigidity, given by $P = p/q$. From this it can be deduced that the sampled variable is proportional to the inverse of rigidity, $1/P$, henceforth known as X. Additionally, it is convenient to start working in rigidity instead of momentum. This will not constitute a great change in the expressions but since it is the natural variable in this particular problem, it will be the used variable.

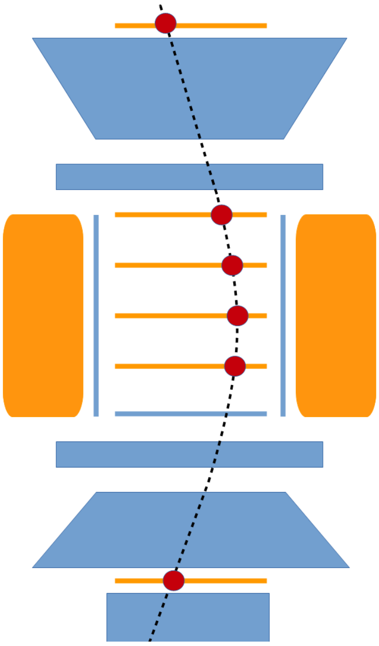

Figure 5.9: Diagram depicting particle interaction with the Tracker detector and track extrapolation.

One can now calculate how relative error in rigidity relates to the relative error in inverse rigidity by doing

$$X = \frac{1}{P} \implies \mathrm{d}X = \left|\frac{-1}{P^2}\right| \mathrm{d}P \implies \mathrm{d}X = \left|\frac{-X}{P}\right| \mathrm{d}P \implies \frac{\mathrm{d}X}{X} = \frac{\mathrm{d}P}{P}. \tag{5.9}$$

Since relative errors are the same one can study the relative resolution of inverse rigidity and use it the same way relative rigidity resolution would be. The likelihood function $L(P_0)$ can now be calculated and inserted into expression 5.7

$$\begin{aligned} L(P_0,\sigma_p) &= \int_{P_1}^{P_2} f_P(P,P_0)\,\mathrm{d}P = \int_{X_1}^{X_2} f_X(X,X_0)\,\mathrm{d}X = \int_{X_1}^{X_2} \frac{1}{\sqrt{2\pi}\sigma_X(P_0)} \exp\left[-\frac{1}{2}\left(\frac{X-X_0}{\sigma_X}\right)^2\right]\mathrm{d}X \\ &= 0.5\left[\mathrm{Erf}\left(\frac{X_2-X_0}{\sqrt{2}\sigma_X}\right) - \mathrm{Erf}\left(\frac{X_1-X_0}{\sqrt{2}\sigma_X}\right)\right]. \end{aligned} \tag{5.10}$$

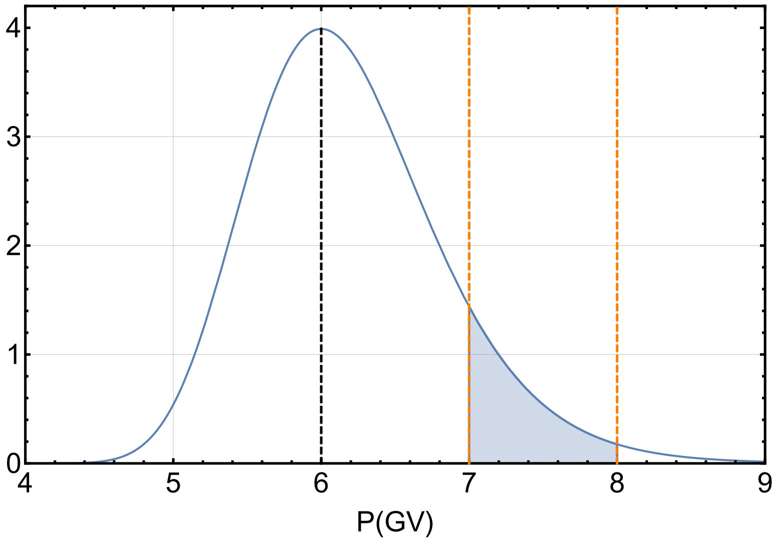

Figure 5.10: Plot highlighting the smearing effect of rigidity measurement by showing the contribution of a 6 GV cosmic ray to the bin 7-8.

The way $L(P_0)$ estimates the probability that a cosmic ray's measured rigidity lies in a given bin is shown in figure 5.10. For a cosmic ray of true momentum of 6 GV, the value of $L(P_0)$ is calculated by integrating the rigidity distribution function over the interval $[7, 8]$ GV. This smearing effect will produce a range of true rigidities larger than the interval in question, as is depicted figure 5.11 where $L(P_0)$ is plotted as a function of true rigidity, for a resolution of 11$\%$.

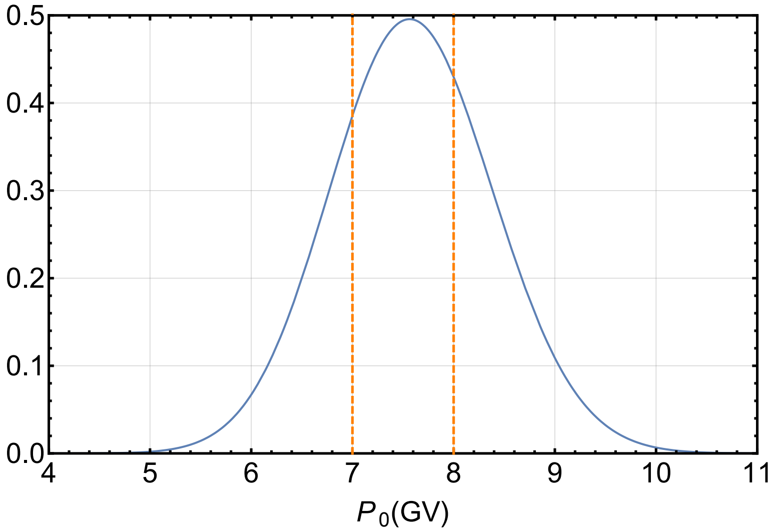

Figure 5.11: Plot showing the contribution of every rigidity to the bin 7-8 GV.

In order to estimate rigidity migration, one can make use of the AMS-02 Monte Carlo simulation but, in order to do that, a new variable has to be defined, $t_X = \frac{X-X_0}{X_0}$. It can be shown that $\langle t_X \rangle = \langle X \rangle - X_0$ and that $\mathrm{var}(t_X) = \mathrm{var}(X)/X_0^2$. It is then easy to show that if X is Normally distributed t_X will also be normally distributed (which data will also show that it is). This implies $\sigma_{t_X} = \sigma_X/X_0$.

Using the proton sample from the official AMS Monte Carlo simulation of the detector, it is possible to estimate relative rigidity measurement resolution from t_X's resolution (shown in figure 5.12) by fitting a normal distribution to slices of figure 5.12.

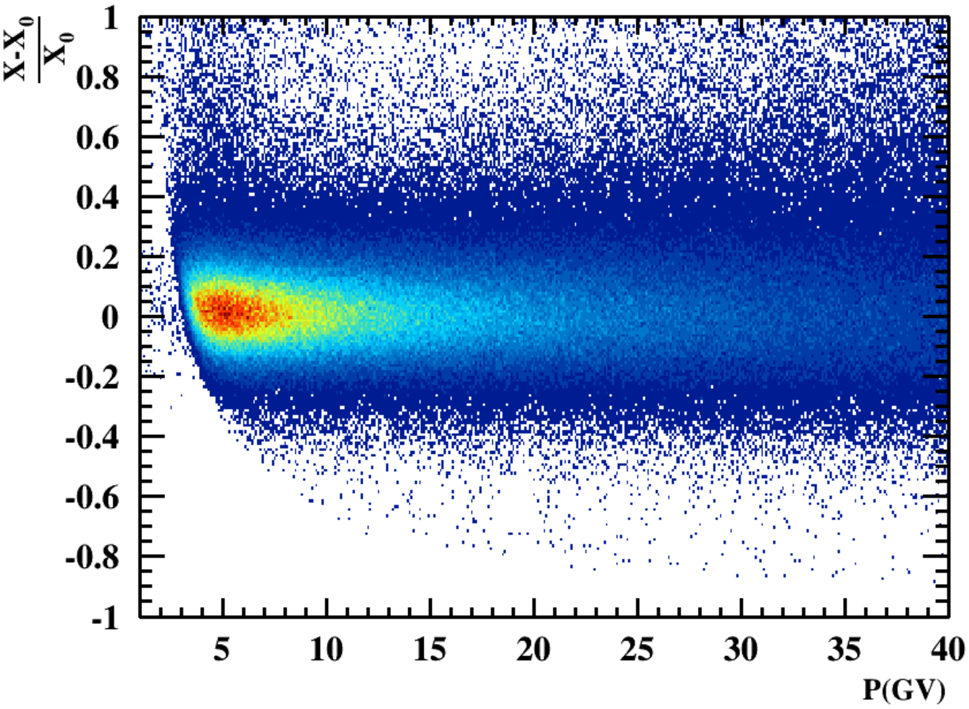

Figure 5.12: Inverse rigidity relative shift as a function of rigidity, for a MC proton sample.

With the purpose of verifying rigidity resolution dependency with inverse resolution, two different distributions were used to fit to this dataset, the first was a double Gaussian with two different averages and two different standard deviations, while the second was a single Gaussian. Figure 5.13 shows the comparison between the results for resolutions in the main Gaussian of both models. These were applied to the Monte Carlo sample.

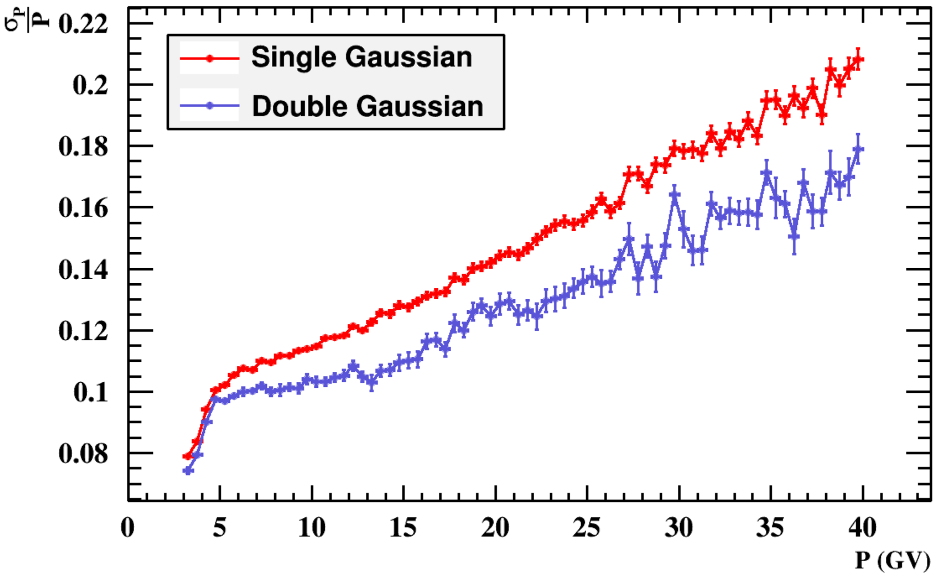

Figure 5.13: Comparison between the sigma of one Gaussian model versus the sigma of the main Gaussian in the two Gaussian model, as fitting functions.

For clarity, a slice in rigidity, from 6.5 to 7 GV, was taken from the histogram in figure 5.12 and displayed in figure 5.14.

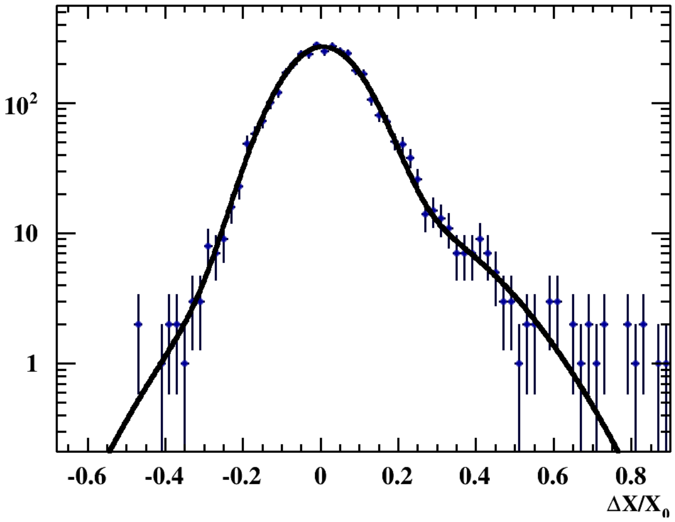

Figure 5.14: Inverse rigidity relative shift fit to slice 6.5-7 GV.

As can be seen in 5.15, the weight of the second Gaussian is very small. Due to this fact, it was decided to only use the single Gaussian distribution during the following studies.

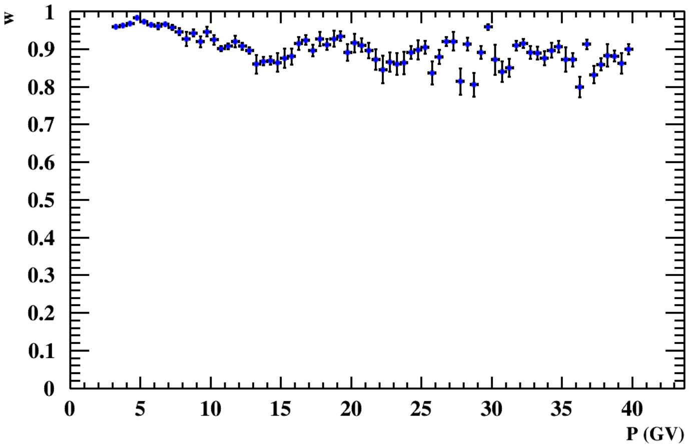

Figure 5.15: Relative weight between the two Normal distributions fitted to rigidity resolution.

For completeness sake, figure 5.16 shows the standard deviation for the second Gaussian in the two Gaussian model.

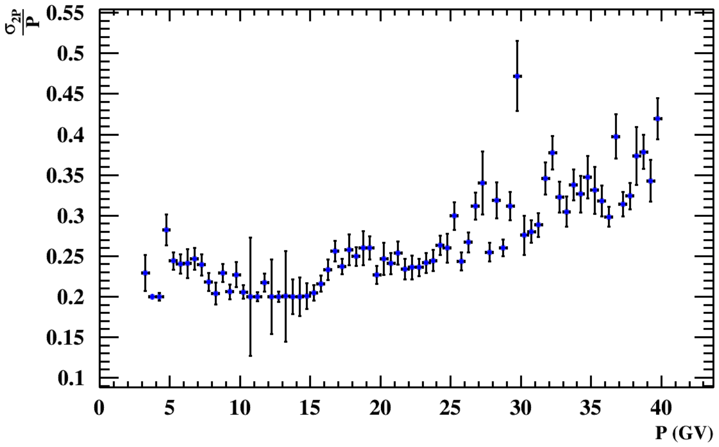

Figure 5.16: σ_P/P for the second gaussian in the two gaussian model for the rigidity resolution, as a function of particle rigidity.

5.2.2 Primary Cosmic Ray Flux

The next and final step towards the complete elaboration of the RICH resolution model is the comprehension of the term $\Phi(P_0)$ from the likelihood function in expression 5.7, the flux of primaries that generates the dataset being studied.

5.2.2.A Local Interstellar Spectrum

One can start with the primary cosmic ray flux. This is the number of particles (in this case protons) reaching the Solar system per unit of time, per interval of rigidity, per unit of transverse area and per unit of angular aperture,

$$\frac{\mathrm{d}N_0}{\mathrm{d}T\mathrm{d}A\mathrm{d}\Omega\mathrm{d}s}(T) = \frac{\mathrm{d}N}{\mathrm{d}T} = \frac{18.9T^{-2.79}}{1 + 6.75T^{-1.22} + 1.30T^{-2.8} + 0.0087T^{-4.20}}. \tag{5.11}$$

This is the same flux as used on chapter 3, but on different units (more appropriate for this study), and is depicted in figure 5.17.

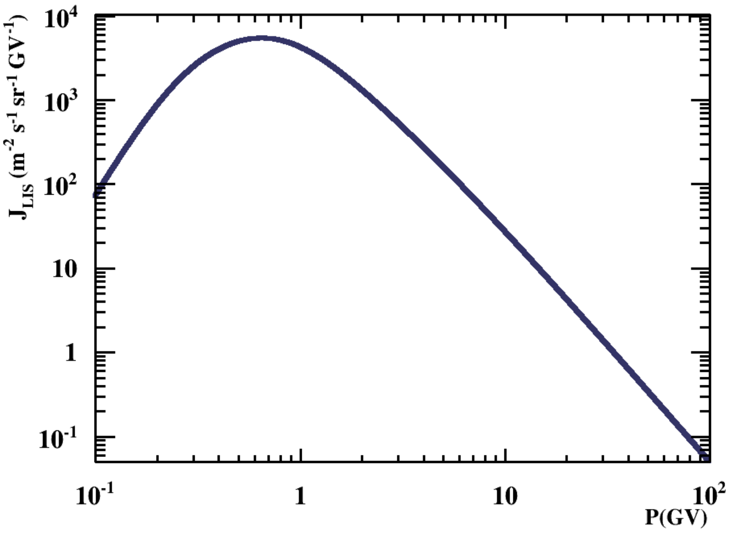

Figure 5.17: Local interstellar primary proton flux[68].

5.2.2.B Solar Modulation

If there were no other effects, the previous flux would have been enough, but this is not the case, there are three elements that must also be taken into consideration, the first being Solar modulation. As it was shown previously, low energy cosmic rays ($P < 40$ GV) have their energy shifted when they cross the heliosphere. To take this effect into consideration the simplest model was used (in order to improve computational performance), the Force-Field model, which takes the form

$$J_T(1AU, E) = J_{\mathrm{LIS}}(E + \Phi_{SM}) \frac{E^2 - m^2}{(E + \Phi_{SM})^2 - m^2}, \tag{5.12}$$

as seen previously, and is depicted in figure 5.18.

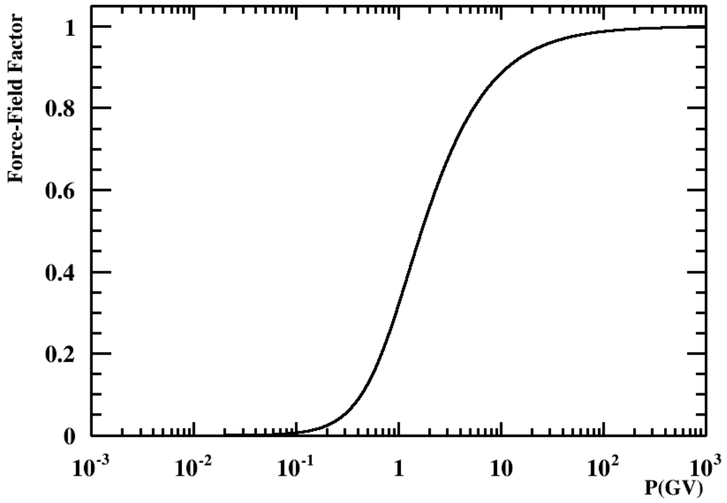

Figure 5.18: Solar modulation Force-Field factor by which the flux is multiplied.

5.2.2.C Geomagnetic Cutoff

The second phenomenon to take into account is the geomagnetic rigidity cutoff. As mentioned in section 3.3.1 the Earth's magnetic field will trap particles with momentum lower than the cutoff value.

In order to estimate the probability that a particle with a given rigidity surpasses Earth's magnetic field, an histogram was made. For any given position of the ISS, the cutoff rigidity was estimated and to every bin *after* the cutoff, one count was added to it. This means that at one particular time, only particles with a larger rigidity than the cutoff would be detectable by AMS.

Filling the histogram with a large number of ISS orbits (3 months) and normalizing it so that when $P_0 \to +\infty$, $P_{\text{cutoff}}(P_0) = 1$, it then becomes the probability that a particle with a given rigidity is detectable by AMS-02. The result can be seen on figure 5.19.

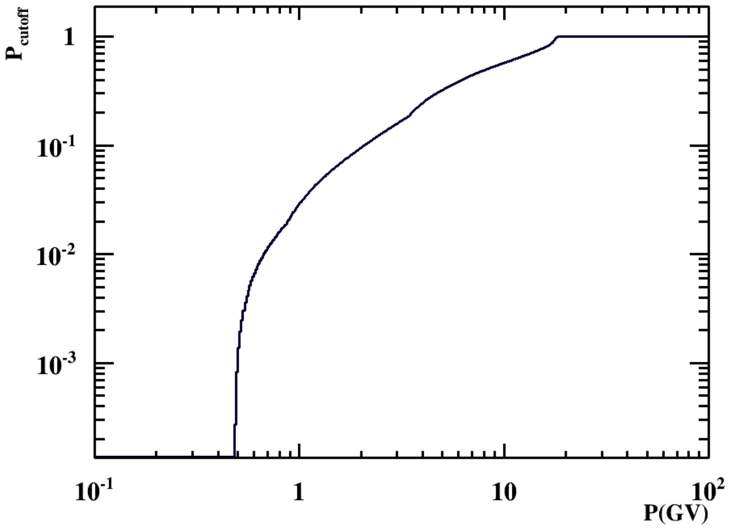

Figure 5.19: Probability that a particle of rigidity P is able to reach ISS, through the Earth's magnetic field, averaged out over 3 months.

the parametrization of this effect is essential if the objective is the study of low energy Galactic cosmic rays. If particles with rigidity lower than the cutoff rigidity are detected, those particles had to be trapped in Earth's magnetic field, making their origins uncertain.

5.2.2.D Ring Probability

The third and final requirement is no longer related to the physics of the cosmic rays but rather to the detector in study, the RICH detector. As it was explained previously, in order to determine the aperture angle of the Cherenkov ring, at least three hits in the matrix are required. This geometric constraint can be parametrized by a function which gives the probability of having a RICH ring formed for a given rigidity. In previous studies made by the LIP AMS-02 group [20], the average number of photons emitted was estimated and parametrized as a function of particle's rigidity, as shown in figure 5.20.

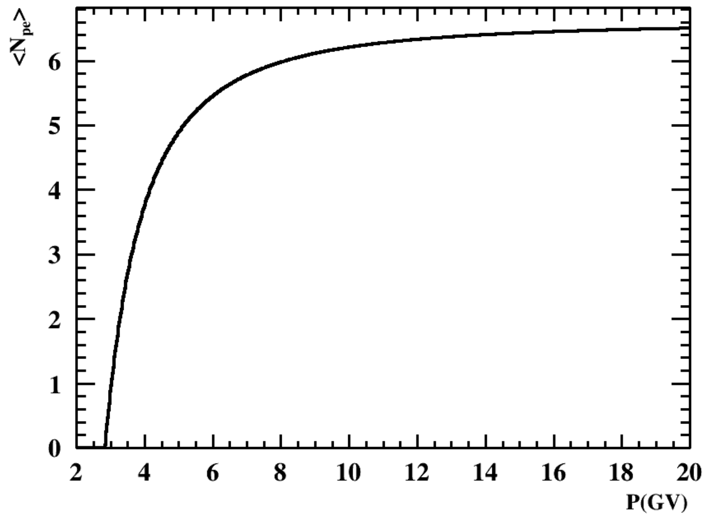

Figure 5.20: Mean number of radiated photoelectrons for Aerogel radiator for vertical protons, as a function of rigidity, in AMS-02.

Using this parametrization, it is possible to determine the probability that a particle with a given rigidity has a well enough defined ring that it can be accurately measured (at least 3 hits).

Considering that the number of hits is approximately given by a Poisson distribution function with a mean of $N_{pe}(P_0)$ ($N_{\text{hits}} \sim \text{Poisson}(\mu = Npe(P_0))$), the three hits requirement becomes $P(N_{pe} >= 3)$ which is the same as having $1 - P(N_{pe} < 3)$. This probability can be calculated by doing

$$P_{\text{ring}}(P_0) = \sum_{i=0}^{2} \frac{\mu^i}{i!} e^{-\mu} = 1 - (1 + \mu + 0.5\mu^2)e^{-\mu}, \ \mu = N_{pe}(P_0). \tag{5.13}$$

Figure 5.21 shows the result of the estimated ring probability in the Aerogel radiator for protons, as a function of particle rigidity.

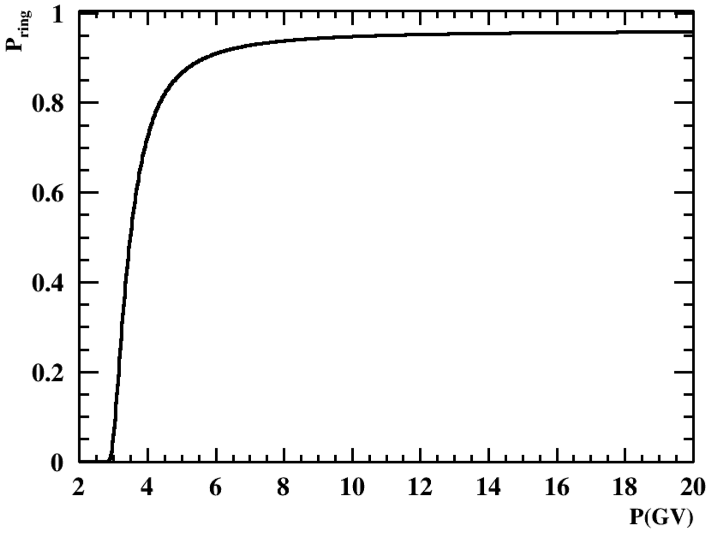

Figure 5.21: Cherenkov ring probability for AGL, as a function of rigidity, in AMS-02, for protons.

Careful observation of the ring probability function will show that the probability starts differing from 0 near the 3 GV rigidity instead of the ~ 2.84719 GV for a proton in Aerogel ($n = 1.0529$). This is due to another imposition made by the reconstruction algorithm. As the cosmic ray passes through the detector, it also passes through the matrix, leaving a signal in the PMT's in the matrix that does not come from the Cherenkov cone of light. To prevent mistaking the signal ring from this central gathering of this, an association distance larger than 5 cm is required by the algorithm. Since the detector is 48 cm, this distance imposes then a new radiation threshold of ~ 3.0173 GV.

5.2.3 The Full Model

All the necessary elements are now well understood and the model can be applied to both Monte Carlo and AMS-02 data. The fully parametrized model can be written as

$$\begin{aligned}\mathcal{L}(\beta,\sigma_\beta,\sigma_X) &= A\int_{p_1-3\sigma_X}^{p_2+3\sigma_X} \mathrm{d}P_0\Phi(P_0)L(P_0,\sigma_X)g[\beta,\beta_0(P_0,m),\sigma_\beta] \\ &= A\int_{p_1-3\sigma_X}^{p_2+3\sigma_X} \mathrm{d}P_0\frac{\mathrm{d}N_0}{\mathrm{d}P_0}(P_0)\,P_{\mathrm{ring}}(P_0)\,P_{\mathrm{cutoff}}(P_0)SM(P_0) \\ &\qquad 0.5\left[\mathrm{Erf}\left(\frac{X_2-X_0}{\sqrt{2}\sigma_X(P_0)}\right)-\mathrm{Erf}\left(\frac{X_1-X_0}{\sqrt{2}\sigma_X(P_0)}\right)\right] \\ &\qquad \frac{1}{\sqrt{2\pi}\sigma_\beta(P_0)}\exp\left[-\frac{1}{2}\left(\frac{\beta-\beta_0}{\sigma_\beta(P_0)}\right)^2\right].\end{aligned} \tag{5.14}$$

The full likelihood function, calculated for several rigidity bins, can be seen in 5.22.

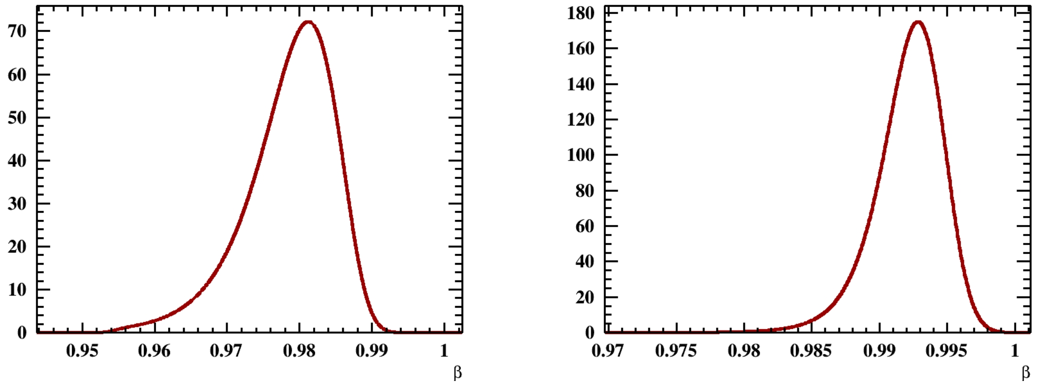

(a) 4 - 5 GV

(b) 7 - 8 GV

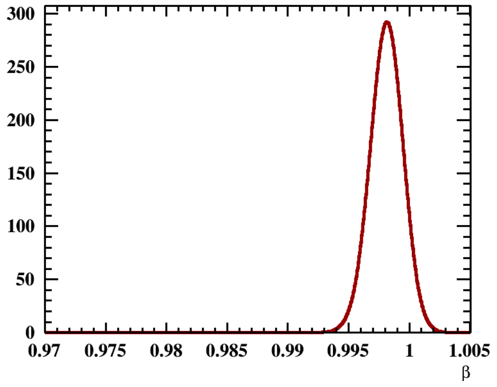

(c) 15 - 16 GV

Figure 5.22: Probability density function of velocity, under the full model, for different rigidity bins.

This study has the goal of estimating RICH velocity resolution as a function of rigidity and, in doing so, it will also estimate TRK resolution from data. This revealed to be a cumbersome task due to the number of parameters and the models used to describe the individual detectors. This function was evaluated numerically (numerical integration with Gauss-Legendre quadrature rule).

To recover both rigidity and velocity resolutions, the likelihood function from expression 5.14 must be used as a fit function to rigidity slices of 5.7. Since both rigidity and velocity resolutions are functions of the particle's true rigidity, when data gets organized in bins, the smearing effect mentioned in section 5.2 gains importance once more. The only way to be able to use expression 5.14 as a fit function is to assume that the resolutions in the model are constants within the bin chosen. This means that the estimated values are not a function of true rigidity explicitly but rather an average of that variable over the bin. This is a necessary approximation due to the statistical nature of the problem but this is not uncommon to do and the error is not high so long as the bins are chosen to be narrow enough.

Now that the model is fully defined and all the inherent approximations and models are characterized, the likelihood function can be applied to data.

5.2.4 Results from Fit to Monte Carlo Data

The model was firstly applied to Monte Carlo data and the results are shown in figures 5.23.

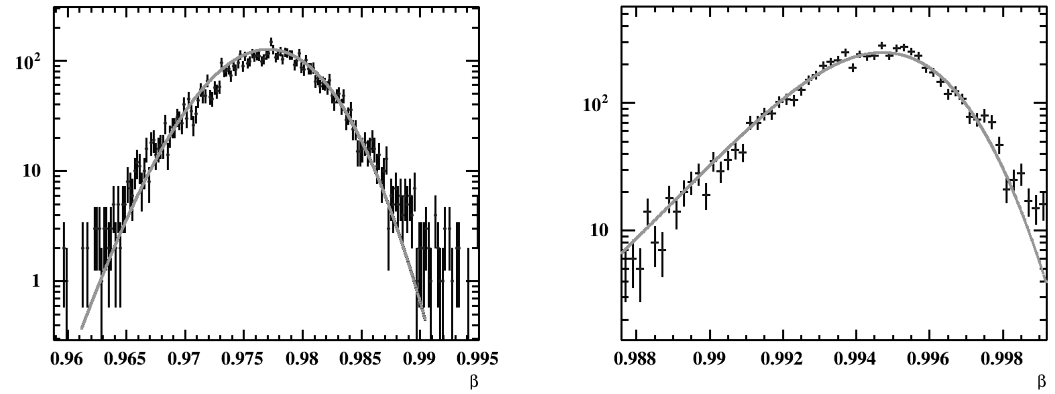

(a) 4 - 4.2 GV

(b) 8 - 8.2 GV

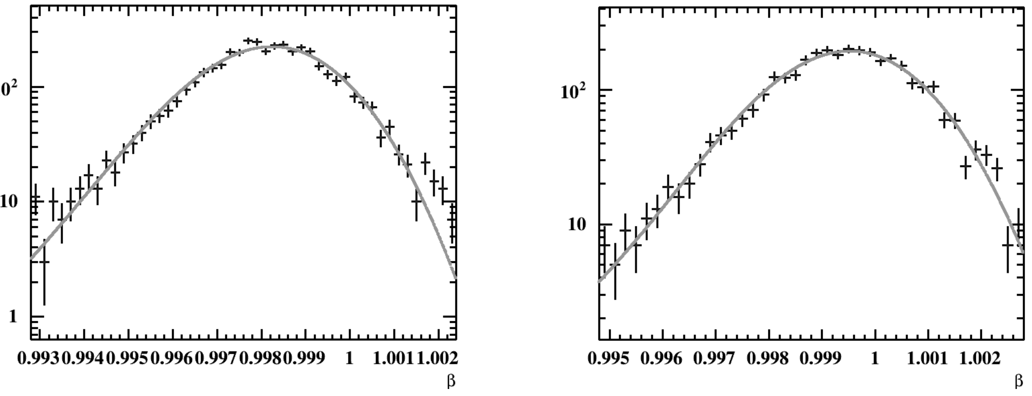

(c) 12 - 12.2 GV

(d) 16 - 16.2 GV

Figure 5.23: Plot of the model fitted to Monte Carlo data, for several rigidity intervals.

Gathering the results from the fits made throughout all the rigidity range, divided into bins of 0.2 GV width, yielded figures 5.25 and 5.24.

The fit function shows good agreement with the MC data sample.

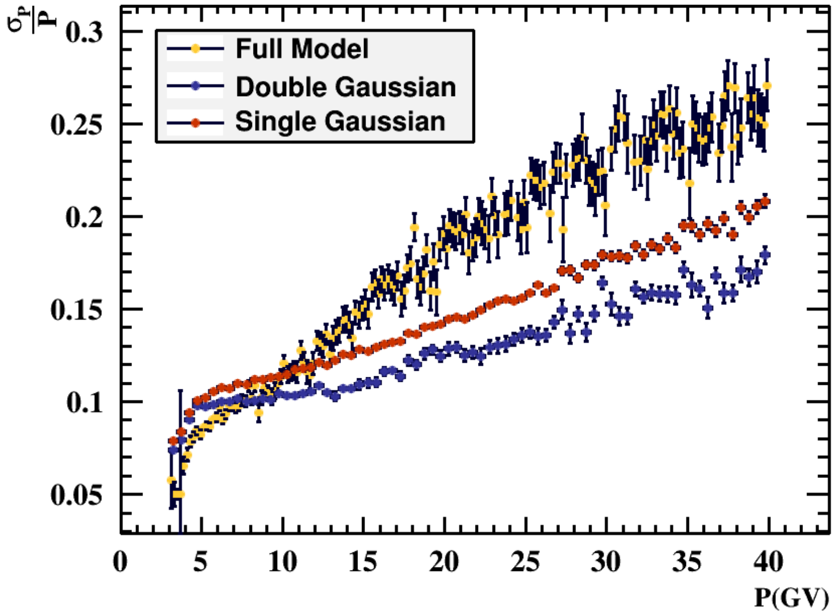

Figure 5.24: Comparison of rigidity resolution between the full model fit, the single Gaussian fit to relative shift and the double Gaussian fit to relative shift in rigidity (displaying only main Gaussian in the double Gaussian case), applied to a Monte Carlo proton sample.

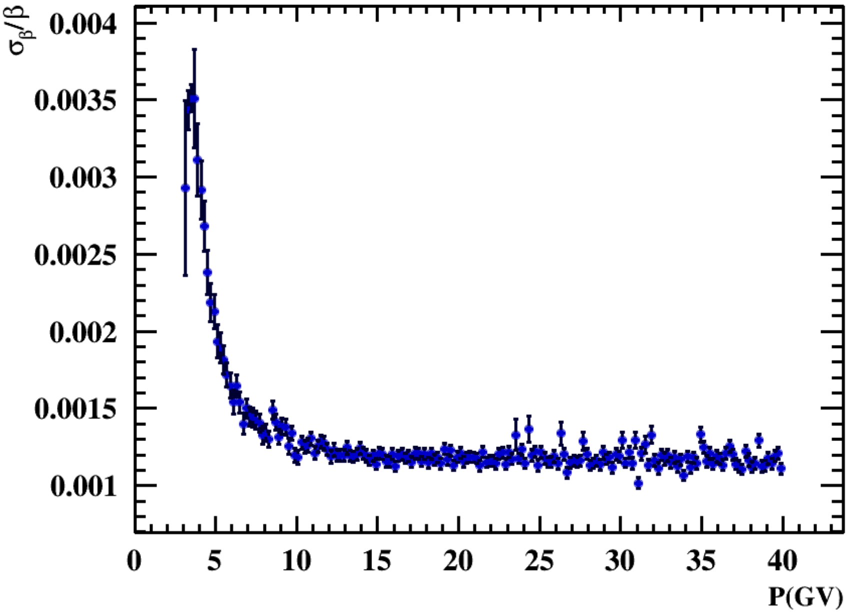

Figure 5.25: Aerogel velocity resolution, estimated for a Monte Carlo proton sample, using the full model as a fit function.

Relative rigidity resolution, σ_P/P (figure 5.24), shows the expected behaviour but with a higher slope.

RICH's relative velocity resolution, σ_β/β (figure 5.25), displays a similar behaviour to that of figure

5.8 but, as expected, with lower values (from $\sim 3.00 \times 10^{-3}$ to a plateau of $\sim 1.25 \times 10^{-3}$).

5.2.5 Results from Fit to AMS-02 Data

The same model was then applied to AMS-02 cosmic ray data, yielding the following results presented in figure 5.26.

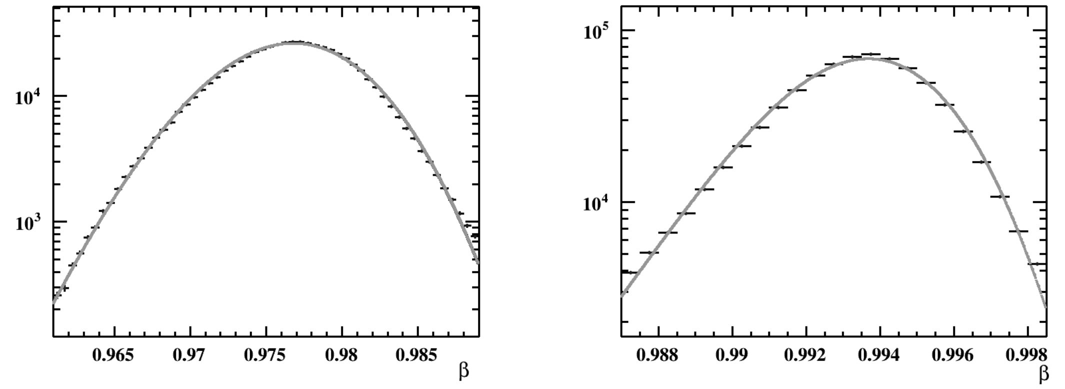

(a) 4 - 4.2 GV

(b) 8 - 8.2 GV

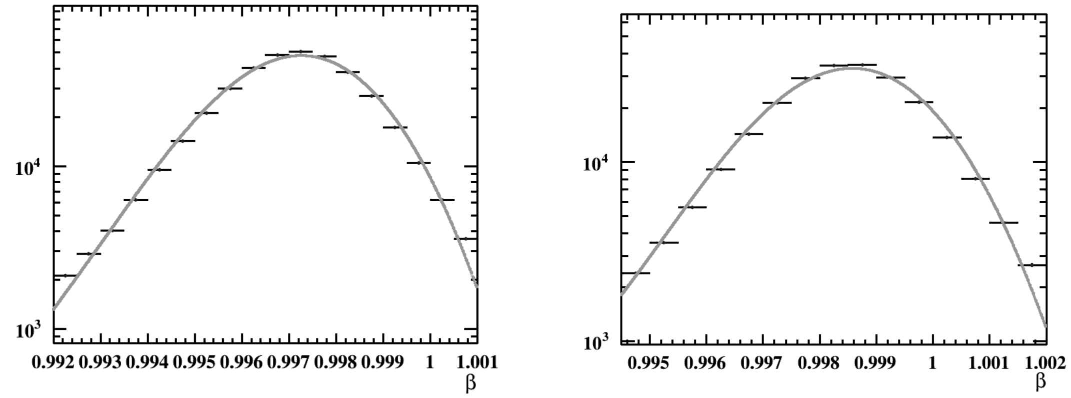

(c) 12 - 12.2 GV

(d) 16 - 16.2 GV

Figure 5.26: Plot of the model fitted to AMS-02 data, for several rigidity intervals.

Organizing the results into graphs once more and comparing them to the results obtained using Monte Carlo gave the results shown in figures 5.27 and 5.28.

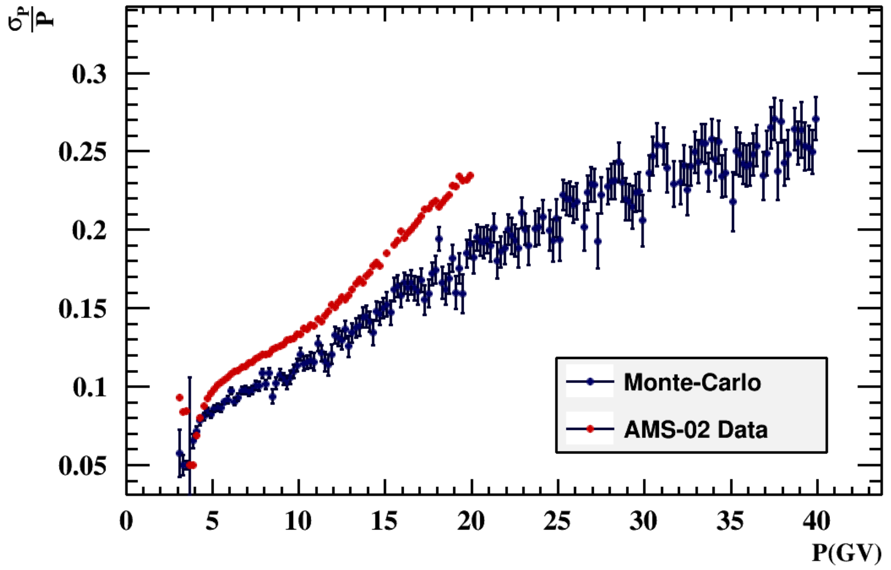

Figure 5.27: Rigidity resolutions, from full model, for Monte Carlo and AMS-02 cosmic ray data.

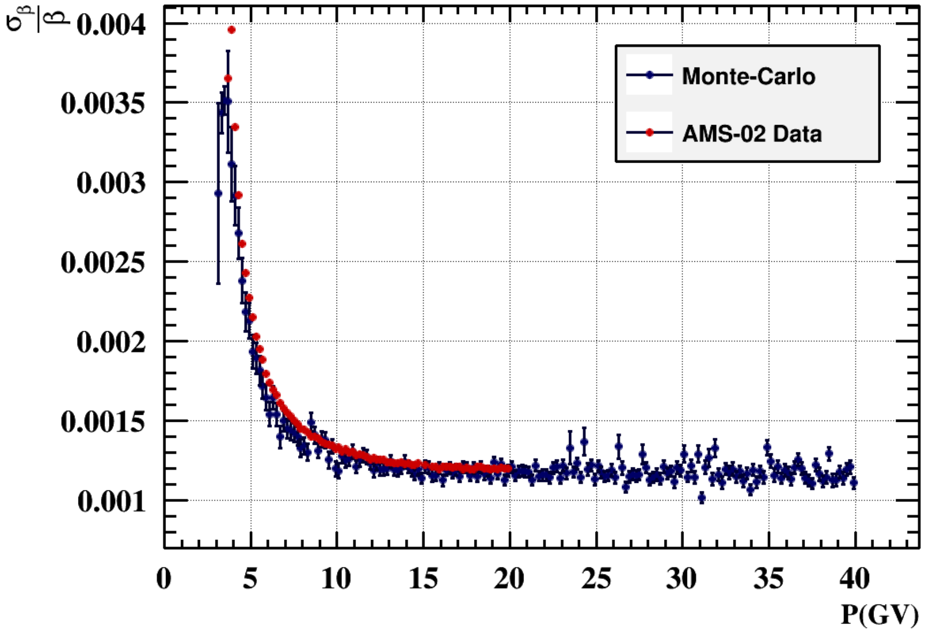

Figure 5.28: Velocity resolutions, from full model, for Monte Carlo and AMS-02 cosmic ray data.

Even though it appears that the model is quite sensitive to the velocity resolution, the estimation of rigidity resolution is not perfect. This is due to the interaction between the shape of the flux and the tracker resolution. Although the primary cosmic ray flux was included in the model, small fluctuations between it and the real one can be masked as a larger contribution in rigidity resolution (instead of having more cosmic rays at a smaller/larger rigidity than the considered, the model increases the counting in that bin by making the resolution larger). Another contribution to this error lies in the selection of data which might slant the flux due to its efficiency not being perfectly flat over all rigidities.

Another thing to keep in mind is that both the width in rigidity and the width in velocity contribute to the width of the distribution. This entails that, to some degree, the two widths are correlated. Even if this is the case, since the two distributions have such a different topology (one is symmetrical and the other is not), one can assume that with a big enough statistics, this correlation will eventually disappear.

The model degenerates on both resolution estimations for the first values of the plot (~ 3 GV), due to not having much statistic near the Cherenkov radiation threshold for protons. Despite this, a fairly good agreement was gotten between both resolutions for both datasets.

The model also showed another aspect that can be a theme of study in later works, the tails of the distributions were not very well parametrized by our model when the effort was made to better fit the peak and main body of the distribution. There are two big contributions to these tails, the simplified model used to describe the Tracker resolution (AMS-02 studies indicate that the proper resolution should have two Gaussian distributions overlapped on inverse rigidity to better cover the tails of the distribution) and due to particle contamination which might slant the distribution. Particle contamination happens both due to a compromise between cut efficiency and event number and to particle interactions inside the detector that might interfere with the proper construction of a ring in RICH.

The model revealed to be a success, giving, at the same time, an estimation of both the TRK's and RICH's resolutions, as well as showing that even though bin migration is present in all measurements it can be duly parametrized.

Now that velocity and rigidity resolutions are known, a study on how they affect particle discrimination can be done.

5.3 Particle Estimator

As a final step for this work, a particle estimator based around RICH's great relative resolution ($\sim 1.25 \times 10^{-3}$) will be built. It will try to identify and discriminate particles up to ~ 15 GV rigidity.

The problem of accurate particle identification is relevant in AMS-02 when trying to select electrons (or positrons). In the positron case, the charge sign and absolute value is the same, forcing an identification based on other physical properties as well. Due to the abundance of protons in the primary flux, estimating the electron flux is as much about selecting electrons as it is trying to eliminate the proton contamination.

5.3.1 Probability and Measurement

This estimator is based on the independent measurement of particle properties by different detectors (RICH and TRK). From the previous study, both velocity and rigidity distributions are well understood. Both velocity and inverse rigidity are normally distributed.

This estimator is constructed around the concept of measurement. As a particle's rigidity is measured, one knows that the particle's true rigidity has to lie somewhere around the measured value. Knowing rigidity's measurement distribution, one can say that the probability that a given X is the true inverse rigidity is given by $\mathrm{Prob} = g(X, X_m, \sigma_X)\,\mathrm{d}X$.

After rigidity is measured, as the particle proceeds down the detector a RICH independent measurement is made, a measurement in velocity. Since velocity and rigidity are connected, the independent velocity measurement should be centred around the true velocity, β_0, with a certain spread. This means that every rigidity measurement represents an interval around which a true rigidity might lie and that true rigidity will create a velocity measurement centred on the true velocity, as is depicted in figures 5.29 and 5.30.

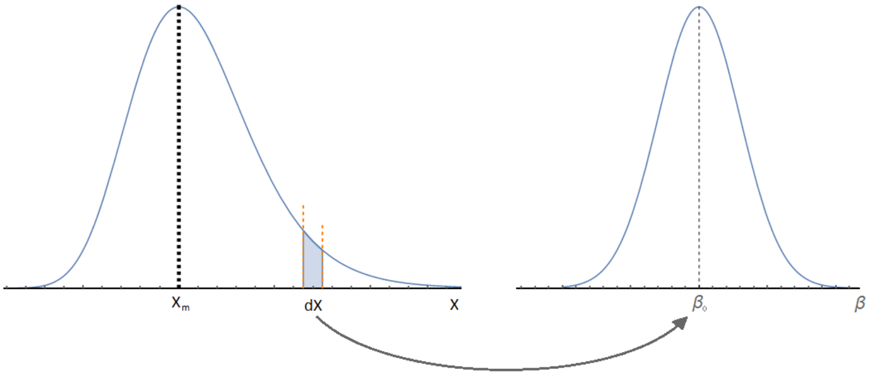

Figure 5.29: Scheme depicting the construction of the particles velocity probability density function.

Following this line of thought, a probability density for velocity might be written as

$$\mathrm{d}P = \underbrace{g(X, X_m, \sigma_X)\,\mathrm{d}X}_{\text{Prob. of X}\in[\text{X;X+dX}]}\, g(\beta, \beta_0(X, m), \sigma_\beta)\,\mathrm{d}\beta, \tag{5.15}$$

or, in a probability density function (PDF) form,

$$\frac{\mathrm{d}P}{\mathrm{d}\beta} = \int_0^{+\infty} \mathrm{d}X g(X, X_m, \sigma_X)\, g(\beta, \beta_0(X, m), \sigma_\beta). \tag{5.16}$$

This expression would be valid in the case that every rigidity measurement gave rise to velocity measurement. This is not the case. Due to RICH detector detection principle, there is a probability that a ring is formed for any given particle rigidity (as was shown in section 5.2.2.D). This implies that the complete probability density function for velocity is given by

$$\frac{\mathrm{d}P}{\mathrm{d}\beta} = \int_0^{+\infty} \mathrm{d}X P_{\text{ring}}(X, \mu(X)) g(X, X_m, \sigma_X)\, g(\beta, \beta_0(X, m), \sigma_\beta). \tag{5.17}$$

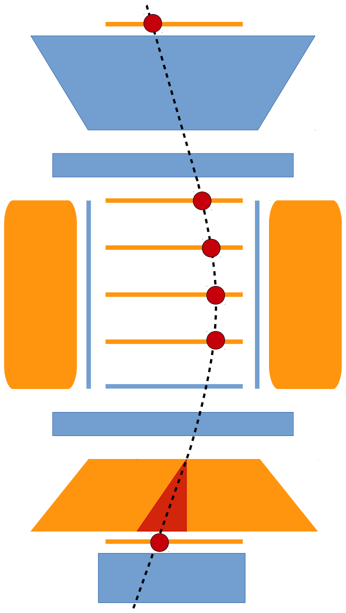

Figure 5.30: Diagram depicting the interaction between the RICH and Tracker.

By thinking in terms of measurements, one can create a probability density function for β and attribute each measured value a different probability of it being compatible with the rigidity measurement. A way to calculate this compatibility is done by integrating expression 5.17 in velocity from the measured value to the closest *infinity*, away from the peak of the distribution, as is shown in figure 5.31. This area represents a probability of the measured velocity β_m belonging to the distribution and is peaked at 0.5, requiring a factor of two so that the function value ranges from 0 to 1.

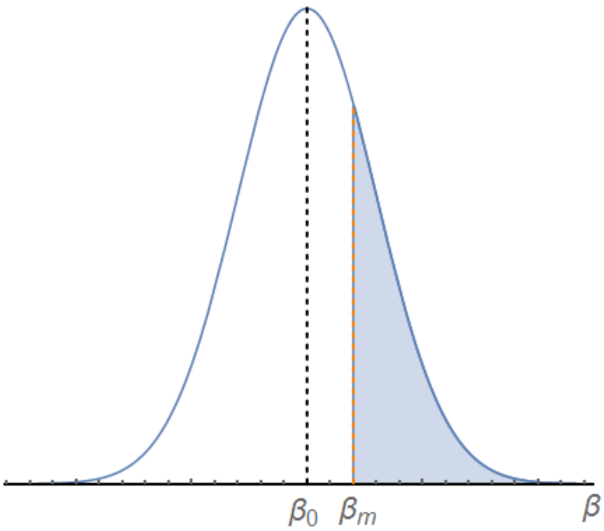

Figure 5.31: Graph depicting the calculation of velocity probability.

The likelihood function that accurately represents the compatibility of rigidity and velocity measurements (X_m, β_m) is then given by

$$\begin{aligned} P(\beta_m \,|\, X_m, m) &= 2\int_0^{+\infty} \mathrm{d}X_0 P_{\text{ring}}(X_0)\, g(X_0, X_m, \sigma_{X_0}) \cdot \begin{cases} \int_0^{\beta_m} \mathrm{d}\beta g[\beta_0(X_0,\, m), \beta, \sigma_\beta] & \text{if } \beta_m < \beta_0 \\ \int_{\beta_m}^{+\infty} \mathrm{d}\beta g[\beta_0(X_0,\, m), \beta, \sigma_\beta] & \text{if } \beta_m < \beta_0 \end{cases} \\ &= 2\int_0^{+\infty} \mathrm{d}X_0 P_{\text{ring}}(X_0)\, g(X_0, X_m, \sigma_{X_0}) \cdot \begin{cases} 0.5 \left[\mathrm{Erf}\left(\frac{\beta_m - \beta_0}{\sqrt{2}\sigma_\beta}\right) - \mathrm{Erf}\left(\frac{-\beta_0}{\sqrt{2}\sigma_\beta}\right)\right] & \text{if } \beta < \beta_0 \\ 0.5 \left[1 - \mathrm{Erf}\left(\frac{\beta_m - \beta_0}{\sqrt{2}\sigma_\beta}\right)\right] & \text{if } \beta < \beta_0 \end{cases} \end{aligned} \tag{5.18}$$

Now that the framework has been laid down, the resolutions have to be parametrized if one seeks to properly identify particles. The AMS-02 software chain provides an error estimation for every rigidity measurement. This error comes from in-depth studies of the entire TRK system and not only from statistical dispersion alone (mainly from a geometrical stand-point - impact point, irregularities in the magnetic field, ...), that error will be taken as a good estimation of where the cosmic ray should lie, rigidity-wise.

In the case of velocity resolution, the estimation from the previous section will become useful.

A detail has been overlooked so far, the constraint between the two measurements, the **mass hypothesis**. This parameter is crucial to the distribution since it relates the true value of both measurements, causing different particles to have different estimators. The estimator gives the probability that, given a certain rigidity measurement and a mass hypothesis, the velocity measurement *belongs* to the distribution, in other words, it measures the probability that a measured (rigidity,velocity) pair belongs to a particle of a given mass. Under Bayes' formalism, one can even try to find out how likely it is that a particle mass generated the dataset by doing

$$\mathrm{prob}(hypothesis|data) \propto \mathrm{prob}(data|hypothesis) \times \mathrm{prob}(hypothesis), \tag{5.19}$$

but that calculation is outside the scope of this work since the following studies will be done in a Monte Carlo pure proton sample, implying that $\mathrm{prob}(hypothesis) = 1$.

5.3.2 Monte Carlo Studies

To study estimator's performance, it was applied to a pure Monte Carlo sample of protons (same used in the previous section), giving the results depicted in figures 5.32 and 5.33.

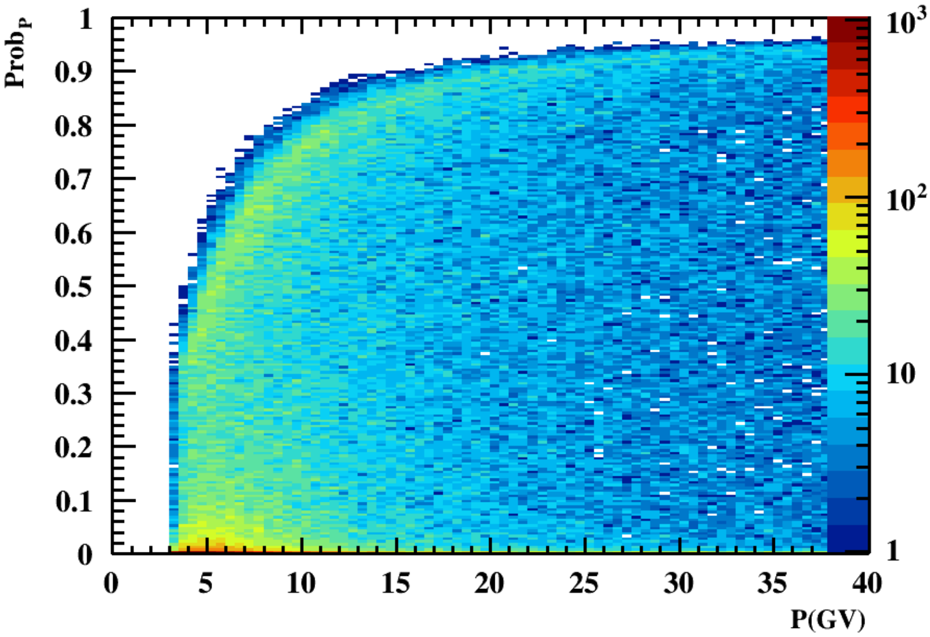

Figure 5.32: Probability that a particle is a proton as given by the estimator, as a function of rigidity, ran over a Monte Carlo proton sample.

This result is highly influenced, rigidity-wise, by the relative abundance of events at different rigidities so a normalization was done in order to clarify the histogram,

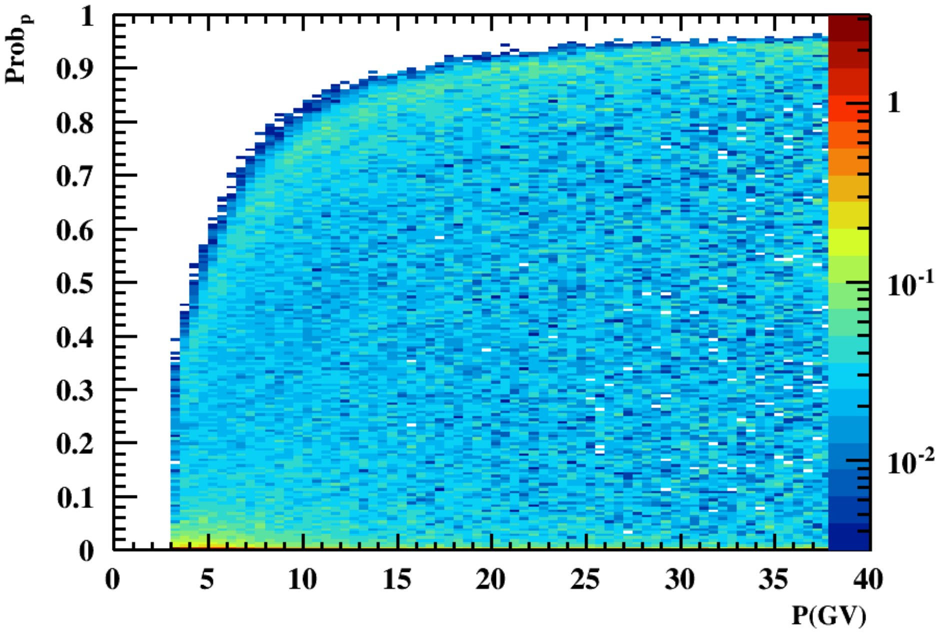

Figure 5.33: Probability that a particle is a proton as given by the estimator, normalized, as a function of rigidity, ran over a Monte Carlo proton sample.

Looking at figure 5.33, an almost flat distribution arises, surrounded by a border. This would be a somewhat unexpected result if put out of context. The border is created by the ring probability. It creates a threshold probability, due to number of hits in the PMT matrix.

The near flatness of the distribution in probability is due to the way this probability is calculated. It is estimated by integrating the distribution in velocity from from 0 to β_m (or from β_m to ∞). This is the calculation of the cumulative probability function.

Statistics show that when a variable x is distributed according to a PDF,

$$\frac{\mathrm{d}N}{\mathrm{d}x} = f(x), \tag{5.20}$$

if a new variable $u(x) = \int_{-\infty}^{x} dx' \, f(x')$ is defined, it can be seen that

$$\frac{\mathrm{d}N}{\mathrm{d}u} = \frac{\mathrm{d}x}{\mathrm{d}u}\frac{\mathrm{d}N}{\mathrm{d}x} = \frac{1}{f(x)}\frac{\mathrm{d}N}{\mathrm{d}x} = \text{constant}. \tag{5.21}$$

Since the probability is constructed in the same way u was, if when calculating the integrated probability of β_m the distribution is flat, the PDF in study is in fact an accurate approximation of the true distribution that generated the dataset.

The next step is to evaluate the result of the estimator for the electron mass hypothesis, against the same Monte Carlo sample of protons. This result is shown in figure 5.34.

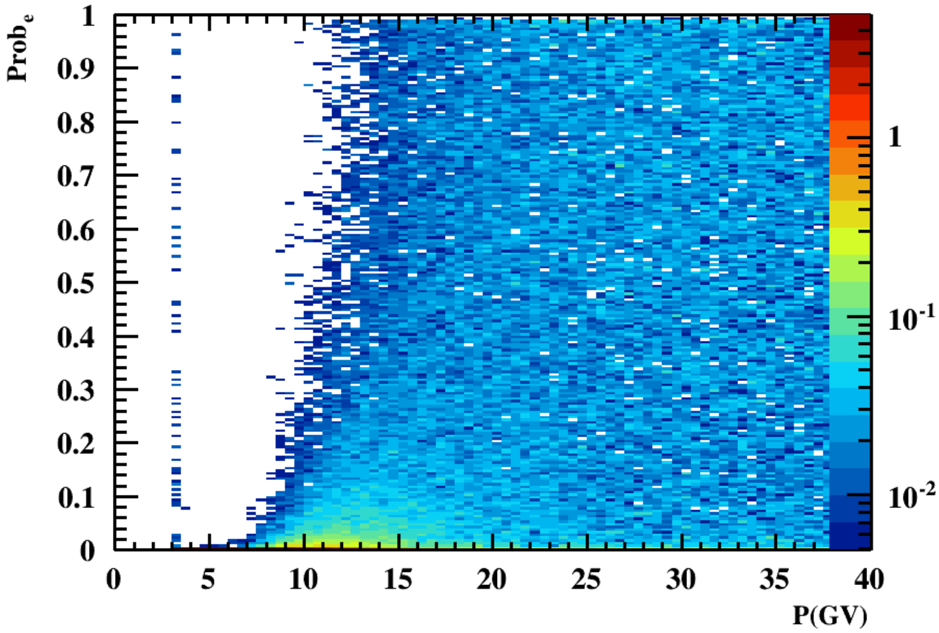

Figure 5.34: Probability that a particle is a electron as given by the estimator, normalized, as a function of rigidity, ran over a Monte Carlo proton sample.

Figure 5.34 shows the expected behaviour for the electron probability, for small values of rigidity, the electron PDF is so far away from the proton measurement that the probability is constantly zero. The clear non-flat behaviour is another hint, it shows that the PDF associated with the electron does not accurately describe the behaviour of the proton sample for such low values of measured velocity.

After $P \sim 7.5$ GV , small values of probability start to appear as the two PDF's intersect, up to the point where they become nearly indistinguishable (for $P > 15$ GV). When the two PDF's merge, the probability of being a proton is almost identical to that of the electron and so, even for this Monte Carlo proton sample, the electron probability starts displaying a near-flat behaviour as well (after $P \sim 15$ GV). These changes in behaviour can easily be seen in figures 5.35 and 5.36 where profiles of both the proton and electron distributions are shown. Proton displays a regular behaviour where the electron starts off with a very slant distribution up to a flat one at high rigidities.

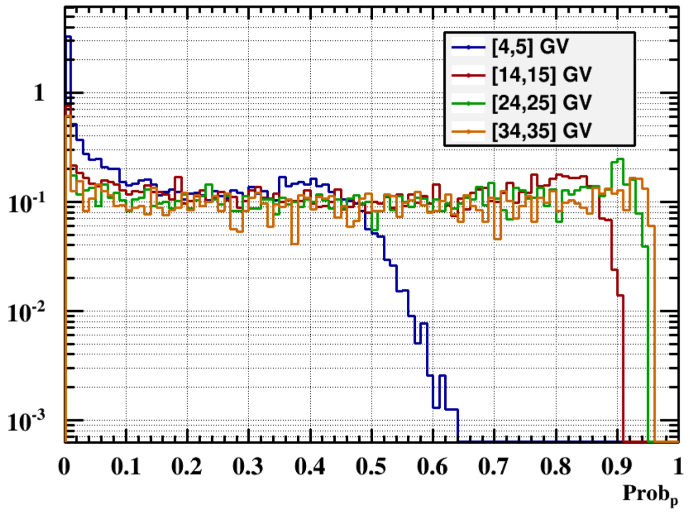

Figure 5.35: Profile of the probability distribution that a particle is a proton as given by the estimator, ran over a Monte Carlo proton sample.

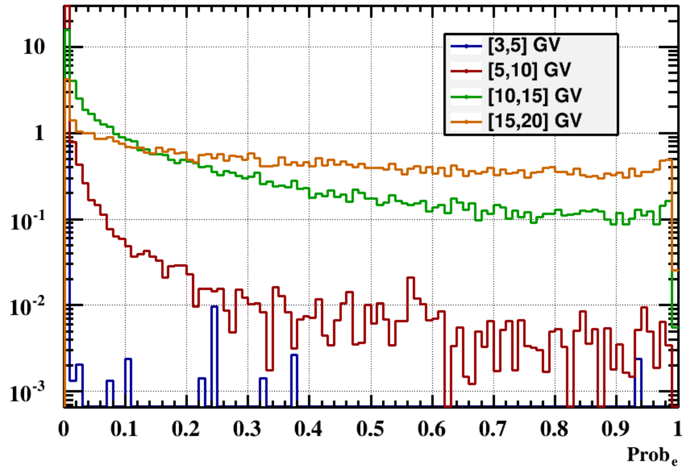

Figure 5.36: Profile of the probability distribution that a particle is a electron as given by the estimator, ran over a Monte Carlo proton sample.

These results show good prospects for the estimator. Figure 5.37 displays two important behaviours, the predominance of the distribution near the $\mathrm{Prob}_e \sim 0$ and the lack of correlation between the two variables ($\mathrm{Prob}_p \neq \mathrm{Prob}_e$). It also highlights the fact that the one instance where both probabilities are somewhat correlated is when the measurement is *bad* and both probabilities return very low values. Even though it does not happen very often, these kind of events have to be rejected due to not being described by either of the two probabilities (populations) in this model. In real data, these events could belong to either bad reconstructions or to a third population of particles.

Knowing how the estimator behaves for a pure sample is important but one wants to understand the implications of using it in the process of selecting data.

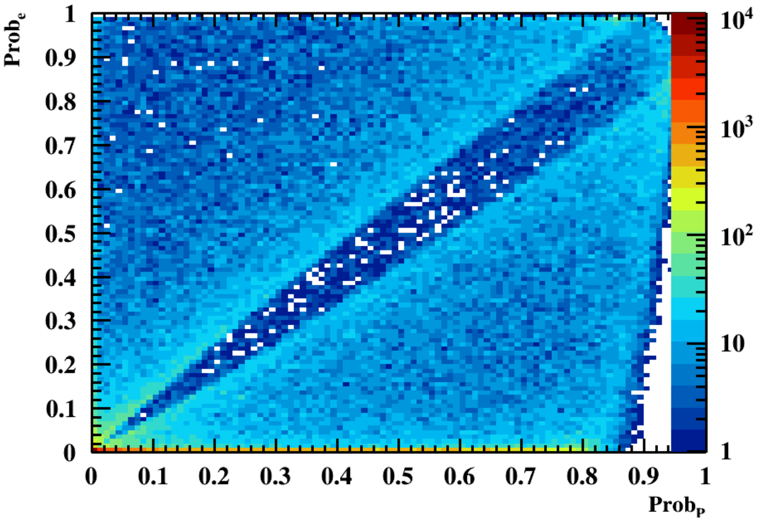

Figure 5.37: Probability that a particle is an electron as given by the estimator as a function probability of being an proton, ran over a Monte Carlo proton sample.

5.3.3 Particle Separation and Contamination

The probabilities determined in the previous section can be used standalone or an **hypothesis test** can be built to decide between two particle species.

This test [17] consists of choosing the different hypotheses (the **null hypothesis** and the alternative hypothesis) and our **test statistic**. The test statistic is a choice of analysis variable that parametrizes the problem, the variable used to study the problem. This choice is usually associated with a simplification or dimensional reduction of the problem.

After the hypothesis are made, an appropriate cut must be selected. This cut (or decision boundary) is associated with a decision to choose the first or the second hypothesis based on the fact that the event being analysed lies on the region of value greater or lower than t_{cut}

More often than not there is an overlap of the PDF's and the choice of t_{cut} implies a choice of how much of the main signal is chosen and, consequently, how much of the background.

As stated previously, AMS-02 flux is primarily protons. When selecting electrons/positrons, there is a high chance of having protons in the selection, a contamination. Using the Monte Carlo sample of protons, and the decision framework presented, it is possible to calculate the theoretical contamination of protons to a given particle sample.

The contamination, C can be calculated by doing

$$C = \frac{\int_x^1 \mathrm{dProb}_{\bar{S}} \frac{\mathrm{d}N}{\mathrm{dProb}_{\bar{S}}}}{\int_0^1 \mathrm{dProb}_{\bar{S}} \frac{\mathrm{d}N}{\mathrm{dProb}_{\bar{S}}}}, \tag{5.22}$$

where S represents the particle species in study.

This contamination may not be easy to calculate but can be determined through the Monte Carlo proton sample.

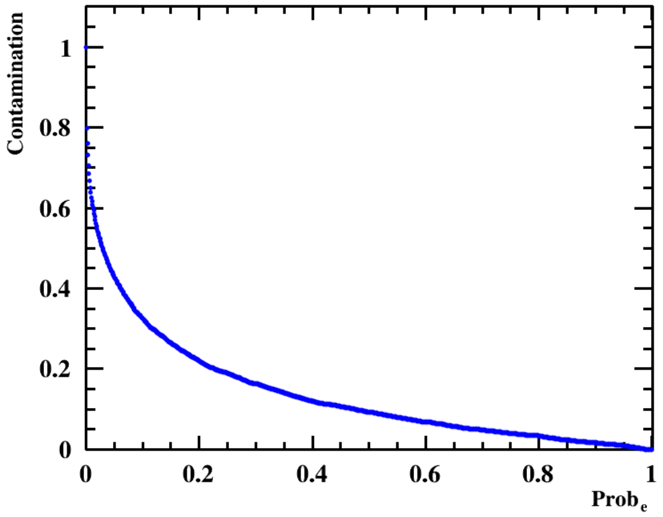

Figure 5.38: Contamination of protons as a function of Prob_e, for the rigidity bin 11-12 GV, estimated using a proton Monte Carlo sample.

Figure 5.38 shows the contamination as a function of the cut for the bin 11-12 GV. It displays the expected behaviour, for very light cuts, the contamination saturates, most protons are able to pass that cut and contaminate the electron sample. On the other hand, if the cut is very high ($t_{cut} > 0.9$), the proton contamination stays low.

One can then calculate an optimized cut such that contamination is smaller than a given value. Due to the abundance of protons in the AMS-02 measured spectrum, when selecting protons, one would not want a contamination to be higher than the signal itself. With that in mind, a cut in Prob_e was developed in order to keep the contamination lower than the electron relative abundance, 1/100. This plot is shown in figure 5.39.

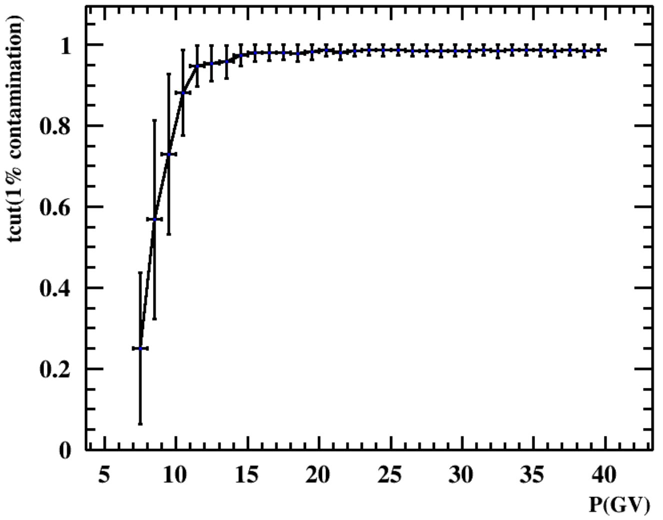

Figure 5.39: Cut in $\mathrm{Prob}_e/(\mathrm{Prob}_p + \mathrm{Prob}_e)$ that insures a proton contamination lower than 1%, as a function of rigidity, estimated using a proton Monte Carlo sample.

Now that the contamination of a theoretical electron sample with protons is understood it is possible to calculate the efficiency of selecting electrons using the estimator presented. As shown by the previous section, the distribution of the variable Prob_S to a pure sample of the particle S (assuming the detector behaviour is well understood) is flat. This entails that $\frac{\mathrm{d}N}{\mathrm{dProb}_S} = constant$ and, since the efficiency is calculated from

$$\epsilon = \frac{\int_{t_{cut}}^{1} \mathrm{dProb}_S \frac{\mathrm{d}N}{\mathrm{dProb}_S}}{\int_0^1 \mathrm{dProb}_S \frac{\mathrm{d}N}{\mathrm{dProb}_S}} = 1 - t_{cut}, \tag{5.23}$$

where t_{cut} is simply the chosen cut on the variable Prob_S.

5.3.4 Relative Probability

As a final step in the study, one would want to create a new variable that would express the behaviour of both the proton probability and the electron probability. The chosen variable was $\frac{\mathrm{Prob}_p}{\mathrm{Prob}_p + \mathrm{Prob}_e}$. This variable reflects the development of proton probability relative to the electron probability. The result of this variable on the MC proton sample is displayed in figure 5.40.

The study of figure 5.37 showed a correlation that is relevant to this study, the low probability regime for both probabilities. If both proton and electron probabilities are low, one has to say the particle belongs to a third population (even if that population is the bad reconstruction population) and can not use the new variable to select it. In this scenario, this variable would fluctuate around the 0.5 value without having any particular meaning, it would be a background centred around 0.5 in figure 5.40 for almost any rigidity. To counter this, an arbitrary cut was chosen, one of the probabilities had to be larger than 0.01 if the ratio was to be calculated.

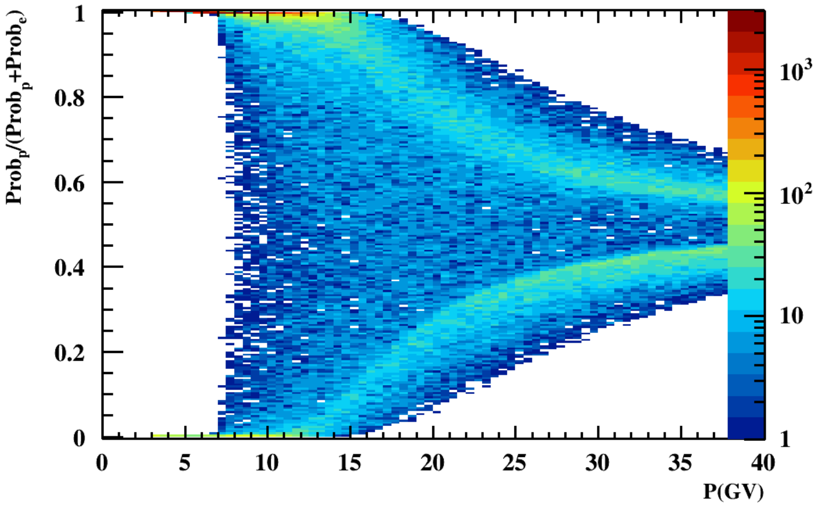

Figure 5.40: Probability that a particle is a proton as given by the estimator divided by the probability of being a proton plus the probability of being an electron ($\frac{\mathrm{Prob}_p}{\mathrm{Prob}_p + \mathrm{Prob}_e}$), ran over a Monte Carlo proton sample.

For clarification, slices of 2 GV width were taken of figure 5.40. These slices are presented in figure 5.41 and allow for a clear visualization of how the two probabilities interact.

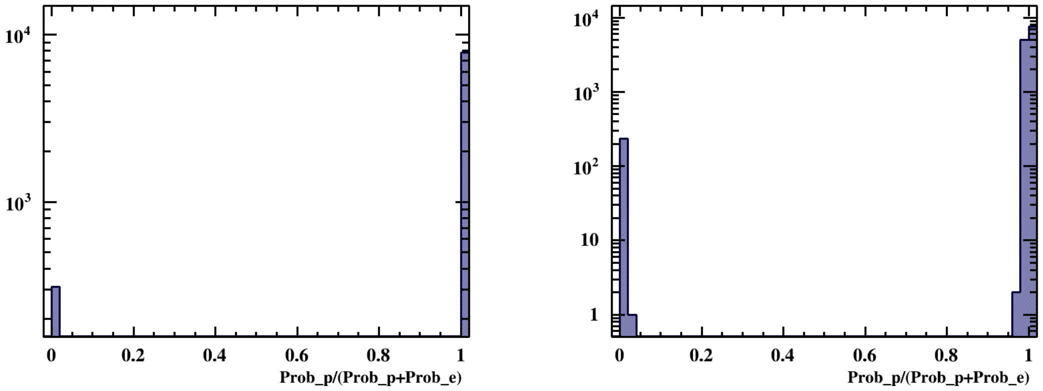

(a) 3 - 5 GV **(b)** 5 - 7 GV

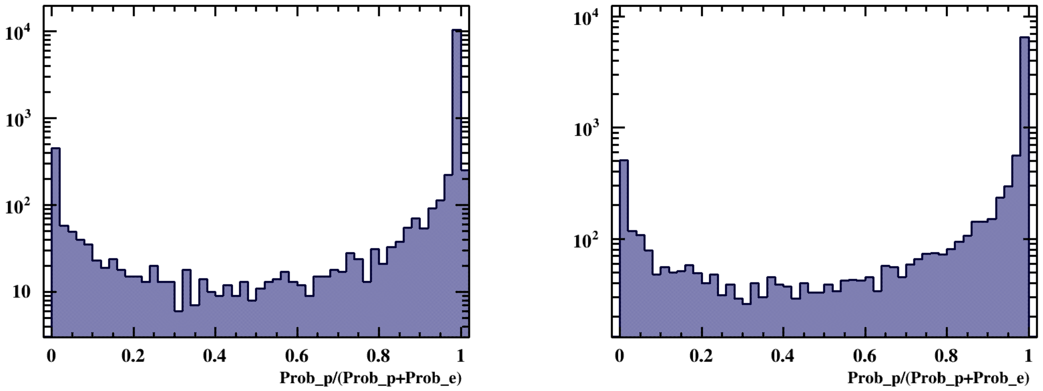

(c) 7 - 9 GV **(d)** 9 - 11 GV

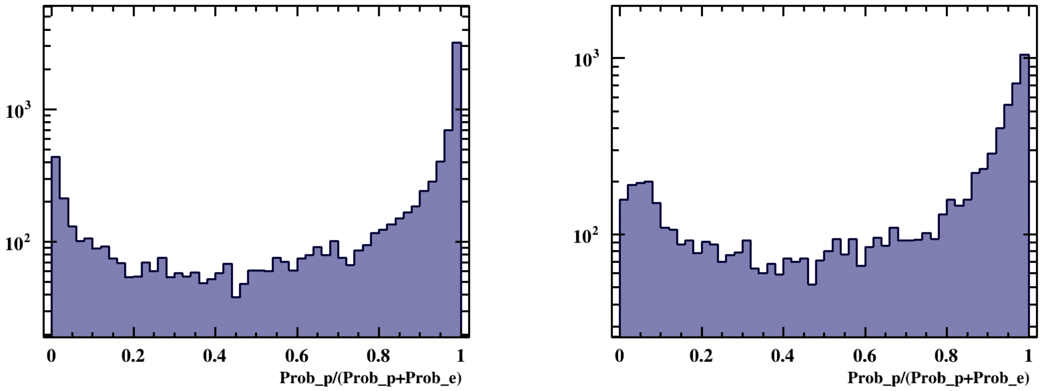

(e) 11 - 13 GV **(f)** 13 - 15 GV

Figure 5.41: Slices in rigidity of $\frac{\mathrm{Prob}_p}{\mathrm{Prob}_p+\mathrm{Prob}_e}$, 2 GV wide, ran over a Monte Carlo proton sample.

In the first bins, the separation is complete, there are two very well separated peaks where particles are either identified as protons or as electrons. As rigidity grows, the two probabilities stay far away from each other but some events start filling the space between them. After a certain rigidity, $P > 15$ GV, the distribution starts displaying two populations that tend towards 0.5. The symmetrical nature of the estimator, for high momenta, gives rise to this dual behaviour tending towards 0.5 which reflects the merging of the PDF's for both estimators.

To study the low probability for low rigidity population, a plot on velocity versus rigidity was done for all events with lower probability than 0.1. This plot is shown on figure 5.42. This plot clearly showcases the bad probabilities at low rigidities. There are two obvious curves, a sample contamination and the proton curve itself progressing towards the higher velocities (where it becomes hard to distinguish the two probabilities). This contamination is due to low mass secondary particles generated by the proton as it traverses the detector, generating the peak at low probabilities seen throughout the early rigidities in figure 5.41.

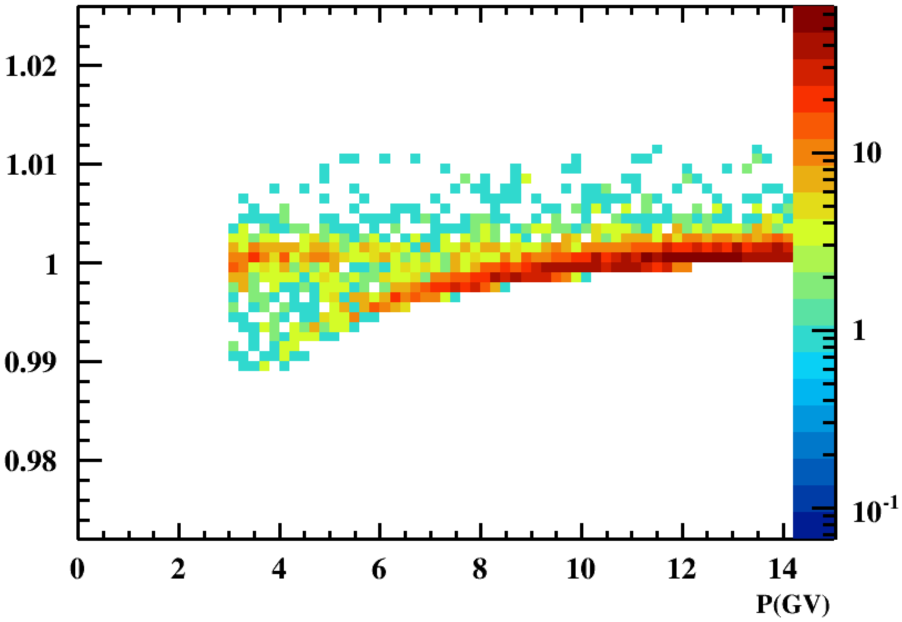

Figure 5.42: Particle velocity as a function of rigidity for particles with $\frac{\mathrm{Prob}_p}{\mathrm{Prob}_p+\mathrm{Prob}_e} < 0.1$.

For rigidities lower than $15\mathrm{GV}$ the estimator offers a great discrimination power since the distribution remains very asymmetrical and with a clear distinction between the peaks (the peak on the low probabilities being a contamination in Monte Carlo for rigidities up to 5 GV). From the results given by both estimators, one could assume that a pure electron sample would give a somewhat mirrored distribution from this one. This shows high hopes for the estimator and its separation power.

Another application of the estimator comes from the asymmetrical nature of the result (in the working regime), a technique called template fitting. From pure samples of particles, one extracts the distribution for each species, for each bin in rigidity. In order to do this, one makes use of either Monte Carlo or very pure samples of real data so that the template distributions are estimated as precisely as possible. In real data, the total flux should have different contributions from different populations, each with its own template. Knowing that real data is an overlap of these distributions with different normalizations each, one can try to find out these normalizations (relative species abundance) by fitting these templates to data additively. Even though this was not done due to time constraints, the estimator shows great prospects in this area.

This estimator showed that it can be used as an additional tool when selecting cosmic rays from a given dataset. It showed a good capability of particle discrimination for low rigidities (up to 15 GV).

In order to improve it, still using RICH, other properties dependent on particle species could be added, such as charge. Remembering from equation 5.3 that there's a Z^2 dependency on number of radiated photons, it would be possible to add charge to the estimator in order to make it more complete but that leaves the scope of this work.

6

Conclusions and Prospects

Contents

6.1 Conclusions and Prospects 78

6.1 Conclusions and Prospects

The main goal of this thesis was to study the Solar Modulation of Galactic cosmic rays using data from AMS-02 and develop a particle separation tool that would allow to select particles using the AMS RICH detector.

This thesis began by describing the theoretical model behind Solar modulation and the interaction of cosmic rays with the highly conductive Solar plasma.

Under the assumption of isotropy in cosmic rays a density function was defined and a transport equation was deduced. This equation revealed to be a parabolic equation 3-dimensional in space, 1-dimensional in time and 1-dimensional in momentum which entails a numerical resolution due to the non-linearity of most of its coefficients. The choice of parameters used was based on the most current approaches to solving the Parker transport equation and revealed to be in great agreement with AMS-02 data.

In this work, three approaches were taken when attempting to solve the equation. The first approach take was the Force-Field solution, which tries to simplify the problem to one of a cosmic ray traversing a dispersive medium, resulting on a single modulation coefficient that parametrizes the whole phenomenon. It estimates an average effect of energy loss. The 1D and 2D solutions try to solve the problem numerically, having the simplification of reduction of dimensions and assuming steady state solutions $\partial f/\partial t = 0$.

As a whole, all these simulations revolve around the knowledge of the shape of the diffusion coefficients, the Solar wind, the Solar magnetic field and of the Local Interstellar flux. The estimation of the diffusion coefficient is done under the area of QLT and diffusion models, the Solar wind comes from Thermodynamics, Solar corona studies and modelling of data taken from probes such as the SOHO, the complex Solar magnetic comes from MHD and, lastly, the Local Interstellar Spectrum (LIS) flux comes from Monte-Carlo Diffusion models, Galactic propagation models and data taken from probes such as the Voyager.

Solar modulation is a deep and complex area of study which still has many problems to resolve and many phenomena to discover before it can claim the Solar plasma as understood.

After the Solar modulation phenomenon was duly parametrized and interpreted under propagation models in Plasma Physics, the next appropriate step would be the comparison with data and parameter estimation. In this thesis, an intermediate step was taken instead, rather than calculating a flux from pre-existing tools, a new tool was developed to help identify the particles that arrived at AMS-02 and, therefore, provide a more accurate reading of the actual measured flux.

AMS-02 constitutes a great asset to Astroparticle Physics due to its precision, acceptance and long exposure to the cosmic ray flux. As capable as AMS-02 may be, it is still an instrument that studies a complex object, the cosmic ray flux. Even though there are several estimations of the chemical composition of the cosmic rays that arrive at Earth's upper atmosphere, each individual cosmic ray still has to be identified through analysis of the detector's signals. AMS-02 is equipped with a series of collinear detectors which provide a set of independent measurements that intersect so that particle species and its properties may be properly identified.

The imposition of criteria to identify and discriminate these particles, as they come into the detector, is what is a called a selection. As each events goes through the selection algorithm, it has to pass the tests in order to be considered for analysis. Estimators can be developed in order to aid the selection in being more accurate without losing too much efficiency in the process.

This lead to the next step of the thesis, the study of the RICH detector and the development of an estimator of particle species. Using the RICH and the TRK present in AMS-02 as independent instruments, a model was developed to describe the flux measured.

It was rather difficult to fit the model to the Monte Carlo data but it revealed to be a success in the end.

Even though the Tracker resolution study revealed to not be as precise as it was hoped, the results were not so far away from each other that they could be considered unrelated. The ill estimation of the flux reaching the detector caused an increased error in rigidity resolution estimation.

The velocity resolution appeared to not be as affected by such a phenomenon since it gave a very consistent result to expectation, as the velocity goes up, the particles radiate a full ring, with more photoelectrons, reaching a peak in accuracy (the plateau in the figure).

After the set up RICH and TRK was studied and model developed, an estimator was proposed to identify particles based on this two detectors.

The estimator revealed to be quite capable of particle identification in our spectrum of particles (from ~ 3 GV to ~ 15 GV). The estimator had the expected behaviour in a proton sample, it exhibited a flat behaviour in proton probability and it was peaked at zero for low rigidities ($P < 15$ GV) in the electron probability.

That accuracy degraded with the increase in rigidity ($P > 15$ GV). As the PDF's merge at $\beta = 1$, the accuracy of the estimator starts to not be able to properly distinguish between particles, but this does not step away from predictions. A cut was estimated, as a function of measured rigidity, that would minimize the proton contamination in an electron selection to bellow 1/100.

As a final step, a new relative probability variable was defined that displayed the good discrimination power of the estimator as a function of rigidity, showing good prospects to the application of the estimator to AMS-02 data.

Even though this thesis did not estimate a flux of cosmic rays based on AMS-02 data, it set down the tools to do so. All methods are implemented in C++ classes in the LxSoft and LxLipana framework developed at Laboratório de Instrumentação e Física Experimental de Partículas (LIP). It has methods based around the AMS-02 software chain and several analysis and selection tools were developed.

As a next step, and already out of the scope of this thesis, a flux may be calculated, based on the performance of both the model and the estimator, in order to estimate flux variations due to Solar modulation.

Bibliography

[1] A. D. Panov et al. Elemental energy spectra of cosmic rays from the data of the atic-2 experiment. *Bull. Russian Acad. of Science: Physics*, 71(4), 2007.

[2] M. Aguilar, J. Alcaraz, J. Allaby, et al. The alpha magnetic spectrometer (ams) on the international space station: Part i - results from the test flight on the space shuttle. *Physics Reports*, 366(6): 331–405, 2002.

[3] L. Alvarez and A. H. Compton. A positively charged component of cosmic rays. *Physical Review*, 43:835–836, 1933.

[4] AMS-02 Collaboration. Ams-02 the alpha magnetic spectrometer experiment, 2014. URL `http://www.ams02.org/`.

[5] AMS Collaboration. Helium in near earth orbit. *Phys. Lett. B*, 494, 2000.

[6] A. D. Angelis. Spontaneous ionization to subatomic physics: Victor hess to peter higgs. Opening talk on the 4th International Conference on Particle and Fundamental Physics in Space, 2012.

[7] H. Bhabha and W. Heitler. The passage of fast electrons and the theory of cosmic showers. *Proceedings of the Royal Society of London*, 159:432–458, 1937.

[8] L. Biermann and A. Schlüter. Cosmic radiation and cosmic magnetic fields. ii. origin of cosmic magnetic fields. *Physical Review*, 82(6):863–868, 1951.

[9] L. Biermann, B. Brosowski, and H. U. Schmidt. The interaction of the solar wind with a comet. *Solar Physics*, 1(2):254–284, 1967.

[10] R. A. Burger and M. S. Potgieter. The calculation of neutral sheet drift in two-dimensional cosmic-ray modulation models. *The Astrophysical Journal*, 339:501–511, 1989.

[11] R. A. Burger, H. Moraal, and G. M. Webb. Drift theory of charged particles in electric and magnetic fields. *Astrophysics and Space Science*, 116:107–129, 1985.

[12] R. A. Burger, H. Moraal, and M. S. Potgieter. On the inclusion of a wavy neutral sheet in two-dimensional drift models. In *Proceedings of the 20th International Cosmic Ray Conference Moscow*, volume 3, pages 283–286, 1987.

[13] R. A. Burger, T. P. J. Krüger, M. Hitgie, and N. E. Engelbrecht. A fisk-parker hybrid heliospheric magnetic field with a solar-cycle dependence. *The Astrophysical Journal*, 674:511–519, 2008.

[14] R. A. Caballero-Lopez and H. Moraal. Limitations of the force field equation to describe cosmic ray modulation. *Journal of Geophysical Research*, 109, 2004.

[15] P. A. Cherenkov. Visible emission of clean liquids by action of γ radiation. *Proceedings of the USSR Academy of Sciences*, 2:451, 1934.

[16] J. Clay. Penetrating radiation. *Proceedings of the Royal Academy of Amsterdam*, 30:1115–1127, 1927.

[17] G. Cowan. *Statistical Data Analysis*. Clarendon Press, Oxford, 1998.

[18] D. J. McComas et al. The heliosphere's interstellar interaction: No bow shock. *Science*, 336: 1291–1293, 2012.

[19] D. Müller et al. *Ap. J.*, 312(183), 1991.

[20] M. L. F. da Gama Velho Arruda. *Charge and velocity reconstruction with the RICH detector of the AMS experiment - Analysis of the RICH prototype data*. PhD thesis, Universidade Técnica de Lisboa - Instituto Superior Técnico, 2008.

[21] Département de Physique Nucléaire et Corpusculaire. Ams-02 ring imaging cherenkov counter - main structural components, 2010. URL `http://dpnc.unige.ch/ams/ams_beta/Gallery/gallery.shtml`.

[22] F. Aharonian et al. First ground based measurement of atmospheric cherenkov light from cosmic rays. *Phys. Rev. D*, 75, 2007.

[23] E. Fermi. On the origin of the cosmic radiation. *American Physical Society*, 75(8):1169–1174, 1949.

[24] I. Frank and I. Tamm. Coherent visible radiation from fast electrons passing through matter. *Proceedings of the USSR Academy of Sciences*, 14:109–114, 1937.

[25] L. J. Gleeson and W. I. Axford. Solar modulation of galactic cosmic rays. *The Astrophysical Journal*, 154:1011–1026, 1968.

[26] L. J. Gleeson and I. H. Urch. A study of the force-field equation for the propagation of galactic cosmic rays. *Astrophysics and Space Science*, 25:387–404, 1973.

[27] A. Gockel. Observations on the radiation of high penetration power on the eiffel tower. *Physikalische Zeitschrschift*, 12:595, 1911.

[28] H. S. Ahn et al. Charge composition and energy spectra of cosmic-ray nuclei for elements from be to ni - results from heao-3-c2. *Astron. & Astrophys.*, 233(1), 1990.

[29] H. S. Ahn et al. Energy spectra of cosmic-ray nuclei at high energies. *Astrophys. J.*, 707, 2009.

[30] V. F. Hess. On the observation of the penetrating radiation in seven free balloon campaigns. *Physikalische Zeitschrschift*, 13:1084, 1912.

[31] INFN Bologna AMS. Ams-02 bologna group, 2007. URL `http://www.bo.infn.it/ams`.

[32] J. D. Jackson. *Classical Electrodynamics*. John Wiley & Sons, Inc., 1998.

[33] T. H. Johnson. The azimuthal asymmetry of the cosmic radiation. *Physical Review*, 43:834–835, 1933.

[34] J. R. Jokipii. Cosmic-ray propagation. i. charged particles in a random magnetic field. *The Astrophysical Journal*, 146:480–487, 1966.

[35] J. R. Jokipii and J. M. Davila. Effects of particle drift on the transport of cosmic rays. iv. more realistic diffusion coefficients. *The Astrophysical Journal*, 248:1156–1161, 1981.

[36] J. R. Jokipii and D. A. Kopriva. Effects of particle drift on the transport of cosmic rays. iii. numerical models of galactic cosmic-ray modulation. *The Astrophysical Journal*, 234:386–392, 1979.

[37] J. R. Jokipii and E. H. Levy. Effects of particle drifts on the solar modulation of galactic cosmic rays. *The Astrophysical Journal*, 213L:85–88, 1977.

[38] K. A. Olive, et al. (Particle Data Group). The review of particle physics. *Chinese Physics C*, 38 (090001), 2014.

[39] K. Asakimori et al. Cosmic-ray proton and helium spectra: Results from the jacee experiment. *Ap. J.*, 502, 2007.

[40] M. G. Kivelson and C. T. Russel. *Introduction to Space Physics*. Cambridge University Press, 1995.

[41] W. Kolhörster. Messungen der durchdringenden strahlungen bis in höhen von 9300 m. *Verhandlungen der Deutschen Physikalischen Gesellschaft*, 16:719–721, 1914.

[42] J. Kóta and J. R. Jokipii. Effects of drifts on the transport of cosmic rays. vi. a three-dimensional model including diffusion. *The Astrophysical Journal*, 265:573–581, 1983.

[43] M. Ackermann et al. Detection of the characteristic pion-decay signature in supernova remnants. *Science*, 339(6121):807–811, 2013.

[44] M. Ave et al. Composition of primary cosmic-ray nuclei at high energies. *Ap. J.*, 678, 2008.

[45] M. Boezio et al. Energy spectra of atmospheric muons measured with the caprice98 balloon experiment. *Phys. Rev. D*, 67, 2003.

[46] J. Minnie. *An Ab Initio Approach to the Heliospheric Modulation of Galactic Cosmic Rays*. PhD thesis, North-West University, Potchefstroom Campus, 2006.

[47] H. Moraal. Cosmic-ray modulation equations. *Space Science Reviews*, 176(1–4):299–319, 2011.

[48] NASA. The alpha magnetic spectrometer ams-02, 2011. URL `http://ams.nasa.gov/`.

[49] NASA. Nasa homepage, 2014. URL `http://www.nasa.gov/`.

[50] N. F. Ness, C. S. Scearce, and J. B. Seek. Initial results of the imp 1 magnetic field experiment. *American Geophysical Research*, 69(17):3531–3569, 1964.

[51] E. N. Parker. Dynamics of the interplanetary gas and magnetic fields. *The Astrophysical Journal*, 128:664–676, 1958.

[52] E. N. Parker. A history of early work on the heliospheric magnetic field. *Journal of Geophysical Research*, 106(A8):15797–15801, 2001.

[53] D. W. Peaceman and H. H. Rachford. The numerical solution of parabolic and elliptic differential equations. *Journal of the Society for Industrial and Applied Mathematics*, 3(1):28–41, 1955.

[54] C. Pei, J. W. Bieber, B. Breech, R. A. Burger, J. Clem, and W. H. Matthaeus. Cosmic ray diffusion tensor throughout the heliosphere. *Journal of Geophysical Research*, 115, 2010.

[55] C. Pei, J. W. Bieber, R. A. Burger, and J. Clem. A general time-dependent stochastic method for solving parker's transport equation in spherical coordinates. *Journal of Geophysical Research*, 115, 2010.

[56] C. Pei, J. W. Bieber, R. A. Burger, and J. Clem. Three-dimensional wavy heliospheric current sheet drifts. *The Astrophysical Journal*, 744:170–175, 2012.

[57] M. S. Potgieter and H. Moraal. A drift model for the modulation of galactic cosmic rays. *The Astrophysical Journal*, 294:425–440, 1985.

[58] B. Rossi. On the magnetic deflection of cosmic rays. *Physical Review*, 36:606, 1930.

[59] B. Rossi. Directional measurement on the cosmic rays near the geomagnetic equator. *Physical Review*, 45:212–214, 1934.

[60] S. Haino et al. Measurements of primary and atmospheric cosmic-ray spectra with the bess-tev spectrometer. *Phys. Lett. B*, 594, 2004.

[61] S. Haino on behalf of the AMS-02 Collaboration. Precision measurement of the proton flux with ams. In *Proceedings of the 33rd International Cosmic Ray Conference - Rio de Janeiro*, 2013.

[62] J. Séguinot and T. Ypsilantis. Photoionization and cherenkov ring imaging. *Nuclear Instruments and Methods in Physics Research*, 142:377, 1977.

[63] T. Sanuki et al. Precise measurement of cosmic-ray proton and helium spectra with the bess spectrometer. *The Astrophysical Journal*, 545, 2003.

[64] S. Ting. Status of the ams experiment. In 22^{nd} *European Cosmic Ray Symposium*, 2010.

[65] I. Usoskin. Heliospheric physics and cosmic rays. Lecture Notes from Heliospheric Physics and Cosmic Rays course at University of Oulu, 2003.

[66] I. G. Usoskin, G. A. Brazilevskaya, and G. A. Kovaltsov. Solar modulation parameter for cosmic rays since 1936 reconstructed from ground-based neutro monitors and ionization chambers. *Journal of Geophysical Research*, 116, 2011.

[67] V. A. Derbina et al. Cosmic-ray spectra and composition in the energy range of 101000 tev per particle obtained by the runjob experiment. *Ap. J.*, 628, 2005.

[68] W. R. Webber and P. R. Higbie. Galactic propagation of cosmic ray nuclei in a model with an increasing diffusion coefficient at low rigidities: A comparison of the new interstellar spectra with voyage data in the outer heliosphere. *Journal of Geophysical Research*, 114, 2009.

[69] Z. Weng. *Particle Identification Using Transition Radiation Detector and Precision Measurement of Cosmic Ray Positron Fraction with the AMS-02 Experiment*. PhD thesis, Sun Yat-Sen University, 2013.

[70] T. Wulf. Observations on the radiation of high penetration power on the eiffel tower. *Physikalische Zeitschrschift*, 11:811, 1910.

[71] G. P. Zank, W. H. Matthaeus, and J. W. Bieber. The radial and latitudinal dependence of the cosmic ray diffusion tensor in the heliosphere. *Journal of Geophysical Research*, 103(A2):2085–2097, 1998.